Mechanics of filled rubbers from a molecular point of view

Mechanics of filled rubbers from a molecular point of view

ACADEMISCH PROEFSCHRIFT

ter verkrijging van de graad van doctor
aan de Universiteit van Amsterdam
op gezag van de Rector Magnificus
prof. dr. ir. K.I.J. Maex
ten overstaan van een door het College voor Promoties
ingestelde commissie,
in het openbaar te verdedigen in de Agnietenkapel
op woensdag 19 april 2017, te 10:00 uur

door

Hasan Samet Varol

geboren te Şişli, Turkije

PROMOTIECOMMISSIE

Promotor: prof. dr. M.Bonn   Universiteit van Amsterdam
Co-promotor   dr. S. H. Parekh   Max-Planck-Institut für Polymerforschung

Overige Leden: prof. dr. S. Woutersen   Universiteit van Amsterdam
                    prof. dr. G. H. Wegdam   Universiteit van Amsterdam
                    dr. N.F. Shahidzadeh   Universiteit van Amsterdam
                    dr. R. Sprik   Universiteit van Amsterdam
                    prof. dr. T. Vilgis   Max-Planck-Institut für Polymerforschung
                    prof. dr. A. Zaccone   University of Cambridge

Faculteit der Natuurwetenschappen, Wiskunde en Informatica

This thesis is dedicated to all of the child refugees who lost their lives crossing mountains and seas to escape war.

PUBLICATIONS COVERED IN THIS THESIS

Chapter 3:

M. R. B. Mermet-Guyennet, J. de Castro, H. S. Varol, M. Habibi, B. Hosseinkhani, N. Martzel, R. Sprik, M. M. Denn, A. Zaccone, S. H. Parekh and D. Bonn, "Size-dependent reinforcement of composite rubbers," *Polymer, 73*, 170-173 (2015).

Chapter 4:

H. S. Varol, M. A. Sánchez, H. Lu, J. E. Baio, C. Malm, N. Encinas, M. R. B. Mermet–Guyennet, N. Martzel, D. Bonn, M. Bonn, T. Weidner, E. H. G. Backus and S. H. Parekh, "Multiscale Effects of Interfacial Polymer Confinement in Silica Nanocomposites," *Macromolecules, 48,* (21), 7929–7937 (2015).

Chapter 5:

H. S. Varol, F. Meng, B. Hosseinkhani, C. Malm, D. Bonn, M. Bonn, A. Zaccone and S. H. Parekh, "Nanoparticle amount, and not size, determines chain alignment and nonlinear hardening in polymer nanocomposites," *PNAS,* accepted (2017).

OTHER PUBLICATIONS

S. A. Jensen, Z. Mics, I. Ivanov, H. S. Varol, D. Turchinovich, F. H. L. Koppens, M. Bonn, and K. J. Tielrooij, "Competing Ultrafast Energy Relaxation Pathways in Photoexcited Graphene," *Nano letters, 14* (10), 5839–5845 (2014).

J. G. de Castro, R. Zargar, M. Habibi, H. S. Varol, S. H. Parekh, B. Hosseinkhani, M. Adda-Bedia and D. Bonn, "Nonmonotonic fracture behavior of polymer nanocomposites," *Appl. Phys. Lett., 106*. 221904 (2015).

H. S. Varol, O. Álvarez-Bermúdez, P. Dolcet, B. Kuerbanjiang, S. Gross, K. Landfester, and R. Muñoz-Espí, "Crystallization at Nanodroplet Interfaces in Emulsion Systems: A Soft-Template Strategy for Preparing Porous and Hollow Nanoparticles," *Langmuir,* DOI: 10.1021/acs.langmuir.6b02954 (2016).

CONTENTS

Contents

CHAPTER 1: INTRODUCTION

1.1 Overview

This dissertation presents my results, and associated background information, from my PhD research on polymer nanocomposites. My PhD project focused on explaining – from a molecular scale view – linear and nonlinear viscoelastic properties of polymer – and more specifically elastomer – based nanocomposites. A detailed outline of my thesis is provided below.

- **Chapter 1** provides a theoretical background of the work. First, basic principles of elastomers and elastomer-based nanocomposites are introduced. Then, the importance of studying the molecular-scale properties of nanocomposites to understand their macroscopic mechanical properties and practical uses is discussed. This chapter is closed by explaining viscoelasticity and polymer state-of-order in nanocomposites.

- **Chapter 2** starts with providing information about the polymer materials used in this thesis. This is followed by an explanation of the microscopic and spectroscopic instruments used in this work. Finally, a discussion of the different statistical tests used for deriving useful conclusions from noisy experimental results is included.

- **Chapter 3** focuses on how we generated a universal scaling parameter for explaining the linear viscoelastic properties (reinforcement) of polymer composite systems. Our work shows how the reinforcement of elastomers by various sized (micro and nano) inorganic fillers can be predicted based on filler size and volume fraction.

- **Chapter 4** focuses on the effect of rubber end group functionality on filler dispersion measured on multiple length scales in nanocomposite systems. The nature of interfacial interactions and molecular structure of rubber molecules on silica surfaces are determined by different surface-sensitive spectroscopic methods.

- **Chapter 5** focuses on the coupled behavior of nonlinear strain hardening and molecular orientation in typical nanocomposites. A potential reason

explaining increased nonlinear strain-hardening and increased polymer chain alignment with increasing filler content is presented with polarized Raman spectroscopy and simple scaling arguments describing chain alignment.

- **Chapter 6** is the future directions part of the thesis where I will present my preliminary results about the hardening behavior of nanocomposites under cyclic forces. I will end this chapter by including the next experimental ideas that I believe will contribute substantially to understand the strain-hardening properties of the nanocomposites under cyclic forces.

In this thesis, I have included the major subjects of my PhD research: spectroscopy and mechanics of rubber nanocomposite materials. In addition to the work shown here, I also took part in various side projects: (1) Understanding how fracture of nanocomposite materials is related to filler volume and size [1], (2) Raman imaging of graphene on silica to determine the intrinsic doping.in the context of explaining photoconductivity of doped samples [2], (3) Supervision of a Diploma student, Christian Malm (now PhD student at the Max Planck Institute for Polymer Research) in his work focused on spectroscopic and rheological properties of simplified, bottom-up, and non-vulcanized nanocomposites.

1.2 Basics of elastomer based nanocomposites

1.2.1 Structure of elastomers

Literally, "poly" and "mer" mean "many" and "parts", respectively. Looking deeper into the etymology, numerous groups of atoms form a "part" of a polymer called a monomer. A polymer macromolecule is generally accepted to consist of more than ten covalently bonded (repeating) monomers. In Figure 1-1, different configurations of repeating units of polybutadiene are shown. Letters n, k, and p indicate the average number of different monomers in a polybutadiene macromolecule. Even if the number and type of atoms are the same for each of these monomer units, it is very important to identify the number and position of these monomers along the chain. For example, a chain with different ratios of monomers (n,k,p) but the same molecular weight can have very different chain 3D spatial arrangement, or conformation. Similarly, the positioning of the n, k, and p subunits along the chain – whether random or in so-called "blocks" – also drastically affects chain conformation. Chain confirmation ultimately affects mechanical properties (e.g., softening or hardening) of polymers in networks. For instance, a large number of possible conformations (or a floppy polymer) makes the polymer more flexible compared to a chain with less confirmations.

Φ_1 and Φ_2 in Figure 1-1 indicate the terminal (end) groups. Independent of the conformational structure, polybutadiene is classified as a *homopolymer* since all the repeating units belongs to a single type of monomer. For instance, if we call one repeating unit – butadiene – as A, the final *homopolymer* has a structure of A – A – A – A – A – A and it is presented as $[A]_n$. However, many polymeric structures in nature and synthetic chemistry include more than one different type of monomer, and they are called *copolymers*. In this thesis, polymeric structures generally include two different kinds of monomers (e.g. A and B) distributed along the polymer chains randomly (*statistical copolymers*): A – B – A – A – B – B.

[1,4 - butadiene]$_{trans}$ **[1,4 - butadiene]$_{cis}$**

Φ_1 n   k Φ_2 p
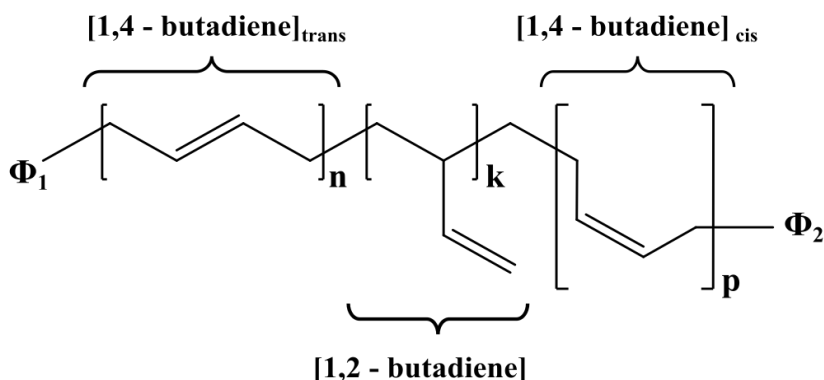
[1,2 - butadiene]

Figure 1-1. Molecular structure of polybutadiene.

In addition to chain conformation, multi-chain organization in networks strongly determines mechanical properties of polymer materials. Chain mobility can be tuned with temperature, giving polymer materials so-called thermomechanical properties. In different polymer systems, mechanical changes due to heating or cooling take place at two material specific thermal transition temperatures that are called the melt transition (T_m) and *glass transition (T_g) temperature*. In general, polymers are divided into three groups depending on their thermomechanical properties: (i) thermoplastics, (ii) thermosets and (iii) elastomers. (i) Polymers that get soft and fluid-like when they are heated over their T_m or T_g are called *thermoplastic*s, and they are considered rigid when sufficiently cooled below their T_g. The structure of the polymers in thermoplastics can be either fully amorphous (Figure 1-2a) or partly (semi) crystalline (Figure 1-2b) depending on their macromolecular chain structure, regularity and interactions.[3] When fully amorphous polymers (which have only a T_g) and even some crystalline polymer liquids (which potentially have T_g and T_m) are cooled quickly, both form amorphous "glassy" materials because the crystalline polymer molecules do not have enough time to form crystalline domains. Importantly; these materials can be <u>reversibly</u> heated into a molten state and molded. (ii) Polymers that get more rigid with increasing temperature, by increasing the number of cross-links, are *thermosets*. In thermosets, once the monomers are cross-linked (Figure 1-2d) at higher temperatures, they cannot be liquefied (or made molten) upon heating anymore. (iii) Polymers that have a T_g below room temperature, are also cross-linked, and exhibit genuine elasticity are called *elastomers* as illustrated in Figure

1-2c. Elastomeric structures also have cross-links but with lower density compared to the thermosets since cross-linking only takes place between the polymer chains not monomers. Due to the low density cross-links and the network like structure (similar to a spider web), elastomers can be elastically deformed to elongations up to approximately ten times the original dimensions. Because of the cross-links, elastomers do not flow under stress easily, and the material can assume its original shape after the stress release in all dimensions, assuming no plastic deformation. [3,4] It is these types of materials that form the basis of all the work presented in Chapters 3, 4, 5, and 6 of this thesis.
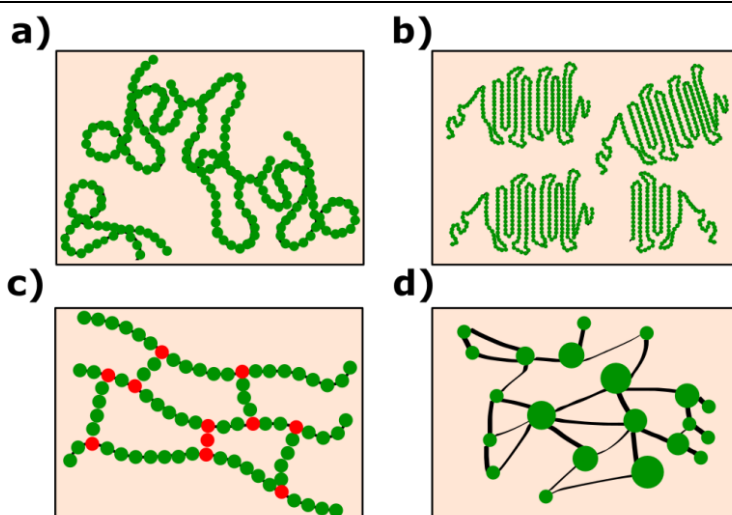
Figure 1-2. Illustration of macromolecular structure of (a) amorphous (b) semi-crystalline thermoplastics, (c) elastomers and (d) thermosets. All the structures are sketched by using green balls representing single monomers. Red balls represent chemical nodes in elastomer structure as the result of vulcanization (cross-linking).

Throughout this thesis and in the field of polymer science, one often hears the term "rubber-like" when referring to elastomers. The word *rubber* is a traditional way of referring to elastomeric materials, and these terms have often been used interchangeably. While rubbers and elastomers are very similar, an elastomer is *rubber-like* if it has the following three traditional properties which were first time proposed by L. R. G. Treloar in 1949:[4]

      (1)   long polymer chains consisting of freely rotating (jointed) links,

(2)   cross-links (e.g., chemical via vulcanization or physical via van der Waals contacts) between polymeric molecules,

(3)   forms a three-dimensional network as shown in Figure 1-2c.

Elastomeric molecules generally have high mobility (liquid like) under external forces (mechanical stress) in room temperature conditions (RT) thanks to their long polymer chains (and low T_g). Having the first condition alone without the other two requirements, materials behave like a liquid – they flow under constant stress. In order to control the motion of the polymer chains, the second and the third requirements are needed. Cross interactions between polymeric molecules partly impede liquid-like motion. Physical cross-linking in rubber usually originates from complex, geometrically entangled polymer chains and is stabilized by van der Waals forces. In addition to such physical cross-linking, chemical cross-links can also be introduced to rubber systems by process called vulcanization, which was discovered by Charles Goodyear in 1839.[4] During vulcanization, sulfur atom(s) chemically react at the active sides (e.g., C=C bonds along the polybutadiene molecule, see Figure 1-1) of the polymer molecules, and they build covalent nodes (red dots in Figure 1-2) in rubber network.[4] It is important to have sufficiently organized cross-links (nodes), as is illustrated in Figure 1-2c, to produce an elastomeric network where all the chains contribute to the total rubber elasticity.[4] When these three requirements are fulfilled the material is no longer a liquid, and it behaves like an elastic rubber.

1.2.2   Effect of fillers

Often, polymer-based materials are not composed of a single polymer component, and contain additives to modify and tune their mechanical properties. Materials made from more than one component that contain more than one phase – the polymer and e.g. inorganic particles – are called composite materials. In general, composite materials are divided into three groups: (1) *particulate-filled* composites including a discontinuous "filler" phase inside the continuous (polymer) matrix phase, (2) *fiber filled* composites, consisting of elongated or randomly distributed fibers inside of continuous matrix (such as carbon fiber), and (3) *skeletal or interpenetrating network* composites, which are a mixture of two continuous (percolated) phases. With these different formulations, it is possible to modify e.g., stiffness, strength, dimensional stability (especially in fiber-filled systems), toughness, mechanical damping, heat distortion temperature, gas and liquid

permeability, and even electrical conductivity and magnetic permeability of the polymeric matrices.

The work presented in this thesis focuses on *particulate – filled composites*, and the size of these fillers are in nanometer range. The general name of these nano-size (dimensions from 1 nm to 100 nm) inorganic filler loaded systems is *nanocomposites*. Thanks to their extremely high surface-to-volume ratio, very small amounts of these nanofillers are sufficient to tailor many of the characteristic properties of the continuous polymer matrix. The fabrication history of nanocomposites starts at the end of the 1980s by the researchers at Toyota who dispersed nano-sized clay platelets in nylon-6 polymer. They observed almost a 2-fold increase in tensile modulus and tensile strength of nanocomposite compared to that in nylon-6 alone. [5]

Many theories have been proposed to understand the basic physical origin of the macroscale properties of nanocomposites, but this remains an unresolved issue. This is mainly due to the structural complexity of nanocomposites, despite a wealth of experimental data on their mechanical properties. Previous studies have often focused on a single parameter e.g. T_g or elasticity but have not always related this with the underlying structure of the nanocomposite. In addition, flexible polymer physics theory, while well-suited to explain homogenous networks, is not sufficient to explain the physical principles of highly heterogeneous nanocomposites.

One important way to understand macroscale changes of nanocomposites due to nano-filler presence is to study the effect of the fillers on T_g of the continuous matrix. In nanocomposites, many theoretical[6,7] and experimental works[8,9] have shown that significant attractive and repulsive interactions at filler-matrix interphase makes the T_g of the nanocomposite higher and lower, respectively.[6–8,10] This finding has been explained in terms of the difference of polymer dynamics at the surface of the fillers compared to the bulk polymer not near any filler surface. In nanocomposites having attractive interfacial interaction, polymer chains at the filler surface form a stable and low-mobility "layer" that has higher T_g compared to the T_g of the bulk polymer. This trend is reversed for systems having repulsive interaction between fillers and matrix. One might ask: Why is T_g particularly important on nanofilled systems but not in the microfilled composites? The answer lies in the relative size difference of an average polymer chain and the filler as shown in Figure 1-3.
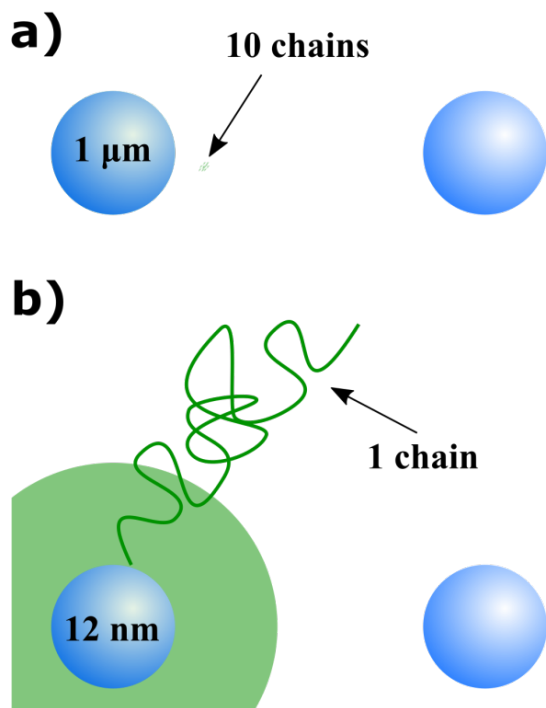
Figure 1-3. (a) Illustration of relative size of 10 polymer chains (R_g = 35 nm) together between two micro particles with diameter of 1 μm. (b) Single polymer chain (R_g = 35 nm) between two nanofillers having 12 nm diameter. For both illustrations perfect distribution of 3.5 vol % fillers is sketched and the average distance between the centers of micro and nano fillers are about 3 particle diameters.

For nanoscale fillers, the contact area between fillers is much larger than for microscale fillers. Thus, the "layer" effect on T_g of the final microfiller composite is negligible compared to the nanocomposite.[10,11] The cartoon presenting the micro- and nanocomposites in Figure 1-3 shows the size of the polymer "layer" on a filler (green colored area in Figure 1-3b), which is ca. 10 nm – seemingly independent of the molecular mass, size and the amount of filler.[12] While Figure 1-3 shows a perfectly distributed filler population within the matrix, this is (almost) never the case – either for micro- or nanocomposites. Work shown in Chapter 3 and Chapter 5 will clearly demonstrate this point, and optimizing the filler distribution in the matrix is a very active research area.

1.3 Molecular picture of nanocomposites

In this section, I will introduce certain molecular scale properties of nanocomposites based on two different kinds of elastomers: (1) acrylonitrile-butadiene rubber (NBR) and (ii) styrene-butadiene rubber (SBR). Fumed silica (SiO_2) nanofillers are used in these formulations with a wide range of primary size (from 12 nm to 30 nm). Importantly, T_g of both rubbers and their composites are significantly lower than RT (ca. -30 °C).

1.3.1 Nanofiller dispersion

As indicated in the previous section, the interface between nanofiller and polymeric matrix has a direct effect on the mobility of the polymer molecules close to the filler surface, and this is a critical property for varying linear and non-linear viscoelastic properties of the nanocomposites.[13–16] Beside mechanics, filler dispersion and the interfacial interaction between filler and matrix also changes optical,[17,18] electrical,[19–21] biological properties[22,23] of the nanocomposites. Given this importance, we should ask ourselves the following questions: 1) how can we control the dispersion of the fillers, and 2) how can the dispersion be quantified?

Silica and carbon black are the most common used nanofillers in elastomer-based nanocomposite formulations in industry due to their low cost and good processability. In early filled elastomer technologies, particularly the car tire industry, carbon black had been used for many years as reinforcing agent. However, starting from the early 1990s, significant car tire performance improvements in terms of wet grip and rolling resistance have been detected by replacing carbon black with silica nanofillers.[24–26] Compared to carbon black, the biggest drawback of silica nanofillers is that they have numerous silanol groups on their surfaces which make them highly polar and hydrophilic. Therefore, silica nanofillers tend to gather – aggregate – when they are mixed inside of hydrophobic polymeric matrices. In what follows below, I will introduce different methods to quantify nanocomposite microstructure and specifically filler dispersion. Two fundamental methods, (i) electron microscopy[27–31] and (ii) x-ray scattering methods.[17,32–37] have the appropriate spatial resolution, penetration, and provide sufficient contrast between fillers and the matrix. Even though transmission-electron microscopy (TEM) is most widely used since it is relatively

simple and fast, small angle x-ray scattering (SAXS) is the most precise method to quantify filler dispersion. Primary particle detection within filler aggregates by TEM is challenging due to the overlap of these aggregates into massive fractal structures. However, because scattered intensity is detected over a wide range of scattering angles (corresponding to different length scales), SAXS is better suited to resolve particle size distributions from the single filler to larger aggregates. While advantageous, the interpretation of SAXS data is subject to a model for the structure factor, which is still a very active area of research. Without a well-grounded model, it is very difficult to properly glean all the information from a SAXS spectrum. SAXS is also challenging in "true" industrial composites, into which typically multiple types of inorganic particles e.g. fillers, or catalysts are incorporated. This was the case in all NBR composites examined in this thesis (see Chapter 2 for more details). In this case, TEM was better suited to quantify aggregate size because electrons scatter more when they travel through the crystalline ZnO compared to silica aggregates. Hence, these two different inorganic structures have different contrast in TEM image and can be distinguished in the subsequent analysis.

In order to overcome the disadvantages of both TEM and SAXS, much recent work has focused on combining the two methods and simplifying the nanocomposite formulations. For example, Baeza et al. removed all the sulfur-containing molecules related to vulcanization and ZnO in order to simplify the formulations and to obtain more precise information about the filler distribution. [38,39] However, removing each ingredient from the original recipe is not desired in industrial nanocomposite research since each of these ingredients has an impact on the final characteristics of nanocomposites. In Chapter 3 and Chapter 4 we discuss in detail our TEM method and image analysis technique for calculating the average aggregate size of the full industrial nanocomposite formulations without simplifying them. Additionally, we show the consistency between our SAXS and TEM results for simplified and industrial formulations.

1.3.2   Chemical methods to control filler dispersion

With methods in place to quantify the nano-filler distribution in the polymeric matrix, now it is possible to address the second question: how can we control the dispersion of hydrophilic inorganic fillers inside of hydrophobic matrix? Two primary methods are used in elastomer-based nanocomposite systems to control the dispersion of the silica nanofillers. The first method is covalent coupling

between the silica surfaces and active groups on the polymers. This, in turn, can be achieved in the two ways shown in Figure 1-4: 1) via silanes attached to the silica, which then couple to the polymer, and 2) direct attachment via end or side functionalized silanol (Si-OH) groups on the elastomer chain. [30,40] The second strategy to control the dispersion is by changing the surface polarity of the fillers.[41,42] These different strategies, as related to the materials in this thesis, are illustrated in the Figure 1-4.
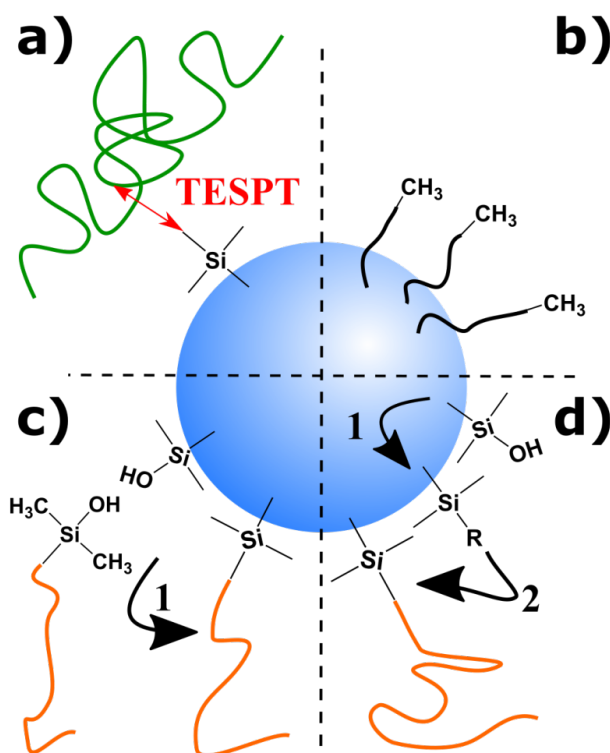
Figure 1-4. Illustration of a single silica particle with possible surface treatments in order to improve the filler dispersion inside of the polymeric matrix. Curved arrows and numbers next to them in (c) and (d) represent the sequence of the treatment steps. R is the initiator used for grafting on polymerization which takes place on the filler surface.

In Figure 1-4a chemical bridge between filler and polymer is mediated by the multifunctional silane, bis[3-(triethoxysilyl)propyl] tetrasulfide (TESPT). This method is a popular method for improving the filler dispersion in the nanocomposite industry, e.g. in car tires. The major drawback of this method is the

high cost of TESPT molecules.[40] Therefore, especially in the tire industry, research has focused on finding other methods, including changing the surface polarity of hydrophilic fillers by using different short hydrocarbons and silanes (Figure 1-4b),[41–44], polymerizing molecules by initiating them on the filler surface[45] (Figure 1-4d), or by modifying the end group of the elastomer chains for direct coupling to the filler surface (Figure 1-4c).

Among all these strategies, modified – functionalized – groups at the end or side groups of the polymer chains is gaining interest by industrial producers.[38,39,46] In recent works, it has been reported that the size of silica nanofiller aggregates could be controlled in SBR by changing the ratio of chains with functional groups to those without functional groups.[38,39] These works have shown that even a low concentration of chains with functional groups (25 % of the total end groups of SBR molecules) was sufficient to tune the filler distribution and thus the non-linear viscoelasticity of complex SBR based nanocomposite systems.[47] However, an unambiguous picture of the chemistry at the polymer-filler interface (such as that illustrated in Figure 1-4c) is not easy to obtain.

1.3.3   Measuring interfacial chemistry between fillers and matrix

It is particularly challenging to quantitatively (or even qualitatively) describe the nature of the interaction between fillers and the matrix. Is the interaction between the intended partners covalent or non-covalent? Making drawings like those in Figure 1-4 is straightforward (known as "Powerpoint Science"), but actually proving these bonding interactions is not straightforward, especially in complex industrial composites. In my department at the Max Planck Institute interface-specific spectroscopic methods have been developed that can provide information on the interface between polymer and silica surface. Three techniques are discussed in this thesis: (i) Sum Frequency Generation (SFG) spectroscopy, (ii) near edge x-ray absorption fine structure (NEXAFS), and (iii) X-ray photoelectron spectroscopy (XPS). The latter two are ultra-high vacuum techniques whereas SFG is an ambient environment spectroscopic tool to determine interfacial molecular structure of materials. All of these methods are sensitive to (sub) monolayer quantities at the surface/interface. NEXAFS and SFG are also sensitive to the orientation of molecules at the interface/surface while SFG is exquisitely sensitive to the ordering of the functional groups at the interface. [48–52] XPS is a truly quantitative tool that provides chemical composition in atomic % and probes the upper few tens of

Angstroms [53–55] of an interface, and importantly for this thesis, it is possible to use depth profiling by using argon ions or clusters to drill into a material. The physical background of SFG, NEXAFS and XPS will be provided in Chapter 2. In Chapter 4, we will show how we studied a model system to clearly identify interfacial chemistry between functionalized SBR and fillers using these surface-sensitive spectroscopic methods.

Figure 1-5. **S**train (ε) response of materials with ideal (a) elastic, (b) viscous and (c) Burgers viscoelastic behaviors under an instantaneous stress (σ_0) applied between times 0 and t'.

1.4   Resistance to deformation of nanocomposites

1.4.1   Viscoelasticity of polymers

The goal of creating nanocomposites is to improve their mechanical properties, often their resistance to deformation or applied loads. For a purely elastic material, such as an ideal spring, this property is called elasticity; however, polymers are not purely elastic, hence they are termed viscoelastic. To understand the term viscoelasticity, we first need to define the roots of this word, which are viscous and

elastic. Viscous, elastic or viscoelastic response of the materials can be detected by creep tests, which measure the time-dependent strain in response to a (constant) step stress. A purely *elastic*, purely *viscous* and *viscoelastic* response of a material due to applied constant stress (σ_0) (between times, 0 and t') are illustrated in Figure 1-5. Strain response of a purely elastic (Hookean) material increases instantaneously with force and stays constant till the force is removed (t=t') (Figure 1-5a). For the ideal (Newtonian) viscous material, the strain increases *linearly* with increasing time as long as load is applied to the material. After removing the load from the system (t'), strain in purely viscous material remains constant unless a further load is applied (Figure 1-5b). Viscous deformation is called non-reversible (plastic) since there is no recovery. In viscoelastic materials, the material presents the strain response of both elastic and viscous material (Figure 1-5c). The curve in Figure 1-5c is called the Burgers model, which has been used to explain viscoelasticity of many thermoplastics.[56] More details of using spring and dashpots for understanding the elasticity of nanocomposites are explained in Chapter 2 (section 2.2).

Differently from many other polymers (glassy and semi-crystalline) having viscoelastic behavior, an "ideal (cross-linked) rubber" mechanical response is almost completely dominated by the elastic response. Long and freely rotating rubber molecules are highly entropic and thus under deformation rubber behaves elastically.[57] Moreover, rubber based composites used in this thesis are cross-linked (vulcanized, see Figure 1-2c) and cross-linked network structure further enhances the elastic behavior of the material since the rubber molecules cannot slide over each other easily during their deformation.

1.4.2   Deformation under static forces: tensile testing

Static mechanical testing methods are used for measuring the force response of material under stretching, compressing, or shearing at a constant rate. In this thesis, we routinely performed static mechanical tests of our samples using *tensile tests*, as well shear to a lesser extent. For a typical tensile test measurement, a material is cut in the form of a dog bone (or dumbbell), which is shown as inset in Figure 1-6a, and it is fixed at one end while the other end is pulled with a constant rate of elongation (strain rate) until the sample fractures. The measures of stress and strain are divided in two main groups as "engineering" and "true". The *engineering stress (σ_{Eng})* and *engineering strain (ε_{Eng})* are calculated from the measured load (F), original (initial) cross-sectional area (A_0) of the center of the

specimen (black shaded area in the illustration of Figure 1-6a inset), original length (L_0) and displacement during stretching (ΔL) of the specimen as,

$$\sigma_{Eng} = \frac{F}{A_0}, \varepsilon_{Eng} = \frac{\Delta L}{L_0} \qquad (1.1)$$

However, at high strain levels, the engineering stress-strain curve is not accurate since stress is not calculated using the actual cross-sectional area of the material (which changes during deformation). As a solution, the stress-strain response of the sample can also be reported in terms of *true stress (σ_{True})* and *true strain (ε_{True})*.

$$\sigma_{True} = \frac{P}{A}, \varepsilon_{True} = \int_{L_0}^{L} \left(\frac{1}{l}\right) dl = ln\left(\frac{L_0 + \Delta L}{L_0}\right) \qquad (1.2)$$

The true stress reports the measured load at each strain divided by the *actual* cross-sectional area, A, rather than the initial value A_o. Since the actual cross-sectional area decreases as the sample elongates, $\sigma_{True} > \sigma_{Eng}$. In elastomeric materials the volume of the sample is assumed to not change during deformation, and the σ_{True} can be related to the σ_{Eng} simply as,

$$\sigma_{True} = \sigma_{Eng} \left(\frac{L_0 + \Delta L}{L_0}\right) \qquad (1.3)$$

An exemplary engineering stress-strain curve of a ductile material is shown in Figure 1-6b. In very short displacement range of σ_{Eng}-ε_{Eng} curve of many materials stress linearly increases with strain and type of deformation in this range is called *elastic deformation* (Figure 1-6b). In elastic deformation range, the material obeys Hooke's law and the constant of proportionality is the modulus of elasticity or *Young's modulus E*:

$$\sigma_{Eng} = E\varepsilon_{Eng} \qquad (1.4)$$

With the increasing strain, many materials diverge from this linear regime at a specific point, called the proportional limit. At higher strain beyond the proportional limit, the material shows a non-linear stress-strain relation, which is called *non-linear elasticity*. In many ductile materials, especially ductile polymers, it is very challenging to pinpoint the exact starting point of non-linear elasticity region in terms of stress. Therefore, the yield stress (σ_Y) has been defined as the accepted location where non-linear deformation starts in a material during tensile testing. σ_Y is found by sketching a line from the strain axis at ε_{Eng} = 0.2 % that has the same slope of that which defines the initial Young's modulus. This is shown schematically in Figure 1-6b. The intersection of this line with the engineering stress-strain curve is defined as the yield and marks the σ_Y. In other sources, this offset value is 0.1 %.
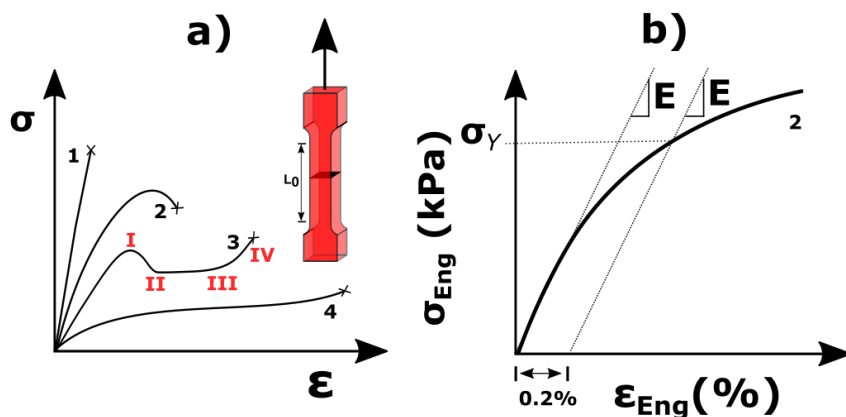
Figure 1-6. (a) Typical stress (σ)-strain (ε) curves of different polymeric samples having brittle fracture (curve 1), ductile fracture after a neck formation (curve 2), ductile fracture with cold drawing and orientation hardening (curve 3), and rubbery deformation which shows the strain-induced crystallization (hardening) prior to failure (curve 4). Cross marks at the end of each curve represent the fracture points. Roman numerals in curve 3 illustrate different deformation stages of a ductile polymer via stretching. Dog bone shape specimen used for the tensile test illustrated as an inset. (b) Low – strain region of a stress – strain curve of a ductile material, showing also the yield stress.

   In Figure 1-6, I summarize typical stress-strain curves of different types of polymers by their deformation behaviors in RT condition tensile tests. A stress-strain curve of brittle and hard polymers is presented by curve 1 in Figure 1-6a. Both amorphous and semi-crystalline polymers can show such a curve if their mechanical tests are performed at a temperature well below their T_g. These polymers have linear stress-strain behavior over nearly the full range of deformation, which eventually ends with a fracture prior to any plastic flow. Stress-strain characteristics of many engineering thermoplastics are presented by curves 2 and 3 in Figure 1-6a. In curve 2 and 3, at the initial part of the deformation, stress increases with increasing strain and after a certain strain level, stress begins *decreasing* with the increasing strain. The strain level for which the stress reaches its maximum value (i.e. where $d\sigma/d\varepsilon = 0$) in both curves is called the ultimate tensile stress (UTS). After UTS, first the stress shows a drop (decrease) with further increasing strain, and this process is called *strain softening*. The minimum stress in this softening regime is called draw stress, and at this point, material either fractures (curve 2) or starts getting harder due to *orientation hardening* (curve 3)

24

immediately before the fracture. In general, during orientation hardening or *strain hardening* polymer chains are aligned to the direction of loading, and the system shows increasing resistance to further deformations (strain). Depending on the polymer type, it is possible to have permanent, non-catastrophic – plastic – deformation. In ductile polymers (but not in elastomers), such a process happens between the UTS and strain level where orientation hardening starts (point IV on curve 3 in Figure 1-6a), and the shape of the specimen changes. After UTS, the central width of the dog bone decreases in a process called *necking* (between points I and II on curve 3). After the neck formation, the sample extends along its length and the cross-section of the necking region gets smaller at the same time (between II and III of curve 3) and this process is called *cold-drawing*. For the samples showing orientation hardening before their fracture (between III and fracture points (IV) of curve 3), necking (decrease in the size of width) gets stabilized when the orientation hardening starts. During the orientation hardening, only the neck propagates from the center of the specimen along the gage distance outward until the sample fails.[5,3]

The stress-strain behavior of a typical elastomer rubber is shown by the curve 4. These rubbers have the smallest modulus but the highest extension ratio compared to the others systems in Figure 1-6a. Before the fracture of rubber, similar to other ductile polymers (curve 3), the cross-linked rubber molecules align to the loading direction, and the material shows the effect of strain hardening prior to fracture. In ductile and rubbery polymers, strain-hardening is a very crucial parameter for understanding the mechanical behavior of these materials in cyclic, high-stress environments and during extended periods of mechanical deformation.

It is important the note that the preceding discussion and Figure 1.6 was in the context of *pure* polymer matrices and NOT in the context of composite materials. The effect of nanofillers on the elasticity strain-hardening characteristics of the rubbers will be discussed in Chapter 5. Additionally, further details of tensile test analysis, for instance Gaussian statistics of rubber molecules, and observation of the modulus of strain-hardening in ductile polymer and nanocomposite systems will be discussed in Chapter 2.

1.4.3   Reinforcement

As mentioned before, the main reason for including fillers (carbon black or silica) in rubber is for improving the mechanical properties of the rubber. For instance,

improving the lifetime of rubber used in car tires can be done by preventing the rupture failure due to fatigue, which occurs during the wear of the rolling tire.[58] Increasing not only the fatigue resistance, but also modulus, rupture energy, tear strength, tensile strength, cracking resistance and abrasion resistance can be done by increasing the linear elastic (storage) modulus of the rubber, or its *reinforcement*, by including fillers among other ingredients. [59,60] Reinforcement of a filled elastomer system can be observed from the linear portion of a storage modulus versus increasing shear amplitude graph, which is obtained from the dynamic mechanical tests (DMA) (Figure 1-7a). The theory of DMA is introduced in Chapter 2 (see section 2.2). Obtaining higher reinforcement (increasing the storage modulus in the linear deformation regime) is a very complex phenomenon depending on two main parameters: (i) arrangements of the fillers in the polymeric matrix and (ii) interaction between the fillers and the polymeric matrix.[10] As explained in section 1.3, the complex interaction between fillers and polymer molecules influences the size, shape and aspect ratio of the filler aggregates and such changes in the filler nature have a direct impact on the composite reinforcement.[61] For rubber-based composites filled with very low concentrations of fillers, in which there is no risk of having particle – particle interaction, it has been found that reinforcement linearly scales with the filler concentration. However, at higher filler concentrations the reinforcement gets more sensitive to the filler aggregate size.[58] In systems containing a similar amount of fillers with different aggregate sizes and with the possibility of direct interaction between rubber molecules and fillers, a higher reinforcement is observed for the sample with smaller aggregates compared to that with larger aggregates. This is explained in terms of having stronger interaction between matrix and fillers in the better dispersed system owing to the larger surface area between the aggregates and matrix compared to that in the other sample with bigger aggregates.[32,62] On the other hand, reinforcement gets more efficient when the fillers are in the shape of complex structures (e.g., branched or fractal) rather than being dispersed perfectly in the rubber.[58,63,64] A precise and straightforward relation between filler dispersion and reinforcement involves many different criterions and is still not completely understood. This topic will be addressed further in Chapter 3.
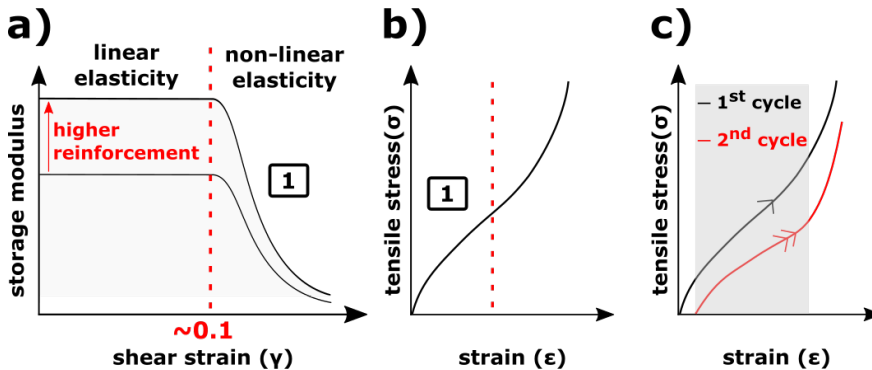
Figure 1-7. (a) Example storage modulus of two different filled rubbers having different viscoelastic properties – reinforcement and nonlinear softening. The storage modulus is linear to the left of the red dashed line and non-linear (via the Payne effect) to the right. Typically ~ 10% shear strain is the critical shear deformation where the sample starts responding to the further deformation non-linearly. (b) Typical tensile stress-strain behavior of a filled elastomer until fracture. Non-linear elastic softening (Payne effect) and hardening are separated by red dashed line. Both in (a) and (c), the boxed "1" mark the regions in the illustrated data where the Payne effect is observed. (c) Example of the Mullins effect by showing tensile stress-strain curves of a rubber material in 2 cycles. The region where the Mullins effect is observed during the second stretching is shown in the borders of the shaded area (grey color).

1.4.4 Payne and Mullins effect

The non-linear softening response of rubber and rubber-based samples is called the *Payne* or *Mullins* effect, depending on its origin.[65,66] The Mullins effect is the stress softening of filled, and even some unfilled, rubbers in the stress-strain curves over multiple cycles as shown in Figure 1-7c. The Payne effect is stress softening observed at moderate strains. This is shown in Figure 1-7a for a DMA measurement and in Figure 1-7b for a tensile test. In literature, the following factors have been invoked for explaining such softening response of the materials: (i) disentanglement of the rubber molecules physically, (ii) reduced interactions between filler and the rubber molecules, (iii) breakdown of the filler network and (iv) chain scission in rubber molecules.[10] Because the both the Payne and Mullins effects are observed in tensile cyclic loading experiments (Figure 1-7c), it is not easy to define which effect is dominant. In order to avoid this confusion, the Payne

effect has been defined as *reversible* strain softening whereas the Mullins effect is defined as *irreversible* strain softening. [67] In contrast, the Payne effect is only observed in filled rubber systems and it gets more prominent with higher concentration of fillers. Furthermore, Payne effect is clearly observed under oscillating loads at very small strain amplitudes whereas the Mullins effect is observed at substantially higher strain levels (outside of the region number 1 in Figure 1-7b) in more than one cycle of tensile loadings. Both softening features are of significant importance in industrial nanocomposites such as car tires, with regards durability, grip, and rolling resistance.[68]

1.5   State of order in polymers and composites

Understanding the orientation of polymer molecules is a fundamental requirement for explaining various macro-scale properties of polymer materials and polymer based composites, most importantly their mechanical properties.[69] As previously mentioned, strain hardening of many polymeric materials under uniaxial stretching is correlated to the dynamic alignment mechanism of the polymer molecules along the loading direction. In cross-linked rubber materials at high strain level, it is important to connect their mechanical and/or swelling behaviors to their strain induced crystallization caused by molecular orientation. This helps explains their deformation mechanism particularly prior to their fracture (strain-hardening).[70] Moreover, in order to design new polymeric materials with superior physical properties (e.g. directional stiffness in composites), the relation between orientation behavior and the properties in polymer films or fibers has significant importance.[71] For nanocomposites, the presence of nanofillers in polymers certainly affects the macromolecular orientation of these polymers due to (i) their large surface area, (ii) interfacial interactions between fillers and polymer and (iii) impeding the motion of the polymer chains close to the filler surface (bound layer).[71–76].

Different methods to measure chain orientation *in situ* are NMR spectroscopy, x-ray diffraction, polarized fluorescence or optical birefringence, Raman and Fourier transform infrared (FTIR) spectroscopies.[77–79] Among these methods, optical birefringence is often preferred for measuring the orientation of polymers. However this method cannot discriminate the anisotropy of oriented molecules between crystalline or amorphous phases of a homogenous polymer or different phases in a heterogeneous polymer because there is no molecular

specificity.[77] For instance, at a certain deformation of a semi-crystalline polymer, it is known that the deformation stages of different phases are different and it is important to understand the connection between total polymer deformation and the chain anisotropy of specific molecules in different phases.[80–82] In the same way, x-ray scattering, while able to discriminate between crystalline and amorphous phases, is limited to observe the orientation in the amorphous phase unless there is strain-induced crystallinity and also has no molecular specificity. Polarized Raman spectroscopy and Fourier transform (FTIR) dichroism are the two most useful methods since they provide orientation data of specific molecular groups within chemically and/or conformationally different chain segments of polymers with or without fillers inside. Owing to the molecular level sensitivity of these vibrational techniques, certain deformation of polymeric samples under stretching can be explained in terms of molecular alignment.[83]

Using x-ray scattering and IR dichroism methods, the direct relation between clay nanofiller content and chain orientation of various polymers like PS,[73,84] polyamide 6 and [74] polyurethane (PU) [75,76] has been studied by monitoring the alignment of the polymer molecules via tensile deformation. However, these studies could not simultaneously measure polymer chain orientation during mechanical deformation. This limitation was because T_g of PS and Polyamide 6 are higher than the RT, so the nanocomposites first were heated, stretched at high temperatures and then they were cooled down to room temperature to measure spectroscopic alignment measurements. In contrast, the PU had a lower T_g than RT, so they could be stretched at RT while measuring chain alignment. However, the PU was not crosslinked and was therefore not stable at RT during deformation. The authors allowed 15 minutes of "stress-relaxation", after stretching PU samples, before measuring chain alignment.[76,85] Hence, there is a need to measure chain alignment under simultaneous deformation, especially in elastomeric systems.

Fortunately, vulcanized nanocomposite rubber systems such as SBR and NBR, which also have very low Tg (ca. -30 °C), are stable under RT conditions (no flow) thanks to their cross-links (vulcanization). Therefore, they can be stretched at RT without the need for any additional procedures (heating or stress-relaxation). While these properties make elastomer materials attractive to investigate the mechano-chemical alignment, there are two major challenges compared to non-crosslinked thermoplastics: (i) Segments of chains in elastomeric networks are cross-linked to each other and are not as independent as non-crosslinked polymeric

chains. (ii) Random cross-linking causes some imperfections or defects in rubber macrostructure such as physical entanglements, looping (pinning of single chain to itself) and terminal chains.[3] Such imperfections make the elastomer alignment mechanism less uniform. In Chapter 5, the alignment of the elastomeric networks along the loading direction, and the effect of fillers on chain anisotropy was quantified with polarized Raman micro-spectroscopy and quantification of molecular order for particular vibrational modes. The technical details of deciding which vibrational modes to study, and the statistical strategies for showing the chain anisotropy will be presented in Chapters 2 and 5.

CHAPTER 2: MATERIALS & FUNDEMENTALS OF METHODS

2.1 Materials

The nanocomposites used in this work are classified in two main groups: (i) *full nanocomposites* and (ii) *simplified nanocomposites*. Chemical formulation details of the full nanocomposites will be explained to the extent that is possible while respecting the intellectual property of our industrial collaborators who produced these samples. Full nanocomposites are further classified by their polymeric matrix types which are styrene – butadiene rubber (SBR) and acrylo-nitrile-butadiene rubber (NBR). Simplified nanocomposites were produced only with SBR materials. In the following, a brief description of the different composites is presented.

Styrene – Butadiene Rubber (SBR) /silica full nanocomposites

SBR (M_w = 1.5 – 1.6 · 10^5 g/mol, T_g = -32 °C) / precipitated silica (Zeosil 1165 MP, primary particle size, R_p ≈ 12 nm, surface area ~ 160 m^2 / g, from Rhodia®) full nanocomposites and neat SBR without fillers inside were synthesized in Michelin® laboratories. [47] Due to presence of end-group functionality, SBR rubber was divided into two classes. As shown in the Figure 2-1, SBR carrying the silanol (Si-OH) end functional group is called *functionalized SBR (F-SBR),* and SBR without any functional group is called *bare SBR (B-SBR)*. The functionalized end-group of F-SBR is chemically written as SBR–SiMe$_2$–OH (Figure 2-1b). The functional group fraction in one end of all F-SBR chains has previously been reported to be greater than 98% according to the results from 1H and 29Si NMR. [47] In the same study, the composition of both F-SBR and B-SBR were shown to be similar to each other due to their identical polymerization steps (anionic polymerization).[47] Both types of SBR were statistical copolymers consisting of 26 wt % of styrene and 74 wt % of butadiene units (41 wt % of 1,2-butadiene and 59 wt % of 1,4- butadiene units). The structures in Figure 2-1(a) and (b) denote the number of each subunit using the letters m, n, k and p for styrene, 1,2-butadiene, *trans*-1,4-butadiene and *cis*-1,4-butadiene monomers, respectively. The ratio of *trans*-1,4-butadiene to *cis*-1,4-butadiene ratio is not known, and it is not crucial for the content of this thesis as it is the same for B-SBR and F-SBR. Gel permeation chromatography (GPC) of the

polymer showed the M_n and polydispersity index (PDI) of both stock polymer solutions in THF (Mn ~ 150–160 kDa, PDI ~ 1.08–1.11) to be very similar to each other, and very close to values previously reported for identical SBR polymers. [47]
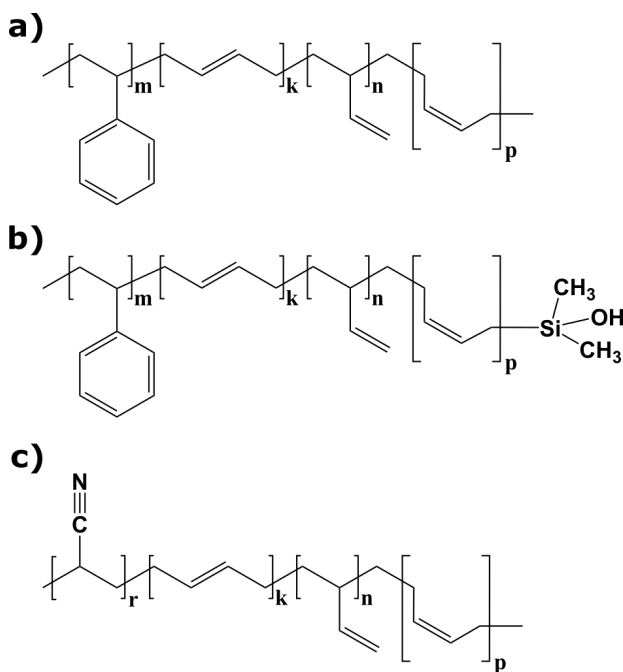
Figure 2-1. Molecular structure of (a) B-SBR, (b) F-SBR and NBR. Letters next to the brackets indicate the number of repeating units in each rubber.

To produce full composites from these SBR polymers, the polymers were mixed with many other components in the melt state. A mixing chamber was heated to 160 ± 5 °C, and the rotor speed in the chamber was kept between 95 and 105 rpm to blend the composites into a uniform mix. The components were added to this chamber in the following way: 1) lamellas of SBR polymer were cut into small pieces and then added to the chamber and 2) after ~ 1 min, a mixture including silica fillers with different amounts (see Table 2-1), catalyzer for vulcanization of SBR (diphenyl guanidine (DPG), 2 wt % with respect to the silica), coating agent (octyltriethoxysilane (octeo), 4 wt % with respect to silica) and coupling agent (bis[3-(triethoxysilyl)propyl] tetrasulfide (TESPT or Si69), 4 wt % with respect to silica)) was added to the chamber and mixed for an additional 4 min. The hot sample was taken out of the reaction chamber and quickly cooled and

laminated by rolling the samples 10 times through a 1 mm gap between rotating cylinders (two roll mill). The laminated mixture was then vulcanized (cross-linked) as a final step of the production.

Table 2-1. Type, amount of the ingredients and possible interfacial interactions in all the nanocomposites used in this thesis

		Synthetic parameters			Interfacial interactions
		Type of rubber	Filler radius : surface area per weight	Filler amount (vol %)	
Full nanocomposites	Silica / SBR	F-SBR B-SBR	12 nm : 160 m^2/g	3.5 6 16 21 24	• Coupling • Coating • Silica – F-SBR
	Silica / NBR	NBR	28 nm : 55 m^2/g 20 nm : 130 m^2/g 15 nm : 180 m^2/g	3 8 14 22.5	X
Simplified nanocomposites	Silica /SBR	F-SBR B-SBR	6 nm : 200 m^2/g	16	• Silica – F-SBR

Acylonitrile – Butadiene Rubber (NBR) / silica full nanocomposites
Precipitated silica (Evonik®, Essen, Germany) / Acrylonitrile Butadiene Rubber (NBR, M_w = 2.5·10^5 g/mol, glass transition temperature, T_g ≈ -36 °C) full nanocomposites were produced at SKF® Elgin, USA. NBR rubber was synthesized as nitrile elastomers via emulsion polymerization of 1,3-butadiene and acrylonitrile (ACN) with the monomer ratio of 28:72. In NBR nanocomposites, the primary size of the

filler particles was changed in different composites. Sizes, surface areas, and amounts of the three different size fillers are listed in Table 2-1. Similar to the SBR nanocomposites, NBR systems were also produced in melt in a mixing chamber; however, for reasons of confidentiality further production details cannot be provided. In general, NBR rubber (100 parts per hundred rubber (PHR)) was included with various amount of silica (see Table 2-1) for different nanocomposites. The amount of stearic acid (1 PHR), zinc oxide (ZnO, 9 PHR), rubber activator (2.5 PHR), sulfur (1.2 PHR) and accelerator for curing agent (2.5 PHR) were kept constant for all the formulations, and their amounts were not scaled with respect to the filler amount as was done for SBR formulations. Mixtures out of the reaction chamber were then vulcanized as a final step.

SBR / silica simplified nanocomposites

Non-vulcanized (dissolvable) F-SBR and B-SBR bulk slabs were dissolved in Tetrahydrofuran (THF, Sigma-Aldrich) and prepared as polymer stock solutions (40 mg/mL). These stock solutions were used after keeping them in a fridge (4 °C) for at least 4 days until a uniform and clear rubber solution (as seen by eye) was obtained. Fumed silica nanofillers (Aerosil 200, Evonik®, $R_p \approx 6$ nm) were used as received to prepare filler stock solutions (15.2 mg/mL in THF). After adding the fillers inside of THF, the solution was sonicated on ice with a probe-type sonicator (Branson Sonifier W450 digital, 1/2 inch diameter, 10 s, 60% amplitude) to promote dispersion of the fillers. To form the final simplified composite, a mixture of both filler and rubber stock solutions was prepared and mixed using the ultrasonic tip for 10 sec, 60% amplitude while keeping the mixture in an ice-bath. The final mixture was placed in a rotary evaporator (Rotavapor R-200, Buechi, Essen) at RT under 20 mbar for 30 min in order to remove THF. After retrieving the mixtures from the rotary evaporator, complete removal of THF was done by keeping the simplified nanocomposite mixture inside a vacuum oven (< 1 mbar) for 24h at 80 °C. In order to avoid any possible condensation reaction between the end-groups of F-SBR and the glassware, plastic ware was used for simplified nanocomposite production.

2.2 Experimental Methods

2.2.1 Tensile testing and rheology

Tensile testing and calculation of strain-hardening modulus

Uniaxial tensile testing of full nanocomposites was done using an Instron Universal Testing Machine (Instron 6022, Darmstadt). Slabs of nanocomposites samples with uniform thickness (ca. 0.2 cm) were cut into the small dumbbell shapes (length ≈ 1 cm, thickness ≈ 0.2 cm, width ≈ 0.18 cm). Cut samples were clamped to the tensile testing device by applying 5 bar of clamping pressure. No pre-strain was used and strain rate was kept 100 mm/sec for each measurement. Mechanical tests were terminated manually after the fracture of the composites. Three different tests were performed on each nanocomposite sample. Engineering stress (σ_{Eng}) and engineering strain (ε_{Eng}) were obtained from the tests and subsequently converted to true-stress (σ_{True}) and true-strain (ε_{True}), following the equations presented in section 1.4.2. The nature of the viscoelasticity of polymers is generally obtained by analyzing the tensile test response in the context of mechanical elements such as ideal springs as the perfect elastic (Hookean) element and dashpots as the perfect viscous element as presented in Figure 2-2a. The combination of ideal and nonlinear dashpots and springs shown in Figure 2-2a was proposed by Haward and Thackray [86] in order to replicate the tensile test response and explain the rubber elasticity in a tangible framework.[4] In order to apply this model to experimental tensile test results at large strain levels (far above the linear regime of the stress-strain curves), the following assumptions were made: 1) that the extension is dominated by strain from the non-linear deformation portion (ε_p) rather than linear (Hookean, ε_H) deformation and 2) that the material was incompressible, meaning that the Poisson's ratio was 0.5. In many stress-strain curves of rubber-based nanocomposites, the linear deformation region is usually impossible to detect as it only appears for very small strains. Therefore, we assumed the output of the tensile tests $\varepsilon_{Eng} \sim \varepsilon_p$ to calculate the extension ratio, λ, as shown below,

$$\lambda = \frac{extended\ length}{original\ length} \sim 1 + \varepsilon_p \sim 1 + \varepsilon_{Eng} \qquad (2.\,1)$$

a)

Hookean spring

$$\varepsilon_H = \sigma_{Eng} / E$$

Dashpot

$$\sigma_{Eng} - \sigma_{Eng(sp)}$$

$$\sigma_{Eng(sp)}, \varepsilon_p$$

$$\sigma_{Eng}$$

b)

L_0

OR

$$L_0 + \Delta L$$

$$\lambda = \frac{L_0 + \Delta L}{L_0}$$

c)

z_0

x_0

y_0

stretching

$z = 4 \ast z_0$

$x = x_0/2$

$y = y_0/2$
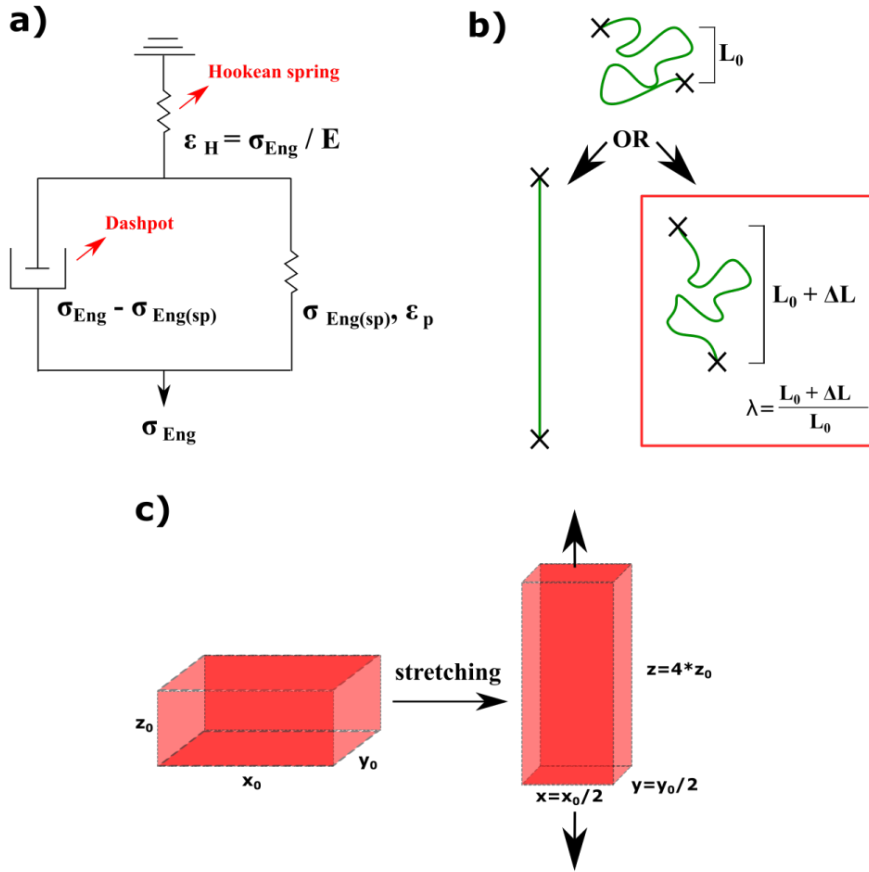
Figure 2-2. (a) Spring – dashpot model explaining the large strain deformation of ductile polymers. The system consists of one elastic (Hookean) spring connected in series to another spring and a viscous dashpot which are connected to each other in parallel. E, ε_H, σ_{Eng}, $\sigma_{Eng(sp)}$, ε_p represent Young's modulus, strain for Hookean spring, engineering stress applied to the system, engineering stress at spring parallel to the dashpot, strain at the dashpot and second spring together, respectively. (b) Illustration of polymer chain distortion under stretching explained in terms of Langevin and Gaussian equations. The Langevin equation is used when a polymer chain approaches the maximum extension between entanglements (straight line between two crosses). Gaussian deformation applies if the polymer chain behaves like a statistical coil and cannot fully extent under deformation (illustrated in red box). Extension ratio, λ of the coil is calculated by the formula shown as inset. In the formula, length difference between extended and original presented by ΔL. (c) Example of volume-conserved deformation of a polymeric material. The polymeric sample with initial dimensions of x_0, y_0, z_0 and after the deformation it takes on dimensions x, y, z.

The Haward and Thackray model can be applied in two ways, depending on the polymer chain extensibility at high strain levels (Figure 2-2b): (i) using Langevin equations by assuming the polymer chain can be extended until it becomes nearly straight at maximum elongation [87] or (ii) using Gaussian approximation by assuming that the polymer chains cannot be fully stretched at the highest strain level as illustrated in Figure 2-2b. Similar to what has been mentioned in the rubber literature, we do not expect a random crosslinked and very high molecular weight rubber molecule to stretch fully.[4] Hence, we employed the Gaussian modeling and used this model to find the so-called *strain-hardening modulus (Gₚ)* of our nanocomposites as,

$$\sigma_{True} = \lambda\sigma_{Eng} = G_p \left(\lambda^2 - \frac{1}{\lambda} \right) \tag{2. 2}$$

The derivation of equation (2.2), which invokes the entropic elasticity of individual chains, has been discussed elsewhere[3,4] and is based on the following fundamental assumptions:

1- Chain segments between two successive crosslink points of cross-linked network are envisaged as independent chains. The complete rubber network, which is subjected to a deformation, is made up with the same number of chains per unit volume.

2- Network is constructed by freely joined chains which follow Gaussian statistics.[3] Therefore, sum of the individual chain (single) entropies gives us the total entropy of the network.

3- Extension ratio of each chain during stretching is equal to the extension of the bulk network. In other words, network sustains an affine deformation.

4- Material does not change its volume during the deformation (Figure 2-2c).

2.2.2   Dynamic-Mechanical analysis: Rheology

Dynamic mechanical measurements were performed at University of Amsterdam – The Netherlands (UvA) by M.R.B. Mermet-Guyennet in Prof. Daniel Bonn's laboratory. An oscillatory rheometer (Anton Paar MCR 300) was used with different radii plate-plate geometries. For full nanocomposite samples, a superglue – Loctite 421 type – was used to improve the adhesion between the plates and the composite. During the rheology measurements, a sinusoidal shear strain was applied to the sample (strain-controlled measurements), which produces a stress response with similar frequency when the deformation is linear (Figure 2-3). The linear strain and stress response curves of rubber (or general viscoelastic materials)

are shown in Figure 2-3c. During the oscillatory measurement of the rubber, a fraction of the energy is stored elastically and the rest of it is dissipated as heat. The sinusoidal applied shear strain ($\gamma(t)$) is characterized by an amplitude (γ_0) and angular frequency (ω) as:

$$\gamma(t) = \gamma_0 \sin(\omega t) \tag{2.3}$$
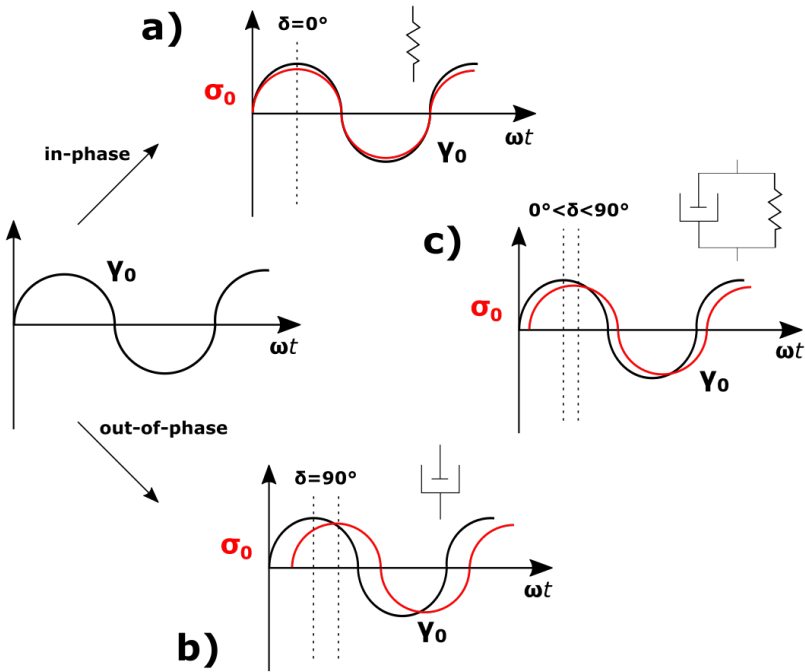
Figure 2-3. Representation of applied oscillatory strain (γ_0) and the oscillatory stress (σ_0) response of (a) perfect (Hookean) elastic, (b) perfect viscous (Newtonian) and (c) viscoelastic material.

Due to the viscoelastic nature of the rubber, the stress response of the rubber induced by the applied oscillatory strain has a phase shift (δ) and it can be described as follows:

$$\sigma = \sigma_0 \sin(\omega t + \delta) = \gamma_0[G'(\omega) \sin(\omega t) + G''(\omega) \cos(\omega t)] \tag{2.4}$$

where G' (called storage modulus) is the storage of the elastic energy , and G'' (loss modulus) quantifies the dissipated energy during the deformation. In perfectly elastic materials (Figure 2-3a), G'' is zero since energy is not dissipated and

completely stored by the material ($\delta = 0°$). At the same time, for perfectly viscous material (Figure 2-3 b), G' is zero since the stress and strain curves are perfectly out-of-phase ($\delta = 90°$). However, in viscoelastic materials G' and G'' are non-vanishing since the material has a stress response of both viscous and elastic origin. Thus, the phase shifts (δ) of the viscoelastic materials always lie between 0° and 90° (Figure 2-3c).

2.2.3   Filler aggregate size determination

Measuring aggregate size

Nanofillers in nanocomposites often aggregate into large amorphous masses during the formulation process. These aggregates are usually ~ 2-10 fold larger than the size of a primary filler particle but can extend to be 100-fold larger in certain cases (as we will see in SBR full composites). This corresponds to ~ 20 – 100 nm in most cases and ~ 1 µm in extreme cases. Furthermore, because the agglomeration process almost certainly takes place out of equilibrium, aggregates often exhibit an extremely high polydispersity. Optical microscopy cannot provide accurate images of nanocomposite aggregates due to diffraction-limited spatial resolution of visible light (Figure 2-4a). Higher resolution images showing dispersed fillers in the matrix – from the primary filler to giant agglomerates – can in principle be obtained using electron microscopy. In electron microscopy, the deBroglie wavelength of an electron is at most ~ nm and typically much lower (depending on the acceleration voltage varying from tens to hundreds of kilo-electron volts (keV)), which is why this technique is able to resolve nanoscale aggregates.

The two main electron microscopy techniques are *transmission electron microscopy (TEM)* and *scanning electron microscopy (SEM)*. In terms of the typical spatial resolution limits presented in Figure 2-4a, SEM lies between *optical microscope* and TEM. In Figure 2-4b, the basic mechanisms of SEM and TEM are explained by showing how the incident electrons interact with the sample. Prior to TEM imaging (JEOL JEM 1400, Eching), bulk nanocomposite samples were cut to 50 nm thick slices by ultracryotome (LEICA EM UC6, Wetzlar) and these slices were placed on top of copper grids. Ultracryotome was performed at -60 C° in order to cool the samples considerably lower than their T_g, which makes them highly brittle. TEM electron path **(1)** in Figure 2-4b shows electron beam transmitted through the thin sample lying on the top of a copper, which is the basic principle of TEM imaging. Electron transmission is not equal over the entire imaged area of the sample, providing the contrast difference between filler and matrix in TEM images.

Silica nanoparticles appear dark due to their high density and high electron scattering from their surfaces (electron path **(2)** in Figure 2-4b). Due to very low atomic density in polymeric matrices compared to inorganic fillers, incident electrons scatter less in the matrix phase. Therefore, as it is shown in the TEM image in Figure 2-4c, more electrons pass through the matrix compared to the regions of fillers, and thus high numbers of electrons are collected by detector (ED in the electron path **(1)** in Figure 2-4b). In Figure 2-4c, crystalline ZnO particles have the darkest contrast because they have the most electron-dense atomic structure.

The basic principle of SEM is represented by electron path **(3)**. In SEM, specimen surface is scanned with the focused electron beam and some of the electrons can go through the specimen (if the specimen is thin) while others are reflected from the surface of the specimen and are detected (ED on the electron path **(3)** in Figure 2-4b). As a consequence of the energy exchange between the focused electrons and the sample, reflected electrons can be grouped as secondary and backscattered electrons when the scattering is elastic and inelastic, respectively. The intensity of the reflected electrons changes due to the focused electron energy, the atomic (Z) number and density of the material at the focal point. Resulting SEM images show the distribution of the scattered electron intensity from the scanned area of the sample.[88] In both TEM and SEM, incident electron beam scatters some characteristic X-rays (path number **(4)** in Figure 2-4b) and such X-Rays can be detected by using additional X-Ray detectors (XD in Figure 2-4b). These scattered X-rays can be further analyzed to perform elemental analysis of the imaged surface in a technique called energy-dispersed X-Ray spectroscopy (EDX).

One advantage of SEM over TEM, is that the former does not require ultra-thin slice as a sample (see appendix of Chapter 5). However, TEM results in higher resolution micrographs, showing better the contrast between inorganic fillers and organic polymeric matrix in nanocomposites (Figure 2-4c). Nevertheless, TEM still lacks resolution for providing structural information from a single filler particle, especially in highly loaded nanocomposite samples due to imperfect contrast between matrix and filler. Because of these inherent limitations, the most accurate method to characterize aggregate size for nanocomposites is small angle X-ray scattering (SAXS).
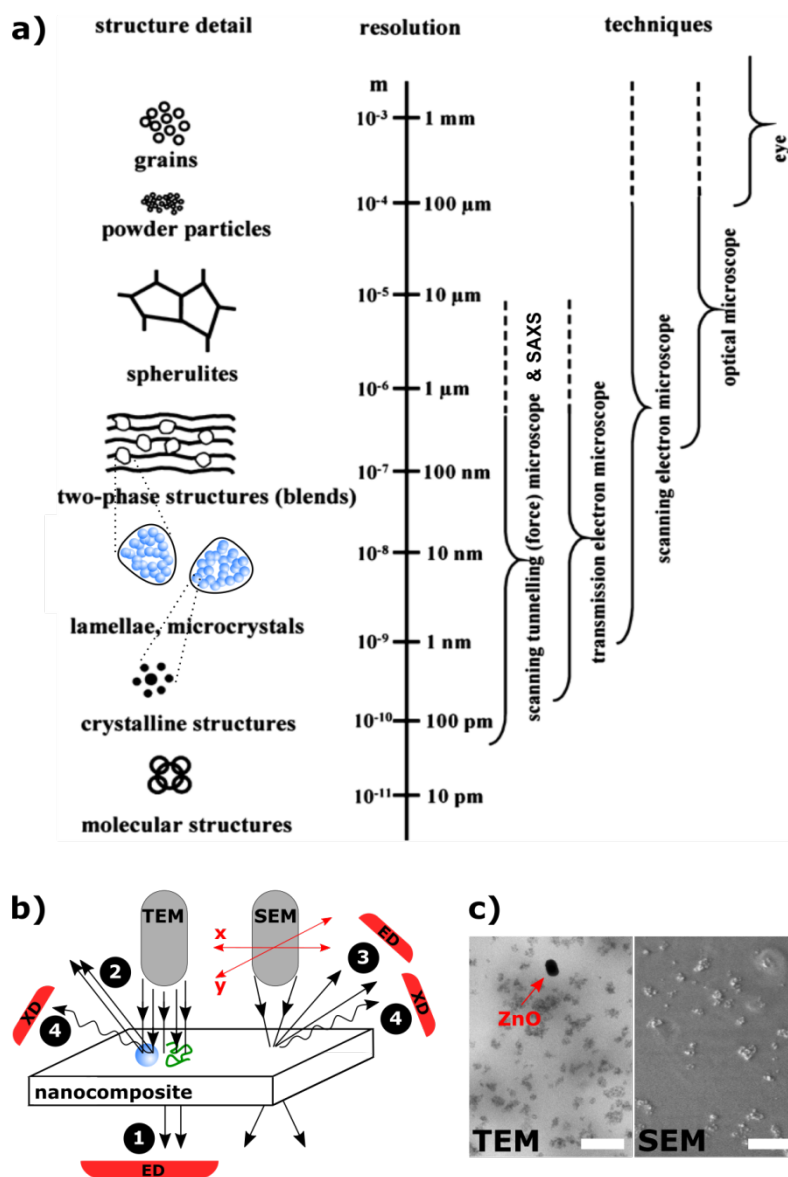
Figure 2-4. (a) Polymeric sub-structures of different sizes and resolution limits of different microscopic techniques and small angle X-ray scattering method (SAXS) for observing these sub structures. Image is adapted from [88]. (b) Illustration showing the principles of TEM and SEM. Positions of the electron (ED) and X-Ray (XD) detectors are shown as labelled red boxes on the way of corresponding electron paths. (c) TEM and SEM images of silica (1.59 vol %) / NBR nanocomposite taken at the same magnification. Scale bars are 500 nm.

Materials & Fundamentals of Methods

In a typical SAXS measurement, a rectangular cut of a nanocomposite sample (ca. 30 mm*8 mm, thickness of ca. 2mm) is illuminated by a collimated monochromatic X-ray beam with the wavelength of ~ 1.1 A (12.46 keV), and the intensity of the scattered X-rays is recorded by a 2-dimensional X-ray detector. The distance between sample and the 2D detector is often variable. Larger features scatter over smaller angles while smaller features scatter over larger angles. Since scattering from silica nanofillers is much stronger than those from rubber, the signal from the fillers is easily obtained. By applying the right model, which is critical, SAXS can give structure of silica distribution in our nanocomposites starting from a single particle.[38] The technical details of the SAXS measurements and the model applied for data interpretation can be found elsewhere.[38] SAXS measurements on the full nanocomposite systems studied in this thesis were done at the ERSF in Grenoble at the (ID 26) beam line by our collaborators in UvA (M.R.B. Mermet-Guyennet and J. de Castro). Using their data, and additional published data, we verified the robustness of our TEM based aggregate size determination explained below.

As a final word, it must be pointed out that the main purpose of electron microscopy in this work was to quantify the nanofiller distribution in polymeric matrix. The biggest motivation to use electron microscopy was because of experimental accessibility and flexibility. ID26 is a user facility where it is difficult to check many samples on-demand. Moreover, the presence of zinc oxide (ZnO) particles (dark black particle in the micrograph presented in Figure 2-4c) in our NBR nanocomposite formulations strongly disturbed the SAXS measurements. TEM provides the best combination of structural information of filler aggregate/agglomerates and elemental specificity (via EDX). Owing to the aforementioned challenges in TEM, we developed a robust image analysis protocol to quantify aggregate size in our composite samples.

Image analysis of TEM images for aggregate size determination

Aggregate size determination of nanocomposite systems was done by using an open-source image processing software called ImageJ®. The TEM imaging parameters and ImageJ software parameters used for image processing are indicated in the methods section of each following chapter. Herein, I will explain the physical meaning of the parameters used for the image processing. The basic process is to use thresholding as an image operation to separate the image into two phases: foreground and background. By choosing the proper thresholding

options in ImageJ®, we can set the aggregates of fillers as foreground and polymeric matrix as background. The steps for this process are stated below.

(i) All images were converted to 8-bit, grayscale images. In an 8-bit greyscale image, there are 256 (2^8) different intensity values which can be assigned to each pixel. Pixel with zero intensity looks black and white pixel has an intensity of 256.

(ii) In order to see the distribution of the intensities in the entire TEM image, we monitor the histogram of the image. The difference between the mean and standard deviation of the intensity histogram was used to obtain the critical threshold value. By calculating the critical thresholding value in this way, the threshold value was intrinsically consistent for all the analyzed TEM images, independent of changes in image contrast.

(iii) Apply threshold to the image.

(iv) Automated routines in ImageJ were used to analyze the resulting binary image for particles. We set the parameters to start counting from an area of a single particle to infinity. Since the shapes of the aggregates are completely random, we kept the circularity range between two maxima 0 and 1. 1 means a perfect circle. Each counted particle (aggregate) is numbered, and we could quickly scan the results and remove large, dark ZnO inclusions (see Figure 2-4c) from data set.

2.2.4   Surface-sensitive molecular spectroscopy

As mentioned before, many functions and applications in polymer-based nanocomposites are controlled by interfacial properties. Particularly, in order to explain the origin of filler dispersion and material property changes due to rubber functionality (F-SBR) in SBR nanocomposites, it was paramount to quantitatively analyze interfacial interactions e.g. between the silanol (Si-OH) functional groups of F-SBR on silica surface. Therefore, we used a mix of both ultrahigh vacuum (UHV) and *in situ* vibrational spectroscopy techniques. The two UHV surface sensitive emission spectroscopic methods used were *X-Ray photoelectron spectroscopy (XPS)* and *Near edge X-ray absorption fine structure spectroscopy (NEXAFS)*. We used surface sensitive scattering spectroscopy *Sum Frequency Generation Spectroscopy (SFG)* for *in situ* interfacial spectroscopy.

Materials & Fundamentals of Methods

X-Ray photoelectron spectroscopy (XPS)

XPS was used for determining the chemical composition of surfaces and can be classified as a surface sensitive since electrons cannot escape longer distances than a few Å.[89] During the XPS measurement, the sample is bombarded by incident X-Ray beam with a fixed energy (hv), and due to the photoelectric effect, electrons are emitted with a specific kinetic energy. The energy of the incoming photons must be high enough in order to overcome the binding energy (E_B) of the electrons and work function (Φ) of the measured material. In basic terms, the minimum energy required to remove one electron from the material is called work function of the material. In order to get an XPS signal, a potential barrier must be exceeded to remove an electron from its Fermi level to the vacuum level. When this electron leaves the material, it moves with a finite kinetic energy (E_K) and can be detected by an analyzer. E_K is expressed as:

$$E_K = hv - E_B - \Phi \qquad (2.5)$$

Importantly, XPS is intrinsically quantitative and provides results of elemental analysis in atomic percentages. The final electron photoemission (PE) spectrum comes from an intrinsic interaction. It is free of an extrinsic background, which originates from a photo excited electron due to the interaction with other electrons (inelastic scattering electrons or secondary electrons) during its travel to the surface and it has no effect on the intrinsic data (peak areas, peak positions and the peak widths) after proper subtraction. Because XPS is intrinsic, intensities from different core levels (of different atoms) can be used as a means to identify atoms and therefore calculate the atomic abundance (%) of particular atoms in a sample. In addition to its quantitative nature and chemical sensitivity at the surface, using Argon cluster sputtering, one can obtain chemical composition data from different sample depths in the system. This is essentially a layer-by-layer measurement, where one obtains a XPS spectrum and sputters with the Ar cluster in an alternating manner. Further measurement, instrumentation and data analysis details of the XPS performed for understanding the nature of F-SBR end functional group interaction on silica surface, will be discussed in Chapter 4.
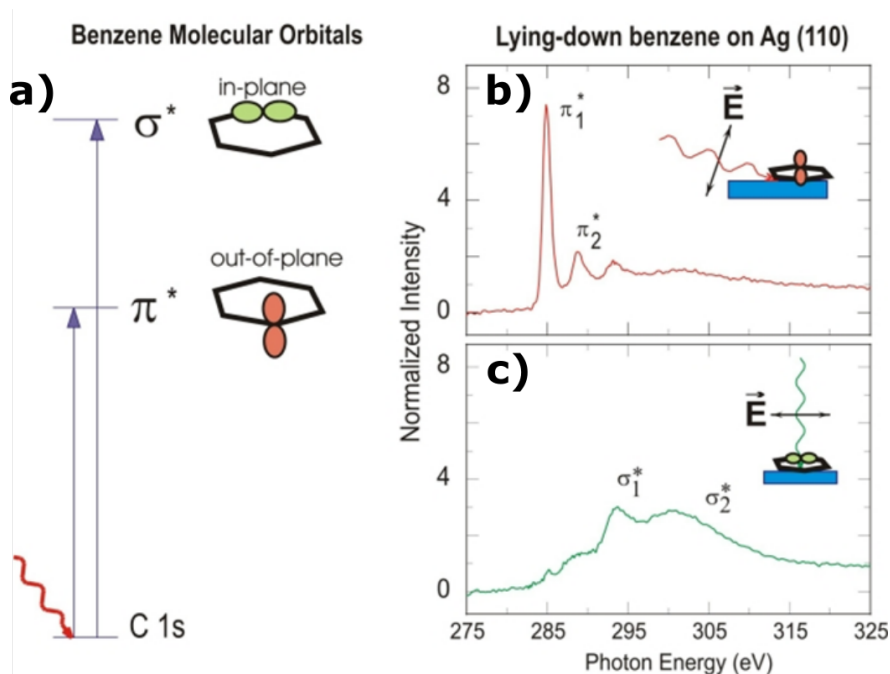
Figure 2-5. An example of polarization dependent NEXAFS spectra of benzene (C_6H_6) lying on Ag (110) surface. (a) unoccupied orbitals of σ and π symmetry aligned in and perpendicular (out-of-plane) to the ring plane, respectively, and the photon energies to excite these groups are illustrated. (b – c) Polarization dependence of the benzene groups on Ag surface are shown in two different NEXAFS spectra taken at different angle between surface normal and the incident polarized X-ray (polarization direction is shown by black line with arrows at both ends). Image is adapted from ref [52].

Near edge X-ray absorption fine structure spectroscopy (NEXAFS)

Differently from XPS, in NEXAFS the energy of the incident X-ray is not fixed. It is scanned, and the absorbed X-ray intensity, which is a consequence of excitation of an electron from a core orbital to an unoccupied molecular orbital is measured. Absorption-based NEXAFS requires thin samples (~ μm) because of the large absorption coefficients of X-rays in most materials, but it is not explicitly surface sensitive. As a result of X-ray absorption, decay of the core hole states results in emission of *Auger electrons* from valence molecular orbitals or so-called X-ray (*Auger*) *fluorescence*. Measuring the emission of electrons or fluorescence produces an Auger or electron yield NEXAFS spectrum.

Auger electron NEXAFS is surface sensitive mainly due to the low kinetic energy of electrons and their very short mean free path in a solid film, which is less

than 1 nm for the energy range from 250 eV to 600eV. Because the excitation X-ray is absorbed throughout a sample, Auger fluorescence, can emerge from deeper depths within the sample. The photons can arise from the top ca. 200 nm of the sample because the photons have significantly higher energy compared to the kinetic energy of electrons and they scatter less during their travel along the sample thickness (large mean free path).[90] Both Auger electrons and fluorescence provide us data for determining the photoabsorption of the film sample on a substrate from different depths.

Auger electron yielding of low Z elements (C, N, O etc.) are way stronger compared to their yield of fluorescence[52] and as mentioned before, Auger electron results are more surface sensitive compared to those from Auger fluorescence. Thus, in this thesis, we measure ordering of SBR films – which include aromatic groups – on silica surfaces by monitoring the so-called partial electron yield (PEY), which measures the Auger electrons.

NEXAFS measurements are useful for detecting the orientation of specific orbitals of carbon bonds (e.g., C-C in benzene rings (C_6H_6) in SBR). Particularly the transition matrix elements for instance π* orbital, have a polarization dependence with respect to the electric field vector (E) of the polarized incident X-Rays. A benzene molecule lying on Ag (110) surface is a popular example for showing the polarization dependence property of the NEXAFS (Figure 2-5).[52] Benzene includes unoccupied orbitals of σ and π symmetry and they are oriented parallel and perpendicular to the benzene ring plane, respectively (Figure 2-5a). A simple example of the power of NEXAFS was determining the orientation of benzene rings on the Ag surface. This was done by shining incident polarized X-Rays at the chemisorbed benzene on Ag (110) surface at two different angles. When the direction of E was parallel to the surface normal, peaks from the out-of-plane π orbitals became more dominant (Figure 2-5b). When the E was perpendicular to the surface normal, as shown in Figure 2-5c, in-plane σ orbital peaks became more intense. This experiment proves the benzene rings lies flat on the Ag (110) surface as it is shown in the insets of Figure 2-5(b) and (c). We performed similar experiments in order to monitor the ordering ability of the silanol end functional groups of F-SBR on silica surface, which will be discussed in details in Chapter 4.

Sum Frequency Generation Spectroscopy (SFG).
Sum Frequency Generation (SFG) spectroscopy, is a nonlinear optical spectroscopy that can provide surface specific vibrational spectra of sub-monolayer organization

of interfacial molecules.[91] Being a second order nonlinear process, the coherent SFG signal cannot be detected in centrosymmetric media. The macroscopic SFG polarization can be expressed as,

$$P^{(2)}(\omega_{SFG}) = \chi^{(2)}(\omega_{SFG})E_{VIS}(\omega_{VIS})E_{IR}(\omega_{IR}) \qquad (2.6)$$

Where $\chi^{(2)}$ represents the second-order nonlinear susceptibility of the material. E_{VIS} and E_{IR} are the electric field of incident visible and infrared beams, respectively.

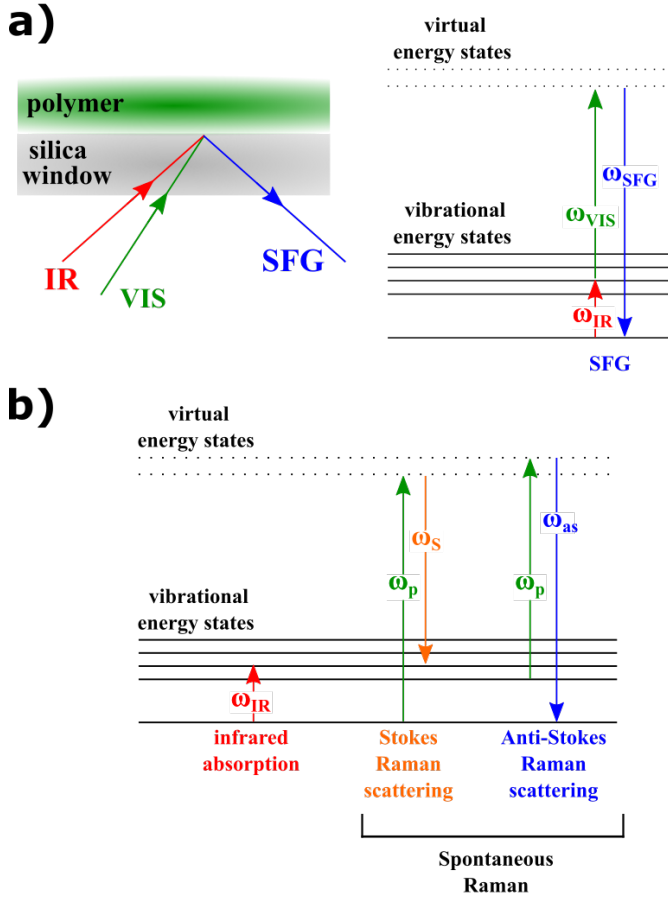**Figure 2-6.** (a) Schematic illustration of SFG measurement at sample – air interface and the general energy diagram of SFG. (b) Energy (photon) diagrams explaining IR, spontaneous Raman processes. In the both energy diagrams shown in (a) and (b), incoming photons leading to an excitation of matter are presented by upward arrows. Emitted photons as a result of relaxation of matter are presented by downward arrows.

Experimentally, SFG is performed by overlapping a broadband IR and narrowband visible beam in space and time at an interface, and consequently an SFG photon is eventually generated and its frequency is written as,

$$\omega_{SFG} = \omega_{IR} + \omega_{VIS} \tag{2.7}$$

While the broadband IR allows simultaneous detection of different IR modes, the narrowband visible beam provides spectral resolution down to 10cm^{-1}. The SFG signal is spectrally resolved and measured with a CCD camera. In our work, the SFG measurements were performed to obtain the interfacial signature of the SBR polymer at polymer – silica interface (Figure 2-6a). This was done to see quantify the effect of silanol end functional groups on F-SBR-filler interaction (Chapter 4).

2.2.5   Polymer anisotropy measurements

Polarized vibrational spectroscopy

Fourier Transform Infrared Spectroscopy (FT-IR)) and Polarized Raman spectroscopy are two popular techniques for measuring polymer chain anisotropy. Basic physics of these methods are illustrated in Figure 2-6b. When IR light (ω_{IR}) interacts with matter, the IR gets absorbed at certain frequencies if they match the energy gap between (or, are resonant with) the vibrational (real) energy states in a sample as shown in Figure 2-6b. In physical terms, these different vibrational states correspond to different molecular oscillations of bonded nuclei with, each having different transition dipole moments μ. The strength of the absorption is proportional magnitude of μ associated with a particular vibration.

In spontaneous Raman spectroscopy, matter interacts with visible light (ω_p). A large portion of the illuminating light reflects, elastically (Rayleigh) scatters and/or transmits, thereby not changing the frequency (energy) of the incident radiation. A (very) small fraction (~1 in 10^7) of the illuminating light changes its energy as a result of inelastic, or Raman, scattering (Figure 2-6b).[92] The energy change can be traced to a particular vibrational mode present in the matter. Unlike IR absorption, Raman scattering is proportional to the variation of polarizability, α, during interaction with the light. Raman scattering can result in two different outcomes,

$$\omega_{Raman} = \omega_P - \Delta\omega \text{ for Stokes Raman scattering}$$
$$or \tag{2.8}$$

$$\omega_{Raman} = \omega_P + \Delta\omega \text{ for anti-Stokes Raman scattering}$$

During Stokes Raman scattering, molecules or atoms are polarized by incident light energy and scatter photons having less energy than those of the illuminating light. In anti-Stokes scattering, the scattered light has more energy than the incident illuminating light because the atom or molecule was initially in a vibrationally excited state.

In our work, IR and polarized Raman spectroscopies are used for monitoring the alignment of rubber molecules in different nanocomposites under tensile stretching. Drawing the nanocomposite slices (ca. 20 μm thick) was done with a home-built stretching device including a motorized actuator (Thorlabs Z825B, New Jersey) which has a minimum achievable incremental movement of 50 nm. During our Raman measurements, in order to avoid complicated depolarization ratio calculations, we did not place any polarizer in front of the detector, and thus we could detect all the scattered Raman light. Therefore, below mentioned theory of dichroism for detecting polymer chain orientation could be applied both to the results from our FTIR and polarized Raman measurements.

Calculating polymer anisotropy

The measured sample has a coordinate system (w, u, v) as shown in Figure 2-7, where w, u, and v represents the stretching, transverse and thickness directions, respectively, and coincide with the laboratory coordinate axes directions. An IR or Raman absorption in (w, u, v) coordinate system (A_{uvw}) is calculated from the interaction between the incident electric field vector ($\vec{E}$) and the transition dipole moment of a particular molecular vibration vector ($\vec{M}$). A_{uvw} is expressed by an inner product of $\vec{E}$ and $\vec{M}$: $A \propto (\vec{M} \cdot \vec{E})^2$. [83]

In the simplest scenario, one assumes that the polymer chains are perfectly aligned parallel to the stretching direction, all the dipole moments of the absorbing groups in the polymer chain lie within a cone with a semi angle Ψ to the stretching (and chain axis) direction. In this scenario, the IR or Raman absorptions when the incident light is parallel ($A_\parallel$) and perpendicular ($A_\perp$) to the stretching direction of the sample are defined as,[83]

$$A_\parallel = A_{uvw}(90°, 0°) = \kappa \, \cos^2 \Psi$$
$$A_\perp = A_{uvw}(0°, 90°) = \frac{1}{2}\kappa \sin^2 \Psi$$

(2. 9)

where κ is a constant. The dichroic ratio R is a classical two-dimensional factor for defining the uniaxial orientation of the molecules to the axis of stretching. It is defined as $= \frac{A_w}{A_u} = \frac{A_{\parallel}}{A_{\perp}}$. The dichroic ratio, R_0 calculated from chains aligned perfectly along the stretching direction is then found as,

$$\mathbf{R_0 = 2 \cot^2 \Psi} \tag{2.10}$$
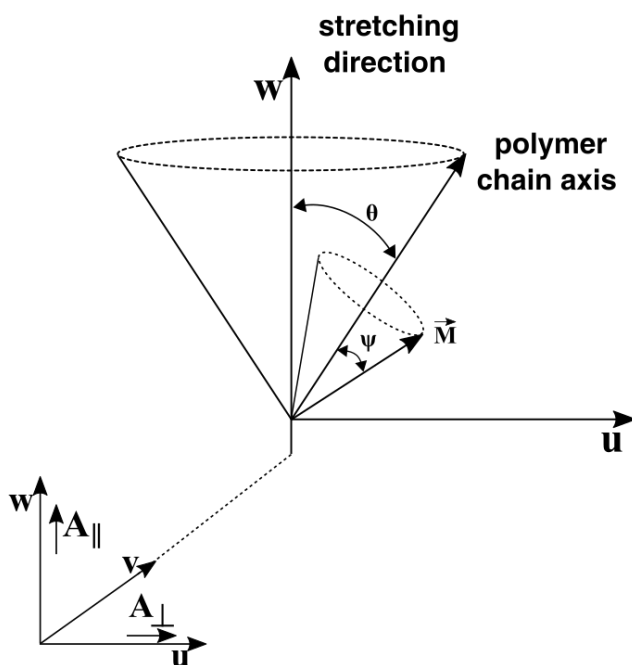
Figure 2-7. Transition moment distributions in an oriented polymer with respect to the stretching direction as a model which is used for our FTIR and Raman data interpretations.

In "real" conditions molecules will never be fully and perfectly aligned to the drawing direction. Therefore, a more realistic orientation of the chain molecules to the stretching direction is defined by a factor f, described by assuming a certain fraction, f of molecule (polymer) is uniaxially (perfectly) aligned and remaining fraction $(1 - f)$ is randomly distributed.[83] Therefore, dichroic ratio, R is expressed in terms of orientation fraction as,[93]

$$R = \frac{f\,\cos^2 \Psi + (1/3)(1-f)}{(1/2)f\,\sin^2 \Psi + (1/3)(1-f)} \tag{2. 11}$$

Eq. 2. 11 can be rewritten as eq. 2. 12 in order to find the orientation factor as a function of the dichroic ratio,

$$f = \frac{(R-1)(R_0+2)}{(R+2)(R_0-1)} \tag{2. 12}$$

where R represents the measured dichroic ratio of a molecular vibration in the "real" system and R_0 is expressed as in eq. 2. 10. In such "real" systems, it is also considered that polymer chains are on average separated from the stretching direction by a semi-angle ϑ as it is shown in Figure 2-7. Therefore, the dichroism, R (eq. 2.11), in this imperfect orientation is re-expressed by using the Ψ and ϑ together as,[93]

$$R = \frac{2\cot^2 \Psi \cos^2 \theta + \sin^2 \theta}{\cot^2 \Psi \sin^2 \theta + (1+\cos^2 \theta)/2} \tag{2. 13}$$

From eq. 2. 13, average orientation of the polymer with respect to the draw direction can be easily found if the angle between the dipole moment direction of the absorbed group and the polymer chain backbone (axis) is known. Furthermore, one can express the orientation function, f, more generally as shown below.[94–96]

$$f = \frac{(3 < \cos^2 \theta > -1)}{2} \tag{2. 14}$$

where $< \cos^2 \theta >$ is the orientational average of all groups calculated as shown below,[83]

$$< \cos^2 \theta > = \frac{\int_{\theta=0}^{\pi} F(\theta)\cos^2 \theta \sin \theta\, d\theta}{\int_{\theta=0}^{\pi} F(\theta) \sin \theta\, d\theta} \tag{2. 15}$$

In this equation, $F(\theta)$ is the probability distribution function for the reference axis and $F(\theta)\sin\theta$ is the overall probability that chains lie along the reference

direction. From the above equations we can observe that if the polymer groups align perfectly parallel to the reference axis (θ = 0°), $\langle S_{mol}(\cos\theta)\rangle$ = 1 and for perfectly perpendicular alignment (θ = 90º) $\langle S_{mol}(\cos\theta)\rangle$ = -1/2. For randomly oriented polymer chains, $<\cos^2\theta> = 1/3$ and thus f becomes vanishingly small. Then, for these systems the orientation factor equation (eq. 2. 12) can be rewritten as,

$$f = \frac{((2\cot^2\Psi) - 1)}{((2\cot^2\Psi) + 2)} \frac{(R - 1)}{(R + 2)}$$

(2. 16)

For the NBR and SBR molecules investigated in this thesis, the exact transition moment angle, Ψ, between their chain axes and the vibrational units used for quantifying alignment are unknown. Therefore, the orientation of the rubbers have been quantified without calculating R_0, which is assumed to be a fixed value for a particular molecular bonding geometry and is not changed with strain. Hence, the anisotropy of the rubbers at increasing strain level are found by calculating the dichroic function, S_{mol}, using the experimental absorption data observed when the incident light is parallel ($A_\parallel$) and perpendicular ($A_\perp$) to the stretching direction as shown below,

$$S_{mol} = \frac{R - 1}{R + 2} = \frac{A_\parallel - A_\perp}{2A_\parallel + A_\perp}$$

(2. 17)

S_{mol} can be conceptually interpreted as the orientational distribution (f) scaled by the (constant) dichroic function between the vibrational mode and the chain axis, $S_{mol,0}$, established by the chemical bonding.

2.3   Statistics

In the course of my doctoral work, suitable methods to validate the statistical significance of the measured data were necessary to quantify the accuracy and repeatability of my results. In particular, I have used different statistical approaches to test my hypotheses: t-tests (a test statistic that follows a Student t-distribution under the null hypotheses) and analysis of variance, known as ANOVA.

While a t-test can be used to determine the statistical difference between two data sets (with a certain level of significance), the ANOVA analysis extends

such an approach to many groups. The biggest drawback of the t-test is its inability to test the significance of more than two different groups at the same time. Thus, I used ANOVA for analyzing the variance among and within groups when there are more than two. Different types of ANOVA analyses exist, however we used only "one-way ANOVA" test which compares more than two populations by changing only one factor at a time (e.g. aggregate size of different silica / NBR nanocomposites at the same volume fraction). We performed all the ANOVA analyses using software called IgorPro (Wavemetrics, Portland). In general, during an ANOVA test, we first set up the null hypothesis, assuming there is no significant difference between the groups, and an alternative hypothesis, which assumes that there is a significant difference between the groups. To this direction, we used F-test in order to assess whether the expected values of a quantitative variable among several populations are statistically different from each other. ANOVA first calculates the F-ratio. F-ratio quantifies the variance *between* different populations in a group with respect to the variance *within* each population as,

$$F - \text{ratio} = \frac{\text{variance between the sample means}}{\text{variance within the samples}} \qquad (2.18)$$

Details of the algorithm for calculating the between group variance and within group variance can be found in ref [97]. The typical F distribution used in an F-test is shown in Figure 2-8, from which one can determine if there is a significant difference between one or more populations. Generally speaking, if the null hypothesis is true, the within population variance is comparable to the between population variance, or in other terms, $F \sim 1$. When the variability between population means becomes significantly larger than the variability within the populations, the F-ratio gets bigger. As shown in Figure 2-8, significant differences between the means in the group of samples during an ANOVA test is observed (rejection of the null hypothesis) if the F-ratio gets very high and exceeds the critical value which is corresponding to $p < 0.05$ in this thesis. [97]

After knowing whether one or more group(s) are significantly different when compared to all groups, ANOVA helps us in a second step to identify exactly in which group(s) we observed this significant difference. To this direction, ANOVA includes some further tests, which are called *post-hoc tests*. In these tests, ANOVA mainly runs pairwise difference tests between pairs in the population and reports those pair(s) for which there are significant differences.
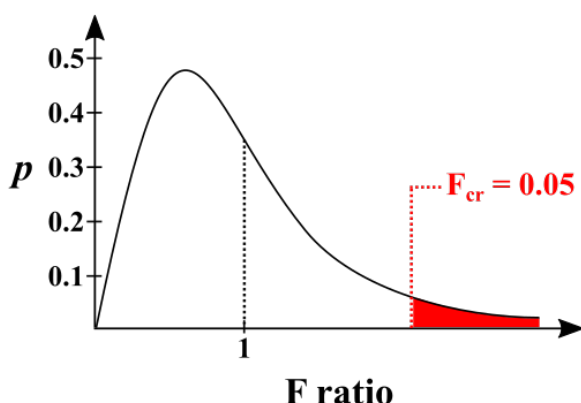
Figure 2-8. Example F distribution used for testing the null hypothesis in our ANOVA analysis showing the critical F-ratio at 5% (0.05).

This might prompt one to ask: why we do not just use multiple t-tests instead of using complicated ANOVA method with post-hoc test(s)? In multiple t-tests (comparing more than two groups together only as isolated pairs), the probability of making a Type I error (an error of rejecting a true null hypothesis) increases with increasing number of t-test. [98] Thus, after multiple t-tests in a population with more than two groups, the outcome is much more likely to show significant differences between certain pairs, even though no real (significant) difference exists.[99] The post-hoc tests are able to keep significance level (p) stable regardless of the number of groups being compared. Based on the particular research question, post-hoc tests give us different methods for group comparisons. For instance, with the help of post-hoc tests, we can compare one particular group against a combination of all remaining groups in a population, or against only some of the chosen control groups.

There are different kinds of post-hoc tests and along the thesis, we used Tukey and the Newman-Keuls tests as the two most common methods of post-hoc tests.[100] In this thesis, significant difference among certain group(s) is/are only accepted after observing the significant difference of the same pair(s) from the results of both Tukey *and* the Newman-Keuls tests. Using more than one pairwise comparison helps us to identify whether a statistical difference between certain group(s) is connected to the sampling error (size of the groups) or not.

CHAPTER 3: REINFORCEMENT OF SILICA NANOCOMPOSITES

3.1 Abstract

Particulate fillers are often used to enhance the properties of soft materials; polymer composites often contain nanometer-sized particles to improve reinforcement, for example. The rationale for using nanometer-sized particles remains unclear, however, and classical micromechanical models cannot account for a scale dependent reinforcement. The systems studied here reveal that the reinforcement increases with decreasing filler size. A new relation is proposed, based only on the particle size, volume fraction, and relative moduli of filler and matrix that describes the experimental results for reinforcement of both filled rubbers and a model system.

3.2 Introduction

Soft materials are often made up of particles dispersed in a continuous matrix, where the concentration and size of the filler particles has a profound effect on the physical properties. The addition of filler particles such as carbon black or silica to a polymer matrix, for example, changes the linear and non-linear mechanical behavior of the resulting composite material.[59,101] For filled rubbers, the linear shear modulus of the filled material increases by more than an order of magnitude over that of the bare rubber. This stiffening, called reinforcement, is defined as the normalized change in shear modulus at volume fraction ϕ of fillers compared to that of the unfilled polymer: $R(\varphi) = G(\varphi)/G(\varphi = 0) - 1$, with G the linear shear modulus. Numerous micromechanical models exist for composite materials that predict $R(\varphi)$ on the basis of the mechanical properties of the constituent materials and their respective volume fractions.[102–104] Such models are based on classical elasticity theory, however, which is size-independent, so that they cannot account for a dependence of composite mechanical properties on the size of the fillers. This strongly contradicts the generic observation that nanoparticles with a high surface-to-volume ratio provide the highest reinforcement.[62,105–107] One recent study demonstrated and explained a size dependent deformability of liquid inclusions in soft matrices using a modification of Eshelby's theory, but no such explanation exists for size-dependent elasticity of systems with hard inclusions in a polymer matrix. [108] In this work, the effect of rigid filler size on reinforcement of polymer

composites in industrial composite materials and a model system is investigated systematically.

3.3   Materials & methods

Filled rubbers

In total, five different types of filled rubbers were used. Two of them, are Styrene Butadiene Rubber (SBR, ρ=140 kDa, vulcanized) based nanocomposites with different rubber functionality (see section 2.1 in Chapter 2) filled with precipitated silica nano-particles. The three other filled rubbers are Acrylonitrile Butadiene Rubber (NBR; ρ =250 kDa, vulcanized), loaded with silica particles of different specific surface areas. Further details of these materials can be found section 2.1 in Chapter 2.

Model system

Polyvinyl Alcohol (PVA, hydrolyzed at 99-100% and a molecular weight of 86 kDa) is provided as a powder by Acros Organics. The powder is dissolved (4 wt %) in distilled water by mixing with a stirring bar at 95 °C for 3 hours. The borate is obtained by dissolving sodium tetra borate (Sigma Aldrich) in distilled water (4 wt %). For some measurements the mass fraction of 4 wt % was decreased in order to decrease the shear modulus of the matrix of the model system (Figure 3-7b). The gel is finally formed by mixing 2 g of solution of borate with 8 g of solution of PVA. The polystyrene beads are Dynoseed ® TS 500, TS 250, TS 140, TS 80 and TS 40 with radii of 250, 125, 70, 40 and 20 μm, respectively.

Rheological measurements

Oscillatory measurements were carried out with an Anton Paar Physica MCR 300 rheometer mounted with the parallel plate geometry. For measuring the filled rubbers the diameter of the geometry was 5 mm. Samples were cut in shape of disks with a thickness about 2.5mm. Loctite glue was used at sample and parallel plates in order to avoid wall slip during the measurements.[109] For the experiments with the model system the geometry was the same but with a diameter of 25 mm, and both of the surfaces were rough to avoid also any wall slip. Data were obtained in the linear regime. We measure here the complex modulus G*, which is found to be frequency independent and, because G' >> G", is equated to the shear modulus at low strain amplitude.[110]

Transmission Electron Microscopy and elemental mapping of silica aggregates

Nanocomposites were imaged with transmission electron microscopy (TEM) and analyzed to determine the silica aggregate size. The nanocompounds were sectioned to a thickness of around 50 nm with an ultracryotome at −60°C using a diamond knife. TEM images were taken by operating a JEOL JEM 1400 microscope with an accelerating voltage of 120kV, which was maintained constant for all samples. To obtain sufficient statistics for aggregate size analysis, a large number of aggregates (~ 4000 aggregates per sample) were taken from different locations within each ultrathin cryosection. All the micrographs were taken with constant electron beam intensity and at an optimum magnification of 5000X.
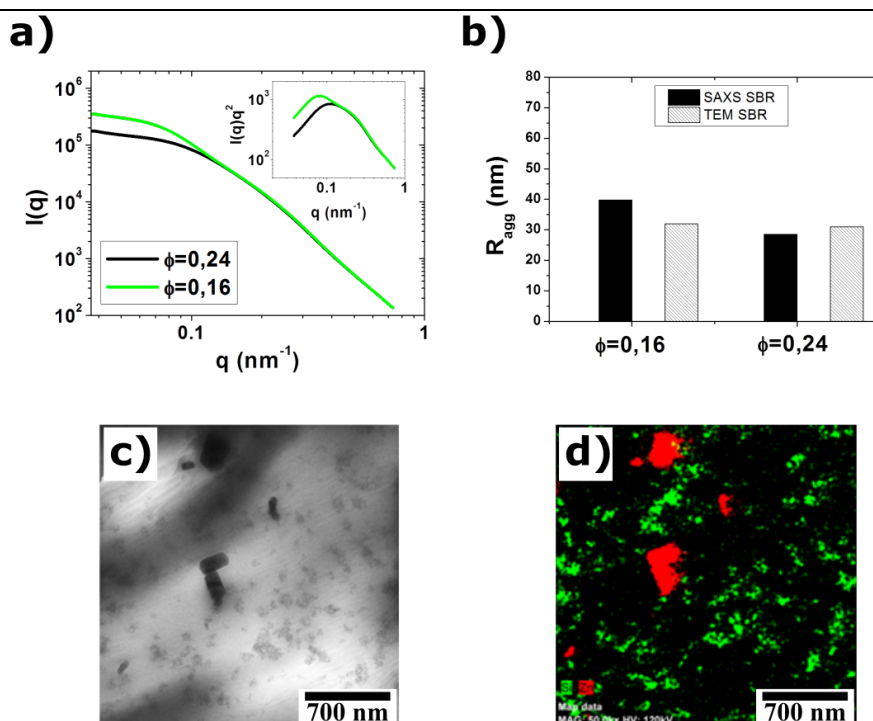
Figure 3-1. (a) SAXS spectra I(q) for the SBR samples (ϕ=0.16 and 0.24). The inset shows the Kratky representation of these same spectra. The aggregate size (r_{agg}) is found at the abscissa corresponding to the maximum of the curve. (b) r_{agg} results from Small-Angle X-Ray scattering (SAXS) analysis of silica/SBR samples loaded with 16 % vol. and 24 % vol. of silica fillers shown (filled columns) with the r_{agg} results from TEM image analysis (patterned columns). (c) TEM image of silica (1.6 vol %) /NBR nanocomposite including of 15 nm diameter silica nanofillers (specific surface area: 175m^2/g) and (d) elemental mapping image of the same region showing Si and Zn in green and red color, respectively.

Microstructural analysis of silica aggregates

In this work, silica microstructure is given by the mean aggregate size (r_{agg}) at different volume fractions. A thresholding routine is used to highlight aggregates against the rubber background in the TEM images and obtain particle analysis for calculating aggregate area and size (see 2.3 in Chapter 2). In order to compare the microstructural differences across composite samples the same thresholding parameters were kept constant. The output of the image analysis includes projected area (A), perimeter, and locational information of each aggregate identified in the image. The projected areas for all aggregates taken from a particular sample were pooled and averaged to calculate the average aggregate radius (r_{agg}).

3.3.1   Aggregate size measurement

TEM comparison with SAXS measurement

As a benchmark for the analysis aggregate size measurements from TEM are compared with those derived from Small-angle X-ray scattering SAXS (Beam line ID26 (ESRF Grenoble), wavelength 12.4 keV and distance between sample and detector is 7m., more information about the derivation can be found in ref [38]) for two types of SiO_2/SBR samples with different filler concentration (Figure 3-1). The agreement between values from TEM and SAXS for these samples demonstrates that the quantitative aggregate analysis is robust. Finally, the presence of strongly scattering ZnO particles (which have a size in the range of the aggregates) contribute to the SAXS spectra for NBR composites, so it was not possible to arrive at any meaningful aggregate size from these data. Therefore, TEM, coupled to energy dispersive X-ray (EDX) analysis, was necessary to segregate ZnO particles and only analyze sizes of silica aggregates (Figure 3-1(c) and (d)).

Polydispersity of the aggregates and aggregate size-volume fraction relation

The fillers in the real rubbers were found to be highly polydisperse (Figure 3-2a), with an average aggregate radius, r_{agg}, of ~ 40-100 nm, depending on the size of primary silica used. The radius of the aggregates is found to be independent of the volume fraction of silica (Figure 3-6b of the main text). As previously mentioned (see 2.1 in Chapter 2), all the filled rubber samples used in this article are provided by industrial partners who prepare these samples in internal mixers. The effect of

this mixing process on aggregates is not clear and is beyond the scope of this article. Nevertheless it is possible to provide initial insights regarding the silica aggregation during mixing.
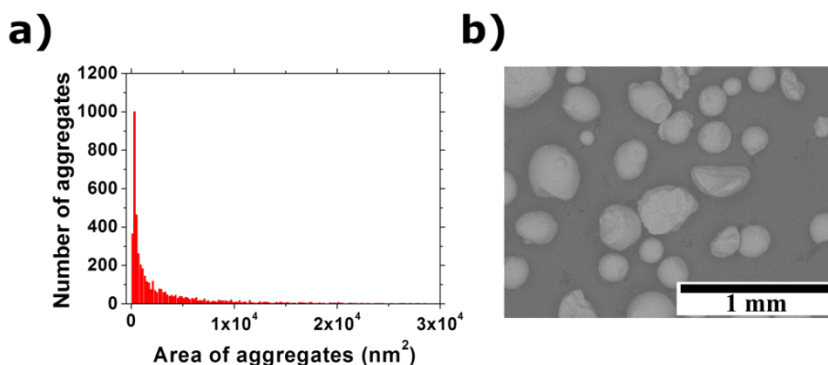
Figure 3-2. (a) Histogram showing the aggregate area distribution of silica (0.016 % vol.) / NBR nanocomposite. (b) SEM picture of aggregates (Zeosil 1165 MP) as provided by the manufacturer, prior to mixing.

The size of the silica added to the polymer is typically of the order of 100 µm, which is 1000 times larger than the final aggregates or the primary particles as quoted by the manufacturer (Figure 3-2b). Others have shown that these large silica particulates are broken down during mixing and potentially grow again via re-agglomeration.[111] This phenomenon was addressed in a recent study of the parameters influencing the structure of the filled material during mixing.[111] In that study it was shown that the radius of the aggregates increases with volume fraction if the parameters of mixing are kept constant, but that an increase of the power of mixing on the other hand decreases the radius of the aggregates. In the present work there is a constant radius of the aggregates that is independent of the volume fraction. The previous study indicates that this result follows from a rather complicated process. However, a constant size (i.e. independent of φ) has been observed in other filled rubbers.[38]

3.4 Results and discussion

Monodisperse polystyrene microspheres, which do not aggregate, are used in the model system (see section 3.3). For the industrial compounds, the primary

nanoparticles aggregate into clusters, and their average aggregate size (r_{agg}) is measured using TEM. Several of the fillers contain zinc oxide, which precludes SAXS measurements. TEM sizing was validated against SAXS in the industrial rubbers where no zinc oxide was present (Figure 3-1b). A scaling for $R(\varphi)$ is obtained that describes the size dependence of the reinforcement for all studied systems. The scaling incorporates an explicit dependence on the size of the filler or filler aggregate and the mechanical contrast between the filler and the matrix material. This scaling captures the filler-size-dependent reinforcement of composite materials and provides the underlying rationale for the use of nanosized filler particles in such materials. The first industrial composite is an acrylonitrile butadiene rubber (NBR) matrix filled with 15, 20, and 28 nm primary size silica particles. The chemistry is varied by using an additional industrial composite consisting of a styrene butadiene rubber (SBR) matrix filled with silica particles. The model system consists of a polymer gel, polyvinyl alcohol (PVA) crosslinked with Borax,[112] reinforced with polystyrene beads of radii (r_b) ranging from 20 to 250 µm.
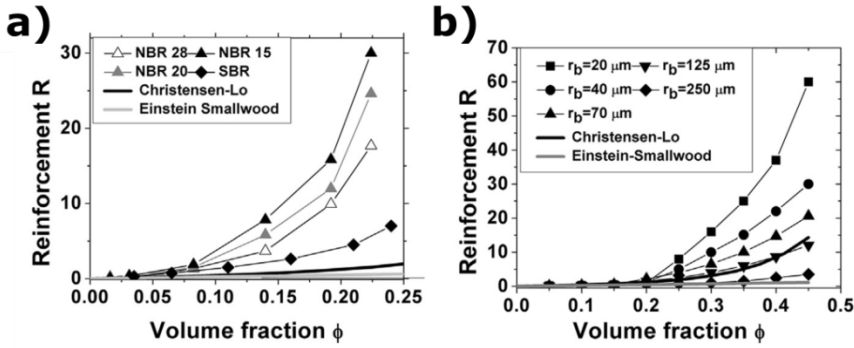
Figure 3-3. Reinforcement (R) versus volume fraction for (a) the industrial rubbers (SBR and NBR) with fillers of varying sizes and (b) the model system (PVA gel filled with polystyrene beads of radius (r_b)). The grey and black lines correspond to the Einstein-Smallwood Equation (ESE) and the Christensen-Lo model, respectively. Additional information about the Christensen-Lo model can be found in the Appendix I. The mechanical contrast between the moduli of the fillers and the matrix is ~ 10^6 for the model system (PVA gel: G ~ 10^3 Pa; polystyrene: G ~ 10^9 Pa) and ~ 10^3 for the filled rubbers (SBR and NBR rubber: G ~ 10^6 Pa; silica: G ~ 10^9 Pa)

The reinforcement measurement shows that for the industrial rubbers $R(\varphi)$ at any fixed value of φ is largest for the samples with the smallest silica

primary particle (Figure 3-3a). The model system, despite its simple microstructure, qualitatively exhibits the same mechanical behavior as the industrial rubbers (Figure 3-3b): a larger reinforcement is observed for smaller particles. Classical elasticity theory on the other hand supposes that (i) the filler size is irrelevant and (ii) the reinforcement is a function of φ only. In both systems, the Einstein-Smallwood Equation (ESE, $R = 2.5\varphi$) no longer describes the reinforcement when φ is greater than 0.15, as filler size clearly begins to play a role. An alternative model for reinforcement is the Christensen-Lo model, which uses a mean field approximation (a filler particle surrounded by a polymer layer embedded in the bulk composite material[103,113] - see Appendix I). This model clearly underestimates the reinforcement (Figure 3-3), though it can be forced to fit the reinforcement-volume fraction curve for a single filler type (size) by incorporating an effective volume fraction (the volume fraction times a proportionality factor), which is attributed to the fractal nature of the aggregates of the silica nanoparticles.[58,113,114] Even with this parameter, however, the filler-size-dependent elasticity cannot be captured. Hence, the challenge is to develop a composite elasticity theory that accounts not only for filler volume fraction φ but also for filler size $r_{b,agg}$ in describing the reinforcement of a composite material.
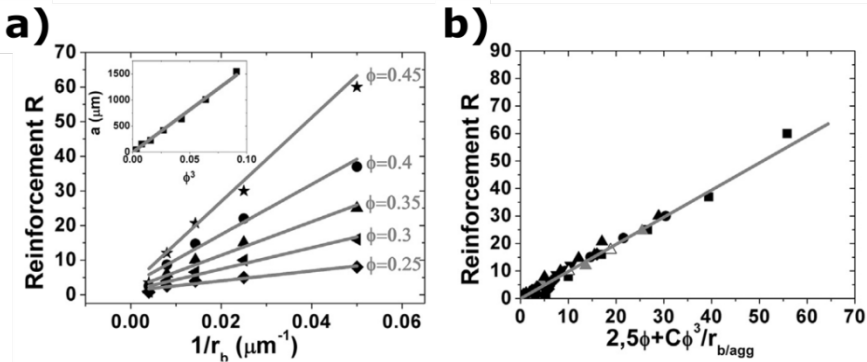
Figure 3-4. Filler-size dependence of the reinforcement of the model system: (a) reinforcement versus the inverse of the radius of the beads for different volume fractions. The red lines are linear fits with slope a. Inset: Slopes a as a function of φ^3. Here, another linear dependence is apparent so the data can be described by $R = 2.5\varphi + C\varphi^3/r_b$ (b) Reinforcement versus the rescaling parameter derived in Figure 3-4(a) for both the model system and the filled rubbers (aggregate size measurement for filled rubbers in Figure 3-6; $r_{b,agg}$ is the radius of beads or aggregates depending on the system considered). The reinforcement data used are the same as in Figure 3-3. The line has unity slope. The values found for C are 73 and 20 microns for NBR and SBR respectively

and 12 mm for the model system (see Appendix I). Note that r_{agg} is independent of φ for NBR rubbers (Figure 3-6(b)).

To further explore the filler-size-dependent reinforcement, it is plotted as a function of $1/r_b$ at constant φ for the model system, for which the particle size is well-defined. It is evident that reinforcement increases linearly with the inverse radius of the filler particles (Figure 3-4a). The lines in Figure 3-4a are of the form $R = 2.5\varphi + a/r_b$, which is the ESE reinforcement plus a size-dependent factor a/r_b ,with a varying as φ^3 (Figure 3-4a inset). After characterization of the aggregate size in filled rubbers from TEM imaging (Figure 3-6 and section 3.3.1) a similar correction for the reinforcement is obtained of the form $R = 2.5\varphi + b/r_{agg}$ and a similar analysis shows that b correspondingly varies as φ^3. By plotting the reinforcement data for all systems on the same graph, Figure 3-4b shows that the same reinforcement relation $R = 2.5\varphi + C\varphi^3/r_{b,agg}$ accurately describes the size-dependent-reinforcement for the model and industrial systems, where C is a constant with dimensions of length. This correction can then be viewed as the expected φ^2 correction to the ESE relation multiplied by the specific surface area S (surface area per unit volume) of the filler, $S = 3\varphi/r_{b,agg}$, yielding $R \sim \varphi^2 S$.

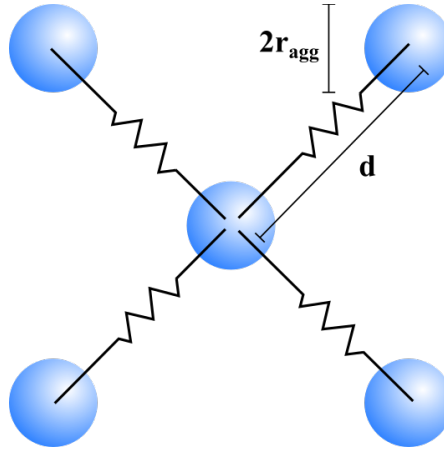**Figure 3-5.** Illustration of different elements model used for finding φ^3/r. Blue balls represent the aggregates and they are linked with elastic springs.

A similar modulus scaling with roughly φ^3 has been observed for percolated networks;[115,116] however, TEM images suggest that the systems studied here are not percolated (Figure 3-6a). Furthermore, recent work from Chen

et al. [117] showed that the systems considered in the present work do not percolate below $\varphi = 0.35$. Therefore, a starting point for developing a length-scale dependent elasticity for reinforcement may be obtained from the following considerations: (i) in the ESE model, the $2.5\,\varphi$ term arises from hydrodynamic effects;[118] (ii) the first interaction term is expected to scale as φ^2 (for pairwise interactions), as in the Guth-Gold-Einstein relation ($R = 2.5\varphi + 14.1\varphi^2$). The size dependence must therefore enter through the mechanism of interaction. If one imagines a set of spring-like forces (transmitted via the polymer network) between neighboring aggregates whose number is determined by the available surface area, the first-order representation of such a spring-like contribution to the elastic response would scale as the surface-to-volume ratio, which is $\varphi/r_{b,agg}$ in correspondence with the observed $\varphi^3/r_{b,agg}$ dependence.
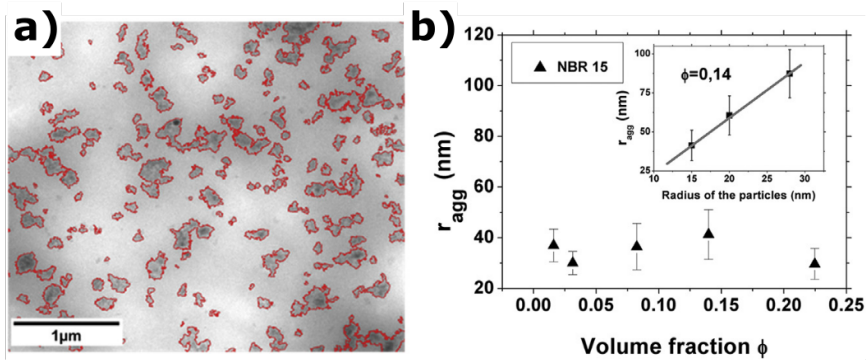
Figure 3-6. Microscopic characterization of the silica aggregates in industrial NBR composites: (a) TEM image analysis from a 50 nm thick slice showing aggregate regions distinguished from NBR matrix (red color borders). The number and coverage area of the aggregates (N_{agg} and A respectively) is obtained from these pictures. Assuming circular shapes, the radius of the aggregates r_{agg} are defined by $r_{agg} = (A/\pi N_{agg})^{1/2}$. (b) Measurement of the radii of the aggregates (r_{agg}) as a function of volume fraction. The aggregate size does not depend on φ. The inset shows the radius of the aggregates as a function of the radius of the primary particles at $\varphi = 0.14$. Error bars are standard errors of the mean from N > 4000 aggregates. (For interpretation of the references to color in this figure legend, the reader is referred to the web version of this article.)

One way of understanding the φ^3 term microscopically is to realize that upon increasing φ, the radial distribution function g(x) develops a peak that corresponds to the average distance between nearest neighbours, implying also an effective

potential of the mean force between two particles, $(V_{eff}(x_{min}))/kT = -\log[g(x_{\max})]$ [119] (which is valid if the matrix elasticity is affected by the silica aggregates as shown in Ref. [10]); $V_{eff}(x)$ takes into account all many-body effects mediated by the polymer chains, including bridging, in a mean-field manner. This allows one to define a spring constant $\kappa = ((d^2 V_{eff})/(dx^2))_{rmin}$ parameterizing the interaction strength between neighboring particles, every bond being a spring of length, $d = 2r_{b,agg} + x$, where $r_{b,agg}$ is the particle size and x is the separation between two particles (Figure 3-5). The overall elastic modulus of such an assembly of interacting particles can be evaluated considering the energy necessary to macroscopically deform the material by a strain (γ), implying that each spring is stretched by a relative amount $\approx d\gamma$. If the springs can be considered to be independent (which is a rough assumption, but it is very difficult to do better at the level of simple scaling arguments), the total elastic energy is given by total number of springs $n_b N/2$ multiplied by the energy of each spring, where n_b is the number of nearest neighbors per particle and N the total number of particles. The total elastic energy density (per volume V) can be derived as $\approx \kappa n_b (N/V)(d\gamma)^2$ and the shear modulus can be calculated as the second derivative of energy density with respect to γ as $G \approx \kappa n_b (\varphi/r_{b,agg}^3)d^2$, where $N r_{b,agg}^3/V \approx \varphi N$ is used. If the neighbors are not too far from each other, $d \approx 2r_{b,agg}$, leading to $G \approx \kappa n_b (\varphi/r_{b,agg})$. This recovers the proportionality to S, the specific surface area of particles per unit volume. Further, the number of neighbours (n_b) can be estimated from the integral of the peak of the radial distribution function Ref. [120]; for not-too-dense systems, $g(x_{max}) \approx 1 + b\varphi$ (a Taylor expansion about infinite dilution), where b is a coefficient that depends on the interaction (e.g. $b \approx 3$ for hard spheres).[121] It then follows that the first non-linear term in volume fraction is $n_b \approx \varphi^2$. Combining these relationships leads to $G \approx \kappa n_b (\varphi/r_{b,agg}) \approx \varphi^3/r_{b,agg}$, which is the scaling derived from the experimental measurements.

Whether arriving at $R \sim \varphi^3$ scaling via the microscopic derivation or intuitive expansion of ESE for non-interacting particles with a particle-interaction term, both lead to the relation, $R = 2.5\varphi + C\varphi^3/r_{b,agg}$. The reinforcement at high volume fraction can be physically understood as a coupling between volume and surface effects, which explains the filler-size-dependent reinforcement in this regime, and the magnitude of C is the upper limit for separation between aggregates within the polymer matrix.
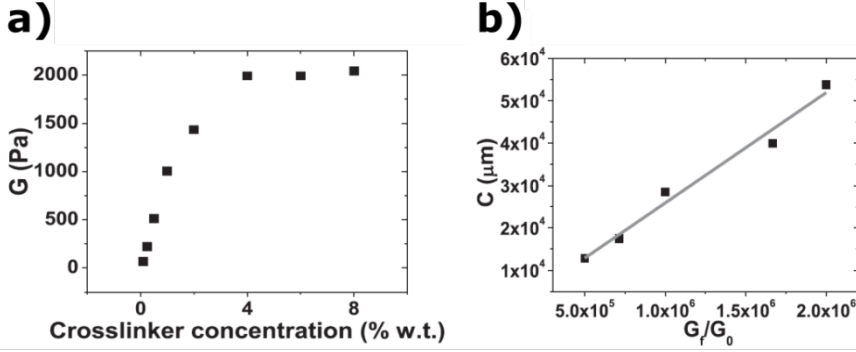
Figure 3-7. Dependence of C on the mechanical contrast between filler and matrix: (a) Linear shear modulus of the PVA gel with different concentrations of crosslinker (Borax). (b) Evolution of C with the moduli contrast between fillers and matrix. The grey line shows the fit with slope d δ = 25 nm.

In the rescaling presented here, C is the only unknown parameter. It is a proportionality constant with units of length that depends on the type of system. The reinforcement of any filler/matrix system is expected to scale with the ratio of the modulus of the filler to that of matrix, because a soft filler does not reinforce a composite to the same extent as a hard filler at the same volume fraction, and the reinforcement should go to zero when the moduli of filler and matrix are equal. Therefore, the value of C should scale with the ratio G_f/G_0, with G_f the modulus of the bulk filler material (e.g. silica or polystyrene) and G_0 is the modulus of the unfilled matrix. This is indeed observed when the crosslinking in the model system is tuned (see Figure 3-7a) to modify G_0. Consequently $R = 2.5\varphi + \delta\left(\frac{G_f}{G_0}\right)\varphi^3/r_{b,agg}$ with δ = 25 nm for all systems studied (Figure 3-7b), where $C = \delta(G_f/G_0)$. C then defines a physical length scale that can be interpreted as the maximum spacing between aggregates for which the φ^3 term will contribute to reinforcement of the composite material (Appendix I). One can calculate a required filler (or aggregate) "density" as 1/C, which decreases as the mechanical contrast between the filler material and matrix increases, with the maximal filler density equal to 1/25 nm when the modulus contrast is unity.

3.5   Conclusions

In this article the filler size-dependent reinforcement was studied for industrial rubbers as well as for simplified model system with well-defined beads as fillers. While it is a common, yet puzzling, observation that smaller filler particles are better reinforcing agents,[62,107] this effect has been quantified here and a scaling law for the filler-size dependence of the reinforcement of composites was derived. This scaling law is a first, but critical, step to developing new theories for predicting reinforcement of composites materials. It is sufficient to account for the filler-size dependent reinforcement phenomenon; no other terms in an expansion in volume fraction are needed for the (rather large) volume fraction range studied here. In addition, only a single parameter C, which is proportional to the filler to matrix modulus ratio, is necessary to rescale all data for a given combination of filler and matrix materials once the filler (or aggregate) size is known. Finally, it is worthwhile to mention that a variety of systems and chemistries were studied in this work, strongly suggesting that the rescaling presented here is universal and reveals a fundamental insight as to why small fillers are commonly and efficiently used to achieve maximal reinforcement in composite polymer materials.

3.6 Appendix I

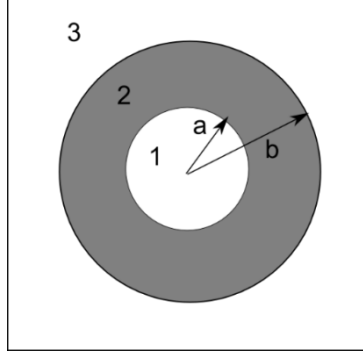### 3.6.1 The Christensen Lo Model

Figure 3-8. Different material parts considered by the Christensen Lo model: Support for explanation of the model. (1) the filler, (2) the polymer and (3) the equivalent medium including polymer and matrix (modulus of the overall material).

The Christensen-Lo model is based on the equivalent medium theory. This technique considers a single filler (1), a pure polymer layer surrounding it (2), and an effective medium around the polymer layer (3). This effective medium includes the combined effect of all the other fillers embedded in the polymer matrix. The modulus of this medium is the modulus of the overall material. Continuity of the displacement and the stress at the filler/polymer and polymer/equivalent medium (r=a and r=b, respectively) interfaces is assumed. This yields a second order equation for the reinforcement [103,122]:

$$
\begin{cases}
A\left(\varphi, v_f, v_0, \frac{G_f}{G_0}\right)(R+1)^2 + 2B\left(\varphi, v_f, v_0, \frac{G_f}{G_0}\right)(R+1) + C\left(\varphi, v_f, v_0, \frac{G_f}{G_0}\right) = 0 \\[2mm]
\begin{aligned}
A = {} & 8\left(\frac{G_f}{G_0}-1\right)(4-5v_0)\eta_1\varphi^{\frac{10}{3}} - 2\left(63\left(\frac{G_f}{G_0}-1\right)\eta_2 + 2\eta_1\eta_3\right)\varphi^{\frac{7}{3}} + 252\left(\frac{G_f}{G_0}-1\right)\eta_2\varphi^{\frac{5}{3}} - 50\left(\frac{G_f}{G_0}-1\right)(7-12v_0+8v_0^2)\eta_2\varphi \\
& + 4(7-10v_0)\eta_2\eta_3
\end{aligned} \\[2mm]
\begin{aligned}
B = {} & -2\left(\frac{G_f}{G_0}-1\right)(1-5v_0)\eta_1\varphi^{\frac{10}{3}} + 2\left(63\left(\frac{G_f}{G_0}-1\right)\eta_2 + 2\eta_1\eta_3\right)\varphi^{\frac{7}{3}} - 252\left(\frac{G_f}{G_0}-1\right)\eta_2\varphi^{\frac{5}{3}} + 75\left(\frac{G_f}{G_0}-1\right)(3-v_0)v_0\eta_2\varphi \\
& + 1{,}5(15-7v_0)\eta_2\eta_3
\end{aligned} \\[2mm]
\begin{aligned}
C = {} & 4\left(\frac{G_f}{G_0}-1\right)(5v_0-7)\eta_1\varphi^{\frac{10}{3}} - 2\left(63\left(\frac{G_f}{G_0}-1\right)\eta_2 + 2\eta_1\eta_3\right)\varphi^{\frac{7}{3}} + 252\left(\frac{G_f}{G_0}-1\right)\eta_2\varphi^{\frac{5}{3}} + 25\left(\frac{G_f}{G_0}-1\right)(v_0^2-7)\eta_2\varphi \\
& - (7+5v_0)\eta_2\eta_3
\end{aligned} \\[2mm]
\eta_1 = \left(\frac{G_f}{G_0}-1\right)(7-10v_0)(7+5v_f) + 105(v_f-v_0) \\[2mm]
\eta_2 = \left(\frac{G_f}{G_0}-1\right)(7+10v_f)(7+5v_f) + 35(1-v_p) \\[2mm]
\eta_3 = \left(\frac{G_f}{G_0}-1\right)(8-10v_0) + 15(1-v_f)
\end{cases}
$$

Here, ν_f and ν_0 are the Poisson ratios of the filler and the matrix, respectively, and G_f and G_0 the moduli of the filler and matrix, respectively. The Poisson ratios of matrix and fillers are respectively ~0.5 and ~0.2, and the modulus of the matrix is negligible compared to the modulus of the fillers (3 to 6 orders of magnitude smaller), so after some calculations this equation yields a general solution:

$$(R+1)_{\mp} = \frac{-B'(\varphi) \mp \sqrt{B'(\varphi)^2 - 4 * A'(\varphi)C'(\varphi)}}{2A'(\varphi)}$$

One of the solutions is negative and can be discarded for physical reasons, the other one is plotted in Figure 3-3 (a) and (b). In the end there are only three parameters that must be considered in the model: the Poisson ratios of both filler and matrix, and the volume fraction.

3.6.2   Determination of C for filled rubbers
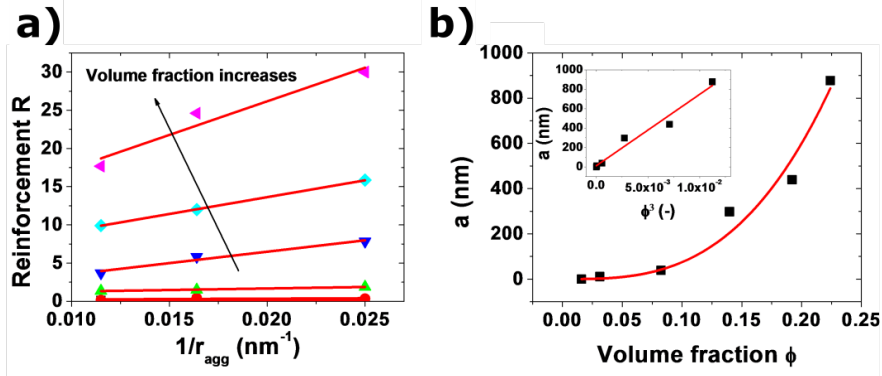
Figure 3-9. Filler-size-dependent reinforcement for filled NBR: (a) plot showing reinforcement versus the inverse of the radius for different volume fractions. (b) Slopes of lines in (a) as a function of the volume fraction of the filler beads. The solid line shows the cubic fit of this parameter; the inset illustrates the cubic dependence of reinforcement on the filler volume fraction.

C is determined for filled NBR as for the model system. The reinforcement (data in Figure 3-3a) is plotted as a function of the inverse of the radius of the aggregates, and then the slope a is fit to get C. The value found is 73 microns for filled NBR. This method could not be applied for the SBR because the aggregate size is not varied at a given volume fraction. As stated in the main text, C is found to be 40

microns for this sample, which is comparable to what is obtained for the NBR samples (73 microns).

3.6.3   The C parameter

The shear modulus of the composite material is given by affine theory (see the paper) as $G \approx b\kappa\varphi^3/r_{b/agg}$, where b is a dimensionless prefactor related to the height of the first peak of the pair correlation function of nanoaggregates. The reinforcement is defined as $R = G(\varphi)/G_0 - 1 \approx b\kappa\varphi^3/(r_{b/agg}G_0)$, where the last approximate equality considers only high volume fractions. Hence, the parameter C is obtained as $C = b\kappa/G_0$, where G_0 represents the shear modulus of the pure rubber with no fillers. In the microscopic model, κ represents the spring constant of the polymer-mediated interaction between two nanoaggregates and has dimensions [force/length], while G_0, by definition, has dimensions [force/length^2]. By introducing a generic length-scale l, $C = (b\kappa/l)/(G_0/l)$. Here, $G_{loc} = b\kappa/l$ has the dimension of an elastic modulus, which measures the rigidity of nearest-neighbour nanoaggregate interaction over the length scale l. If one takes $l=l*$ such that $G_{loc}(l^*) = G_0$, then clearly $C = l^*$. Therefore, C represents the critical length scale or critical average mutual separation l^* of two nearest-neighbour nanoaggregates for the elastic modulus of the nanocomposite to be equal to the elastic modulus of the pure rubber. In other words, the ϕ^3 reinforcement vanishes, or reduces to ESE, if the aggregates are on average farther apart than the critical separation distance l^*. In the systems studied here the average separation between two nearest-neighbour nanoaggregates is ~ 100 nm, which is much less than C (~ 50 μm), and the effective modulus of the nanoaggregate array is much larger than that of the pure rubber.

CHAPTER 4: MULTISCALE EFFECTS OF INTERFACIAL POLYMER CONFINEMENT IN NANOCOMPOSITES

4.1   Abstract

Dispersing hydrophilic nanofillers in highly hydrophobic polymer matrices is widely used to tune the mechanical properties of composite material systems. The ability to control the dispersion of fillers is closely related to the mechanical tunability of such composites. In this work, we investigate the physical – chemical underpinnings of how simple end –group modification to one end of a styrene – butadiene chain modifies the dispersion of silica fillers in a polymer matrix. Using surface–sensitive spectroscopies, we directly show that polymer molecular orientation at the silica surface is strongly constrained for silanol functionalized polymers compared to non-functionalized polymers because of covalent interaction of silanol with silica. Silanol functionalization leads to reduced filler aggregation in composites. The results from this study demonstrate how minimal chemical modifications of polymer end groups are effective in modifying microstructural properties of composites by inducing molecular ordering of polymers at the surface of fillers.

4.2   Introduction

For many natural and synthetic composite materials, enhancing or reinforcing the linear and nonlinear viscoelastic properties of polymer (elastomer) materials is accomplished by inclusion filler particles (e.g. carbon black, silica).[13–16] Mechanical properties of elastomer systems can be substantially increased, e.g., more than a 10–fold increase in shear modulus, by addition of fillers to the polymer matrix. Notably, this strengthening, or reinforcement, depends in a nontrivial manner on the distribution and size of fillers within the elastomer matrix.[10,11,123] Interfacial interactions between individual particles in aggregates, between the aggregates in agglomerates, and between particles and the polymer can modulate particle dispersion and influence the molecular motion of polymer chains in the material. Moreover, in nanocomposites containing nanoparticle fillers with large surface area, the particle dispersion is a critical element for tuning optical,[17,18] electrical, [19–21] biological, [22,23] and mechanical properties[58,118,124–126] of the materials. Unfortunately, controlling the filler distribution in many popular nanocomposite formulations, such as SiO_2–

particle reinforced rubber, is challenging because the typically highly hydrophilic fillers tend to aggregate in the hydrophobic host polymer melt. Previous approaches to overcome the hydrophobicity difference between the matrix and fillers include: (1) covalent coupling of the fillers to the polymer matrix using multifunctional molecules, for instance bis[3–(triethoxysilyl)propyl] tetrasulfide (TESPT)[27,29,40,127–130] or (2) lowering the surface polarity of the hydrophilic fillers by surface modification with silanes,[42,131,132] short hydrocarbons, [43,44] or polymer layers grafted on the filler surface.[45] A recently highlighted strategy for improving the dispersion of SiO_2 particles in styrene–butadiene rubber (SBR) is modifying the host SBR chains themselves with a single silanol functional group (Si–OH) at the end of the chain.[38,39,47] The appealing part of this concept is that the aggregate size (R_{agg}) of SiO_2 fillers can be varied in styrene–butadiene rubber (SBR) by simply changing the concentration of functionalized SBR (F–SBR) chains in the total SBR matrix. However, the impact of polymer functionality on polymer–filler interaction – if any – is still unclear because of the complexity in previously studied systems and inability to investigate the polymer–substrate physicochemical properties.[47]

In this work, we investigate the influence of a single Si–OH end functional group on 50% of total SBR chain ends on polymer–silica interaction at the molecular level by studying well–defined systems with a combination of microscopy and surface–sensitive spectroscopy. We evaluate the adhesion and molecular ordering of both F-SBR and non-functionalized or bare SBR (B-SBR) polymers to SiO_2 surfaces. Our spectroscopic results demonstrate preferential adhesion of F-SBR chains to SiO_2 surfaces and directly show enhanced ordering of polymer chains in F–SBR–SiO_2 films compared with B–SBR–SiO_2 from surface specific sum frequency generation and near edge X–ray absorption fine structure spectroscopy. Finally, depth–resolved X–ray photoelectron spectroscopy was used to show that the Si–OH group formed a covalent bond with OH–terminated silicon surfaces. The multiscale effect of using the Si–OH functionalized SBR starts with covalent interaction between F-SBR and SiO_2 fillers that leads to increased polymer ordering and ultimately manifests as improved filler distribution and reduced aggregation at the microscopic level compared to B–SBR–SiO_2 composites.

4.3   Materials & methods

Materials.

Two types of SBR polymers were employed: 1) silanol end–functionalized SBR (F–SBR) and 2) bare SBR (B–SBR) polymers (see Figure 4-1(c, inset)). Initiation of anionic polymerization of both random F-SBR and B-SBR copolymers are done by using *n*–BuLi in a methlycyclohexane. *N*–(1,3–dimethylbuthyl)–*N'*–phenyl–*p*–phenylenediamine and 4,4'–methylene–bis–2,6–*tert*–buthylphenol were used as antioxidants during the polymerization of both copolymers. Protic terminating agent was used to terminate the B-SBR polymerization. Termination of the F-SBR polymerization was obtained by reaction with hexamethylcyclotrisiloxane in order to have silanol end group at one end of each F-SBR chain. Functionalized end–group of F-SBR can be chemically written as SBR–SiMe$_2$–OH. Functional group fraction in one end of all F-SBR chains was reported previously as greater than 98% according to the results from ^{1}H and ^{29}Si NMR.[47] In the same previous paper, microstructures of both polymers are also shown similar to each other due to their identical polymerization steps. Each chain of both copolymers statistically consists of 26 wt % of styrene and 74 wt % of butadiene units (41 wt % of 1,2–butadiene and 59 wt % of 1,4–butadiene units).[47] These subunits are indicated in every molecular structure shown in this chapter by using the letters m, n, k and p for styrene, 1,2–butadiene and 1,4–butadiene (k+p, for trans and cis), respectively (see section 2.1 for details). The polymer chain stock solutions (40 mg/mL THF) were prepared by dissolving bulk slabs of B-SBR and F-SBR in THF for 4 days at 4°C. The 4–day incubation time was necessary to completely solubilize the polymers in THF. Formulation details of the full nanocomposites can be found elsewhere.[47] Simplified nanocomposites were prepared according to the protocol presented in section 2.1 in Chapter 2.

Transmission electron microscopy imaging and image processing.

Cryo-sectioning and TEM imaging of the nanocomposites were performed as explained previously (section 2.3 in Chapter 2). The aggregates were determined by applying a thresholding routine to highlight silica aggregates against the rubber background in each TEM image using ImageJ. The following steps were followed: 1) OK Brightness and Contrast, 2) unsharp mask (radius was set to 45 and mask weight was used as 0.6), 3) threshold with a value of the difference value between mean and stdDev of each image, which can be found in histogram after the step 2,

and 4) counting (from one primary filler to infinite size). This procedure was kept constant for all samples measured. The output from the image analysis was: aggregate projected area (A), perimeter, and centroid location. We assume a circular shape with the measured projected area (A) for each aggregate from which we calculated the aggregate radius (R_{agg}).

Contact angle measurements.

Teflon and silica window substrates were first cleaned by immersing in piranha solution (3:1 (v/v) H_2SO_4: H_2O_2) for 10 min then rinsed with milli Q water and absolute ethanol. The substrates were then left in a desiccator for 24 h for complete drying. Spin coating of the B-SBR and F-SBR films on Teflon and silica window surfaces were done by using a spin coating device Model WS–400–6NPP/LITE (Laurel Technologies Corp., North Wales, USA). 100 µL from each 40 mg/mL stock solutions of F-SBR and B-SBR were deposited on the substrates during 1 min at 3000 rpm. After the spin coating, the substrates with polymer films on the top were left in desiccator for 24 h.

For understanding a possible polarity difference between the B-SBR and F-SBR due to polymer functionality, we measured the contact angle of water as probe liquid on aforementioned spin coated polymer films on the top of Teflon or silica windows. The contact angle experiments were performed with an OCA35 goniometer (DataPhysics, Germany). The advancing contact angle of the spun coated rubber films was evaluated by placing an initial sessile droplet of milli Q water of 5 µL on the surfaces. The volume of the deposited droplet was increased up to 25 µL at a rate of 0.5 µL/s while keeping the needle in the drop. At the plateau regions of the contact angle (CA) in increasing volume the advancing CA for water of the polymer films is obtained. Advancing CA presented in Figure 4-11 are reported after averaging the mean values from at least two different spot per spin coated film and three different plateaus (cycles) per each of these spots.

Drop cast polymer film preparation and characterization.

Drop cast films of pure F-SBR or B-SBR were prepared for various spectroscopy measurements in this study, and the following method was used, 1500µL from each 40 mg/mL of polymer stock solutions were drop cast on cleaned IR–transparent silica windows (Infrasil, International Crystal Laboraties, Garfield). Windows were cleaned by following the previously mentioned piranha cleaning protocol of the substrates for before the spin coating.

Teflon rings were used as molds for film casting. The drop cast polymer films were kept inside a fume hood for 1 h before being transferred to a vacuum desiccator for 24 h in order to obtain THF–free polymer films. After complete removal of the THF from the polymer, the residual dry film thickness was found to be 150 μm – 180 μm by measurement with a microscope (IX81, Olympus, Tokyo) using a 40X, NA 0.75 objective lens (Olympus, Tokyo).

Infrared spectroscopy.

Fourier transform infrared spectroscopy (FTIR) was used to measure characteristic peaks of the residual polymer films adhered to a piranha–cleaned silicon wafers and absorption of IR light by polymer films on silica windows. Samples were measured with a Nicolet 730 FTIR spectrometer. All FTIR spectra shown were averaged over three different regions of the drop cast film. The integration time for the IR measurements was 800 s. Average IR intensity values between the frequencies of 2120 cm^{-1} and 2140 cm^{-1} of each averaged FTIR spectra were used for the background subtraction.

Sum–frequency generation spectroscopy.

Sum frequency generation (SFG) experiments were performed on the silica–polymer interface of drop–cast polymer films with broadband SFG system in the following way. 1.7 mJ of energy from a Ti:sapphire regenerative amplifier (Spitfire Ace, Spectra–Physics; 800 nm, 5 mJ, 1 kHz, ~40 fs) was used to pump a commercial optical parametric amplifier (Topas–C, Spectra–Physics). This resulted in 4 μJ infrared (IR) pulses centered at 3000 cm–1 with a full width at half maximum (FWHM) of ~400 cm–1. Visible narrow band pulses with a center wavelength of 800 nm and FWHM of ~15 cm–1 were obtained by passing part of the 800 nm laser output through an etalon (SLS Optics Ltd). The IR and visible beams were spatially and temporally overlapped on a film sample with incident angles of ~30° (visible) and ~40° (IR) with respect to the surface normal. The energy of the visible and IR pulses at the sample were 5 μJ and 3 μJ, respectively, to avoid sample damage. The reflected SFG signal was directed to a spectrograph (Acton Instruments) and detected with an electron–multiplied charge–coupled device (EMCCD) camera (Newton; Andor Technologies). Spectra were recorded using Andor Solis software with an integration time of 10 min. All spectra where collected under SSP polarization (s–polarized SFG, s–polarized visible, p–polarized infrared).

The SFG intensity is proportional to the square of the second order nonlinear susceptibility $\chi^{(2)}$ of the sample and the visible and infrared electric fields:

$$I_{SFG} = \left| E_{SFG} \right|^2 \propto \left| \chi^{(2)} E_{VIS} E_{IR} \right|^2 \qquad (4.\,1)$$

The SFG is enhanced when the frequency of the incident infrared field is resonant with a vibrational mode present at the interface. The susceptibility $\chi^{(2)}$ consists of a resonant (RES) and nonresonant (NR) term.

$$\chi^{(2)} = \chi^{(2)}_{NR} + \chi^{(2)}_{RES} = A_{NR} e^{i\varphi_{NR}} + \sum_n \frac{A_n}{\omega_{IR} - \omega_n + i\Gamma_n} \qquad (4.\,2)$$

where A_{NR} is the amplitude of the nonresonant susceptibility, φ_{NR} the phase, A_N the amplitude of the nth resonance with frequency ω_n, and Γ_n the line width of the vibrational transition. To correct for the spectral shape of the IR pulse, data were normalized to a reference spectrum from a 100–nm evaporated gold layer on IR–transparent silica. Equation 3 was then used to fit the normalized SFG spectra and extract the peak amplitudes and positions for the different resonances. The Maximum Entropy Method for phase retrieval was used to verify the phase of the peaks and the non–resonant signal.[133] All SFG spectra shown in this work are an average of 12 spectra (four spots on two independent samples).

Near–edge X–ray absorption fine structure (NEXAFS) microscopy.
Near–edge X–ray absorption fine structure (NEXAFS) microscopy was performed on the silica–polymer interface of drop–cast polymer films; however, before placing the drop cast polymer films in the NEXAFS analysis chamber, the bulk polymer layer was peeled off the silica window by using a fine tweezer. This was done in order to analyze the thin polymer film in close proximity to the silica surface.

NEXAFS images were collected at the U7 beamline at the National Synchrotron Light Source (NSLS – Brookhaven National Laboratory). An X–ray beam, with energy scanned around the carbon K–edge was raster scanned across an 18 × 13 mm^2 area on the sample. The spatially resolved partial electron yield (PEY) was measured using a rapid imaging analytical tool (LARIAT, Synchrotron Research Inc.). The step size for the scans was 0.1 eV (2 s dwell time). The emitted photoelectrons were guided to an electron yield detector by a full field imaging parallel magnetic field. This produced a series of NEXAFS images with a 50 μm

spatial resolution, which was used for the small spot analysis of different areas of the films. The spectra shown are representative of four spots analysed on the sample surface. To eliminate the effect of incident beam intensity fluctuations and absorption features in the beamline optics, the PEY was normalized by the drain current signal of a clean gold mesh located upstream of the analysis chamber along the path of the incident X–ray beam. All the images and spectra from NEXAFS analysis in this paper have been pre– and post–edge normalized using the Athena software package.

Ultrathin spun coat polymer film preparation and X–ray photoelectron spectroscopy.

For the XPS measurements, 20 µL drops from each 10 mg/mL F–SBR/THF and B–SBR/THF solutions were deposited onto piranha cleaned Si wafers. These Si wafers with polymer solution drops on the top were then spin coated for 60 s at 3000 rpm . After the spin coating, the samples were kept under vacuum and then they placed inside of the XPS ultra-high vacuum chamber. The approximate thickness of the spin coat polymer films was determined using a KLA Tencar P–16 stylus profiler (KLA Tencar, Milpitas, California). XPS was conducted using a Kratos Axis Ultra spectrometer (Kratos, Manchester, England) using an Al Ka excitation source with a photon energy of 1487 eV. An argon gas cluster ion source (GCIS) was used for depth profiling the atomic composition of the polymer films. The sputter source was set to a raster size of 1.5 mm × 1.5 mm, and ~200 etching steps were required to fully remove the 60 nm polymer film.

The data was acquired in small spot mode (0.1 mm spot diameter) using a 0° take–off angle, defined as the angle between the surface normal and the axis of the analyzer lens. The analyzer pass energy was set to 80 eV for composition analysis. The molecular environment of the samples was probed by high–resolution spectra (analyzer pass energy = 20 eV) from the C1s and O1s regions. The charge neutralizer was always used during spectra collection (filament current 1.8 Å, charge balance 2 V, and filament bias 1.3 V). The binding energy scales were calibrated to the main bulk Si 2p emission at 99.3 eV, and a linear background was subtracted for all peak quantifications. The peak areas were normalized by the manufacturer supplied sensitivity factors and surface concentrations were calculated using the Kratos Vision software.
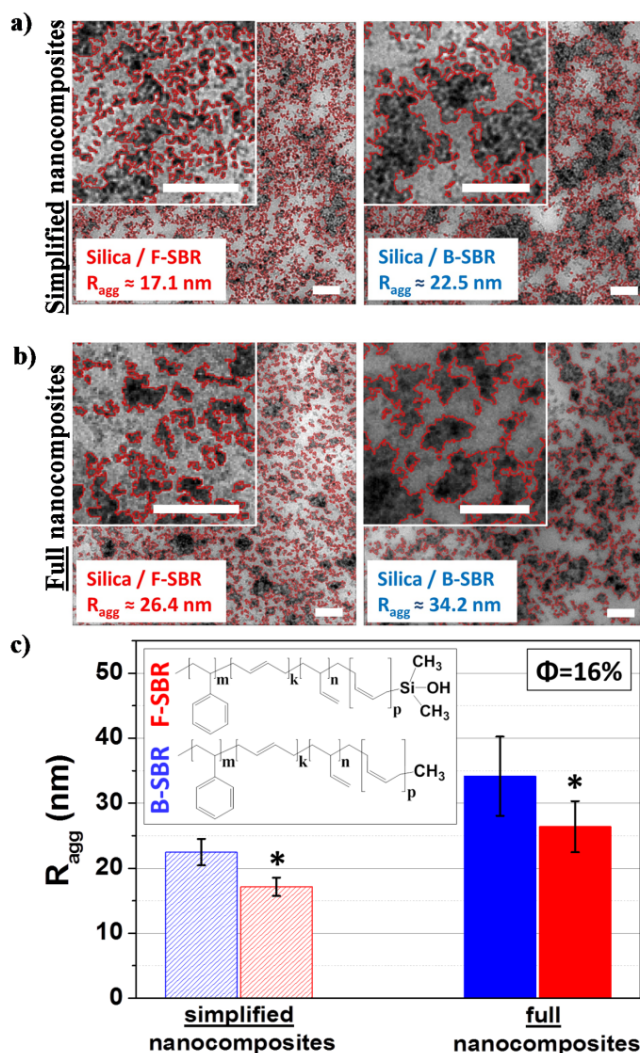
Figure 4-1. TEM images of (a) simplified nanocomposites, and (b) the full nanocomposites. All samples contain 16 vol. % of silica fillers in B-SBR or F–SBR. Scale bars are 200 nm. (c) Average aggregate sizes (R_{agg}) of simplified and full nanocomposites. Red and blue bars represent R_{agg} of samples with F-SBR and B-SBR polymeric matrices, respectively. The inset shows the molecular structures of the two polymers. Letters, m, k, n and p represent the amounts of statistically ordered polymer units of both random copolymers (see Chapter 2 for details). Histograms of the aggregate sizes of all the composites are presented in appendix (Figure 4-7). Asterisks denote statistically significant differences ($p < 0.05$) of R_{agg} between B–SBR–silica and F–SBR–silica samples (1–way ANOVA with Tukey's). Error bars are standard error of mean.

4.4   Results and Discussion

4.4.1   Modifying SiO$_2$ Filler Aggregates by functional-SBR

The molecular structures of the two styrene – butadiene (SBR) polymers are shown in Figure 4-1(c, inset). The synthesis of the two polymers has been described previously, and the basic protocol is summarized in section 4.3.[47] The only difference between the two polymers is a single silanol (Si–OH) end group on "functionalized" SBR (F–SBR), corresponding to 1 Si–OH at the end of an ~ 150 g mol^{-1} SBR chain. The other polymer, with terminal methyl groups, will further be referred to as "bare" SBR (B–SBR). In complex, industrial silica–filled composites, F-SBR chains have been shown to substantially affect silica nanofiller aggregation and distribution.[39,47] This difference is purported to occur via interaction of the Si–OH on the polymer to the silica surface, which creates a brush around fillers to reduce the filler–filler aggregation. This hypothesis is in line with previous studies that have shown that grafting of polymer chains on silica surfaces reduces filler aggregation in hydrophobic environments.[129] However, explaining the origin of changing nanofiller dispersions in SBR as a result of polymer functionality alone is not obvious in complex industrial formulations. They include many additional ingredients e.g. TESPT, octyltriethoxysilane (OCTEO), additional (proprietary) oils, and antioxidants, all of which can influence particle dispersion.[39,47]

To isolate the effect of silanol end–functional groups on filler aggregation in silica loaded SBR composites, we begin by analyzing the size distribution of silica aggregates (R$_{agg}$) in simplified nanocomposite systems. These composites contain only the polymer (F-SBR or B–SBR) and silica nanofillers (see Chapter 2). Transmission electron microscopy (TEM) images of ultrathin sections (~ 50 nm) of simplified nanocomposite systems were acquired and processed to identify aggregates (dark contrast regions) dispersed in the polymeric matrix (Figure 4-1a). For comparison purposes, full nanocomposites were also imaged and processed to identify aggregates (Figure 4-1b). We quantified the effective aggregate radius R$_{agg}$ of each different composite by averaging the area of 4000 aggregates from each composite and assuming a circular shape, similar to what is done in small angle X–ray scattering. Figure 4-1c shows that in both full and simplified nanocomposites,

samples containing F-SBR (red bars) have smaller aggregates than those with B-SBR(blue bars). We note that while TEM is certainly not the optimal choice for analysis of nanoscale aggregates in polymer matrices, we have compared our results with those from small angle X–ray scattering (SAXS) for full nanocomposite systems and find reasonable agreement at 16 % volume fraction with more dispersity at 24 % volume fraction (Figure 4-6). The thresholding step in our image analysis is subject to the image contrast between polymer and fillers (see 2.3 in Chapter 2), and because the distance between aggregates decreases at higher filler volume fraction, this makes absolute aggregate size quantification less accurate at higher volume fraction. Furthermore, interpretation of aggregate sizes as a function of volume fraction is difficult as competing effects (e.g. particle shearing and energetically–driven aggregation) can oppositely affect the aggregate size and disentangling these effects is challenging.[47,134,135] Nevertheless, the consistent reduction of aggregate size seen in F-SBR composites compared to B-SBR composites from both TEM image analysis and SAXS for 16% and 24% volume fraction filler demonstrates that our quantitative aggregate analysis is robust for comparing aggregate sizes at the same volume fraction with different polymer matrices (Figure 4-6). Thus, our results show that, both in full and simplified composites, a single Si–OH end–functional group on an SBR polymer chain is able to modify the aggregation behavior of silica nanofillers in composite systems.

4.4.2 Enhanced attachment of functional-SBR on SiO$_2$ Surfaces

To better understand the origin of the aggregate size decrease in silica/F-SBR samples, we compared the adhesion of B-SBR and F-SBR polymers with planar SiO$_2$ surfaces. Polymers were drop cast onto piranha–cleaned silicon wafers from a stock solution of polymer in THF (see section 4.3). Cleaned silicon wafers typically have a thin (SiO$_2$) oxide layer after piranha cleaning.[46,136,137] We tested if Si–OH groups on the F-SBR polymer increased attachment to the wafers by rinsing the polymer–coated wafers in a THF bath for 80 s. Since the polymers were initially dissolved in a THF solution, rinsing with THF should solubilize weakly adhered polymer chains in both B-SBR and F-SBR films. After this procedure, a visible film was left on the wafer coated with F–SBR, but
no film was observed on the B-SBR coated wafer (Figure 4-2a). We subsequently used Fourier transform infrared spectroscopy (FTIR) to determine the chemical composition of the residual film on the F-SBR coated silicon wafer. Representative spectra from the THF–washed wafers are shown in Figure 4-2b. These spectra

confirm the presence of SBR after THF rinsing for the drop cast F-SBR film while no chemical moieties (beyond those of the Si wafer) were apparent for the corresponding B-SBR sample. From these data, we conclude that attachment of the F-SBR polymer to the piranha–cleaned silicon wafer is clearly enhanced by the single Si–OH group on the chains.
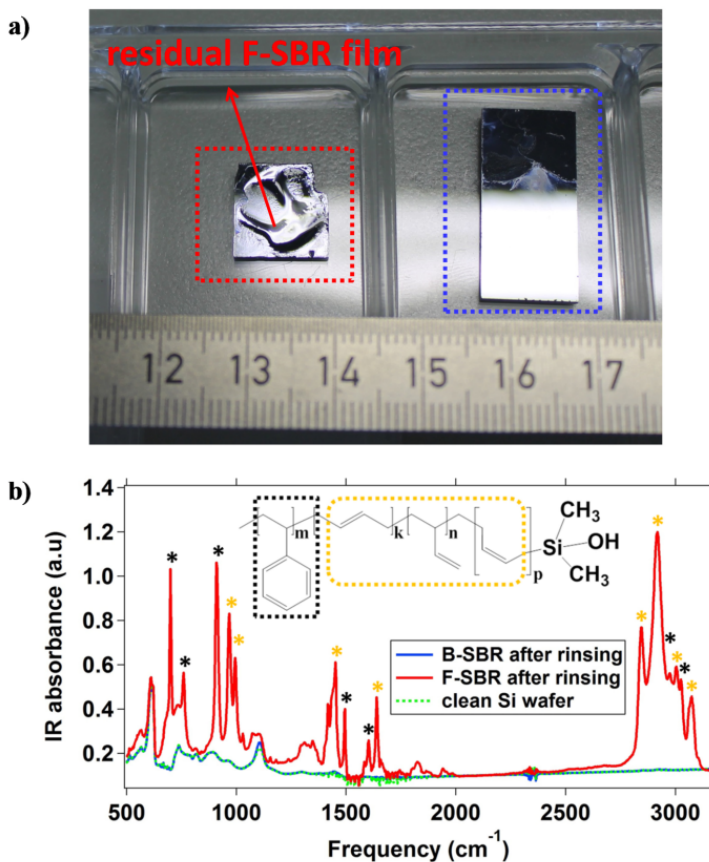
Figure 4-2. (a) Photographic images of F-SBR (left) and B-SBR (right) residue on silicon wafers after rinsing polymer films with THF. (b) FTIR spectra of residual films on Si wafer after rinsing in THF. Clear peaks from SBR are observed for the F-SBR polymer (red) while only Si wafer peaks (green–dashed) are seen after the B-SBR polymer (blue) has been rinsed. Characteristic groups of SBR are shown by outlines in yellow or black on the chemical structure. The same colours are used to identify particular vibrations (marked by asterisks) in the spectrum associated with each characteristic group.

4.4.3 Ordering of functional-SBR on SiO$_2$ Surfaces

The enhanced attachment of F-SBR chains on silicon surfaces presumably originates from the Si–OH group interacting with the SiO$_2$. We further explored the surface – polymer interaction to determine if any differential molecular orientation was induced by Si–OH mediated attachment of the F-SBR polymer to silica. Vibrational sum frequency generation (SFG) spectroscopy and near edge X–ray absorption fine structure (NEXAFS) spectroscopy were used to measure molecular order of the polymer at the silica surface. SFG is a second order nonlinear vibrational spectroscopy that relies on frequency – mixing of an infrared with a visible laser pulse to generate light with the sum frequency. The SFG intensity is strongly enhanced when the infrared laser wavelength is resonant with molecular moieties (e.g., CH$_2$, C=C, or Si–CH$_3$ groups) that are present and noncentrosymmetrically oriented at an interface. SFG has a typical probing depth of ~2–3 molecular layers[138] and has been used extensively to characterize polymer films on various interfaces[139–144], making this technique well–suited for our system. For SFG (and NEXAFS) experiments, we used drop cast films of B-SBR and F-SBR on cleaned, infrared–grade silica windows – without THF washing. Silica windows were used instead of wafers because visible light transparency is required for SFG experiments. SFG spectra were collected from the silica window surface – polymer interface by passing the laser beams through the silica to the silica–polymer interface as shown in Figure 4-3a. In principle, polymer SFG signals should come from both the polymer–silica and polymer–air interfaces. However, in these samples the polymer–air SFG signal is negligible because the infrared light in the CH–region is strongly absorbed by the drop cast polymer layer (see Figure 4-8a), so SFG is only detected from the polymer–silica interface. SFG spectra were recorded under SSP polarization conditions (s–polarized SFG, s–polarized visible and p–polarized IR). Figure 4-3b shows the SFG spectra from the F–SBR–silica interface in red and the B–SBR–silica interface in blue. Spectra from both polymers indicate some degree of molecular order at the silica interface as evidenced by the peaks in the spectra. Control spectra from a THF solution dried on the silica window (without any polymer) showed a 300% and 500% decrease in intensity at ~ 2950 cm^{-1} compared to B-SBR and F–SBR, respectively (Figure 4-3b, black).

The spectra from the F–SBR–silica interface shows clear deviation from the B–SBR–silica interface at ~ 2915 and 2950 cm^{-1}, in addition to a larger overall amplitude. In order to assign peak frequencies and identify the specific moieties

contributing to the spectra, we fit the SFG data with a standard model explained in the Methods (using parameters that can be found in Table 4-1). The fitting results are also depicted in Figure 4-3b (thick lines) and show good agreement with the acquired data. The robustness of the fit was further demonstrated by comparing the reconstructed resonant spectra from the fits with the extracted resonant spectra via the commonly used maximum entropy method (MEM) analysis (Figure 4-8b).[133] These two independent analyses show similar spectra, underscoring the accuracy of the fits to allow reliable peak assignment.
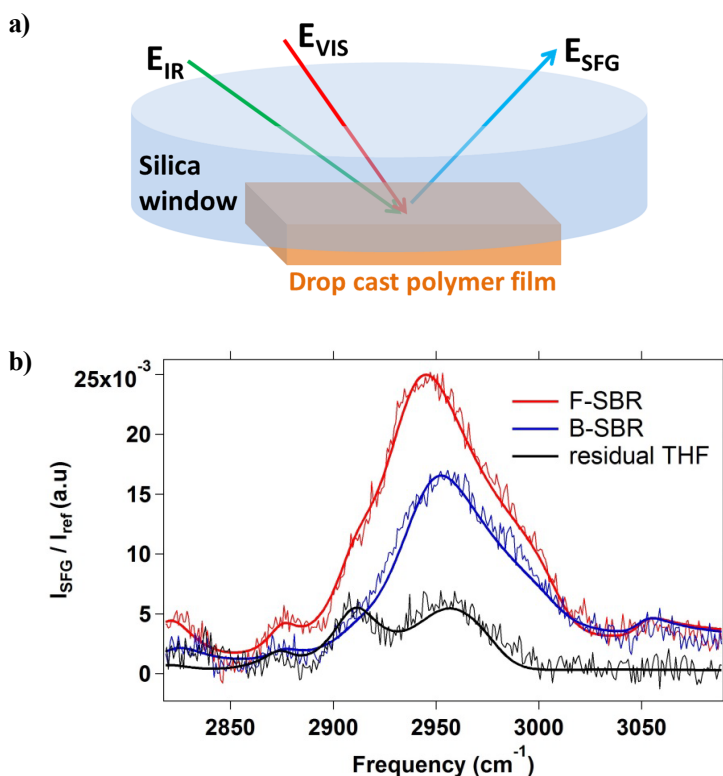
Figure 4-3. (a) Schematic illustration of the SFG measurements of drop cast polymer films on IR–transparent silica. Two incoming photons (infrared and visible shown by green and red arrows, respectively) are spatially and temporally overlapped at the window–polymer interface and generate a photon (E_{SFG}, shown by the blue arrow) with the sum of these frequencies. (b) Normalized (by a reference spectrum from a gold coated window) SFG spectra measured from F-SBR (red) and B-SBR (blue) and residual THF without polymer (black). Thick lines are fits to the spectra based on a standard model (see section 4.3).

From the fitting results and previous work on polymer – interfaces for polydimethylsiloxane (PDMS) in contact with silica, we can identify likely resonances in the SFG spectra. The PDMS–silica interface shows symmetric and asymmetric Si–CH$_3$ vibrations at roughly 2915 cm^{-1} and 2960 cm^{-1}.[145] Similarly, we assign the 2910 cm^{-1} shoulder and 2940 cm^{-1} peak in the F-SBR spectrum to these two Si–CH$_3$ vibrations (Figure 4-3b, red). In the B–SBR–silica sample, the broad signal at 2945 cm^{-1} possibly originates from the CH$_3$ end group; however, a definitive assignment is not possible. Nevertheless, the identity of the peaks (Si–CH$_3$) in the F–SBR–silica system and the overall larger intensity (compared to B–SBR) show that the Si–OH group in F-SBR is in close proximity to the silica and stabilizes a conformation of the polymer in which the neighboring Si–CH$_3$ groups exhibit a noncentrosymmetric organization.

As a complementary technique to SFG, NEXAFS spectroscopy allows one to determine the spatial orientation of chemical structures based on absorption of a polarized X–ray beam by the sample.[52,146] NEXAFS spectra were measured on the same type of drop cast films as used for SFG measurements. Prior to introducing the samples into the NEXAFS analysis chamber, the bulk drop–cast polymer layers were physically ripped from the silica window, leaving behind a residual polymer film on the SiO$_2$ surface (Figure 4-4a). NEXAFS spectroscopy probes the molecular structure of surface adsorbed species by measuring characteristic absorption resonances corresponding to electronic transitions from atomic core levels to unoccupied molecular orbitals.[52] Carbon K–edge spectra from randomly chosen regions of interest of B-SBR and F-SBR residues on silica windows, acquired at 70° and 30° relative to the incident X–ray beam, are presented in Figure 4-4b. The absorption at 285.4 eV, from π* C=C orbitals, is present in all spectra taken from both types of polymers.[147,148] Moving to higher X–ray energies, we observe a shoulder at 288 eV and a broad resonance at 293 eV related to R*/C–H σ * and C–C σ * molecular orbitals, respectively.[51,148–150]

Preferential orientation of molecular bonds was investigated by subtracting spectra from 70° and 30° tilt angles. Difference spectra (70°–30°), from B-SBR and F-SBR residual films are shown in Figure 4-4c. A comparison of the two difference spectra (Figure 4-4c) shows a substantially higher degree of order (positive dichroism) for the π* C=C feature for the F-SBR polymer residue interfaced with silica with a peak height of 0.2 at 285.2 eV. No significant dichroism was observed for the B-SBR residue–SiO$_2$ interface, especially in the π* C=C region

of the difference spectrum (5–fold lower than for F–SBR). This shows that the functionalization of the SBR polymer with a single Si–OH induces a specific orientation of C=C double bonds, such that the C=C bonds are somewhat upright relative to the substrate.
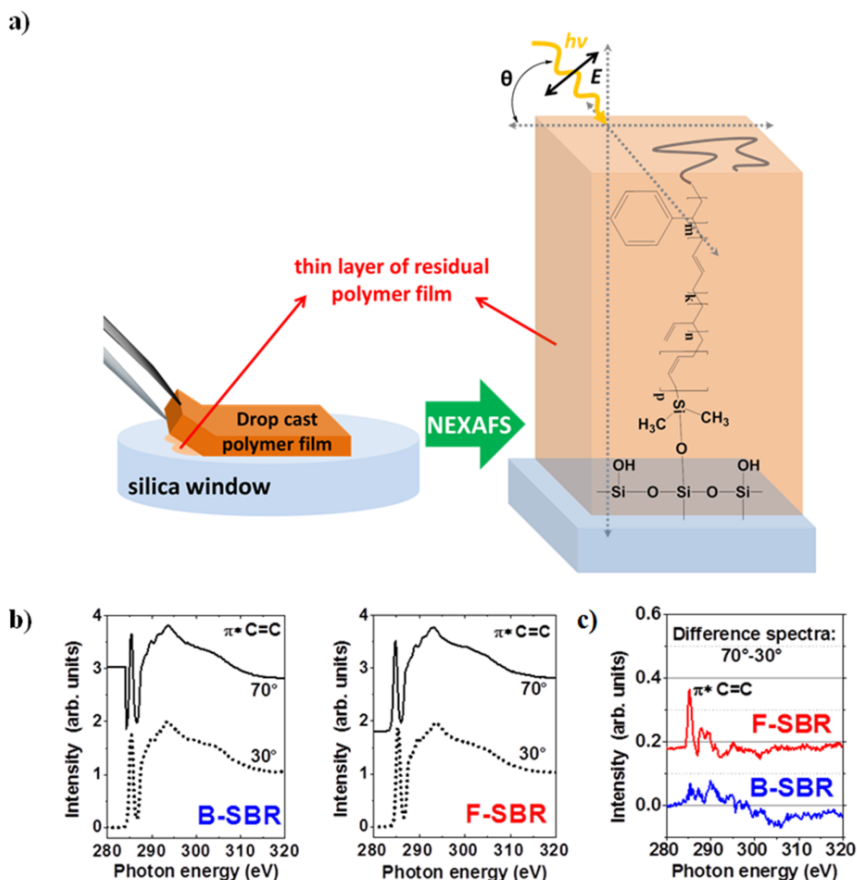
Figure 4-4. (a) Illustration showing removal of drop cast polymer films using tweezers before the NEXAFS measurements. Silica windows with the residual polymer film were introduced into the NEXAFS analysis chamber. Preferential orientation of molecules (e.g., π^* C=C orbitals within SBR chain) to the silica surface can be determined from changes in X–ray absorption at different sample rotation (θ) relative to the incident X–rays. (b) Carbon K–edge spectra extracted from random regions of B-SBR (left) and F-SBR (right) residual films on silica acquired at 70° (straight lines) and 30° (dotted lines). (c) The difference spectra (70° – 30°) are shown in red and blue for F-SBR and B–SBR, respectively. Spectra in (b) and (c) were vertically offset for clarity.

4.4.4 Covalent Nature of the Interaction between functional-SBR and Silica

Our results show decreased silica aggregation, enhanced adhesion, and enhanced molecular ordering of F-SBR polymers at silica interfaces, relative to B-SBR polymers, as a result of the presence of the Si–OH end functional group on the F-SBR polymer. However, none of the above measurements have addressed the question how the Si–OH group interacts with silica: chemisorption or physisorption. In order to address this question, we studied the elemental composition and chemical state of the B-SBR and F-SBR polymer films spun cast onto piranha–cleaned Si wafers using depth–resolved X–ray photoelectron spectroscopy (XPS). Spin–coated polymer films (thickness ~ 60 nm) were depth profiled by repeated sputtering using an argon cluster source and XPS analysis of the exposed surface (see section 4.3 and Figure 4-9). This process provides a snapshot of atomic concentrations (%) at different depths in the polymer film as it is etched toward the substrate. By plotting the atomic concentration of Si and C versus etch time, we can define a particular etching period that best reflects the polymer–substrate interface (Figure 4-9).

The C 1s spectra of both F-SBR and B-SBR at the SiO_2 layer (which is present after piranha etching silicon) show a main emission near 285.3 eV assigned to aliphatic and aromatic CC bonds (Figure 4-5a).[151–153] Spectral fitting reveals that the spectra for the F-SBR– SiO_2 interface contain a second peak near 286.4 eV, which can be assigned to C–Si–O or Si–C bonds coming from the Si–OH end functional groups at the end of F-SBR chains.[154–157] This additional peak supports the conclusion from SFG that the Si–OH end functional groups are condensed at polymer–Si wafer interface and not in the bulk film (Figure 4-10a). Looking next at the corresponding O 1s spectra of both polymers at SiO_2 layer, we observe a common peak at 531.8 eV originating from Si–O bonds at the Si wafer surface.[158,159] Similar to the C 1s spectra, we identified an additional peak after fitting the O 1s spectrum for F-SBR(Figure 4-5b). The second peak near 533.7 eV can be assigned to Si–O–R and Si–O–Si bonds,[155,158,160] and appears only at the F–SBR–silica interface – not in the bulk film (Figure 4-10b).

This observation is corroborated by the Si 2p spectra shown in Figure 4-5c. The main spectral features near 104.4 and 99.3 eV in both spectra related to Si–O–Si species within the thin oxide layer[160–163] are accompanied by a peak near

102.7 eV – only in the F-SBR spectra. The latter peak can be assigned to C–Si–O–Si.[154,158,162,164] Together, the additional peaks from C 1s (286.4 eV), O 1s (533.7 eV) and Si 2p (102.7 eV) spectra at the polymer–substrate interface led us to the following conclusions: (i) the $(CH_3)_2$–Si–OH end functional groups of F-SBR chains are enriched at the surface of the Si wafer and not detectable in the bulk film and (ii) the formation of chemical bonds between the Si–OH group and the silicon substrate, which leads to the formation of $(CH_3)_2$–Si–O–Si moieties at the interface as the result of a condensation reaction.
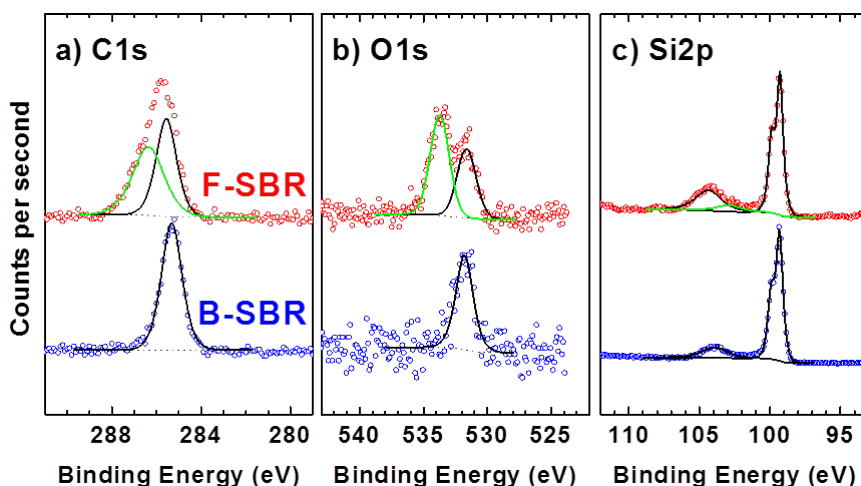
Figure 4-5. XPS spectra of the (a) C 1s, (b) O 1s and (c) Si 2p from the polymer–wafer interface along with fit results (see section 4.3 for details) collected from the F-SBR (red) and B-SBR (blue) films. Argon cluster etching time for the B–SBR–Si wafer interface is between 180 – 360 s. The F–SBR–Si wafer interface XPS results were extracted from etching times between 210 – 390 s. Figure 4-9 shows atomic % for C 1s, O 1s, and Si 2p during the entire argon etching times for both polymer samples. In all the XPS spectral fits, green and black lines are additional and common peaks, respectively, for both polymers.

4.5   Conclusions

In this work, we demonstrate that single Si–OH end groups on SBR chains are sufficient to enhance the interaction of SBR chains with silicon and SiO_2. The increased interaction manifests as stronger adhesion of the F-SBR chains to silicon surfaces as compared to B-SBR chains. Together with increased adhesion, the

additional interaction of the Si–OH functionalized polymer with SiO_2 fillers ultimately led to reduced aggregation of the silica nanofillers within the SBR matrix. The fact that the simplified and full composites showed similar reduced aggregation in F-SBR compared to B-SBR polymers suggests polymer–filler interactions also contribute to improving the dispersion of fillers in the more complex melt formulations as well. The idea of grafting polymer chains to silica particle surfaces with end group modifications has been previously demonstrated, though in the context of hydrophilic polymers, to study polymer segmental motion at silica interfaces.[165–167] This is quite different from the current study in which a hydrophobic rubber – SBR – was attached to silica using a terminal silanol group, which allows identification of functional (aggregation) and physical chemical (molecular ordering) differences when compared to methyl–terminated SBR.

To further explore the molecular origin of the improved adhesion of F-SBR chains to glass surfaces, we employed multiple surface–specific spectroscopies. From these measurements, we observed strong dichroism in carbon K–edge spectra from NEXAFS showing ordering of C=C bonds in the F–SBR/silica system. Further experiments with SFG showed that the F–SBR–silica interfaces exhibited Si–CH_3 signals that were larger than in B-SBR films. Finally, XPS spectra showed covalent bonding of Si–OH groups with silicon substrates in F-SBR films. These findings, along with the polymers having identical hydrophobicity (Figure 4-11), show that interaction of a single Si–OH group from the F-SBR polymer with the SiO_2 filler surface results in polymer ordering at the silica surface, which thereby decreases filler aggregation in the nanocomposites. While it is possible that specific, covalent attachment of polymers to an interface can cause disorder in the case of multivalent attachment, the combined results from SFG and NEXAFS surface spectroscopies for F-SBR films demonstrate that covalently attached polymers are more ordered at the silica interface.[168,169] The results from this study provide a mechanistic basis for future attempts to directly graft hydrophobic host polymer matrices to hydrophilic fillers with the aim of improving filler dispersion and mechanical properties of composite materials.

4.6 Appendix II
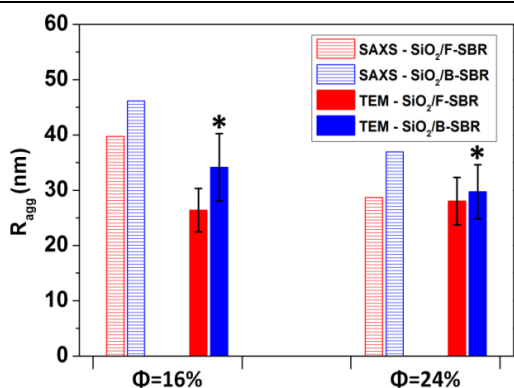
Figure 4-6. Aggregate size (R_{agg}) results from small angle X-Ray spectroscopy (SAXS) analysis of silica/F-SBR (red color horizontal patterned columns) and silica/B-SBR (blue color horizontal patterned columns) samples loaded with 16%vol. and 24%vol. of silica fillers inside shown with the R_{agg} results from TEM image analysis (solid columns with same colour codes). Asterisks represent statistically significant differences ($p < 0.05$) of R_{agg} between B-SBR-silica and F-SBR-silica samples (1-way ANOVA with Tukey's). Error bars are standard error of mean.
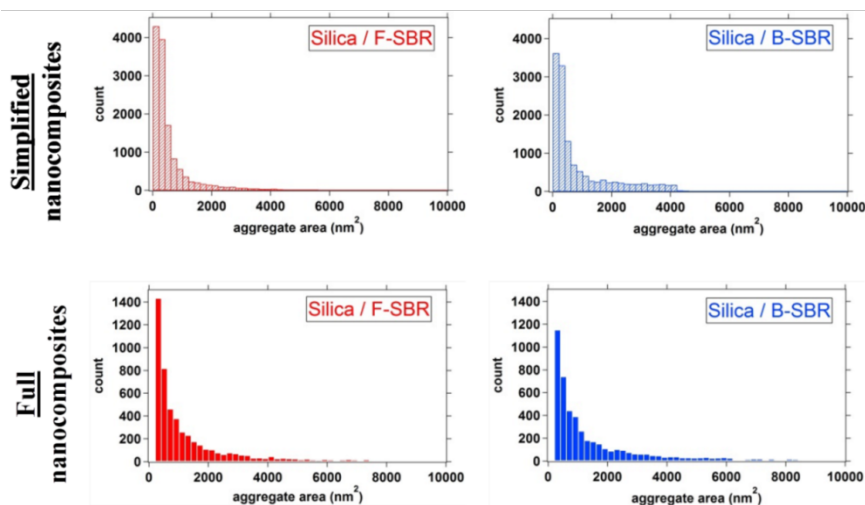
Figure 4-7. Histograms from the TEM image size analysis results of (upper column) simplified and (lower column) full nanocomposites whose images and R_{agg} sizes are presented in Figure 4-1.
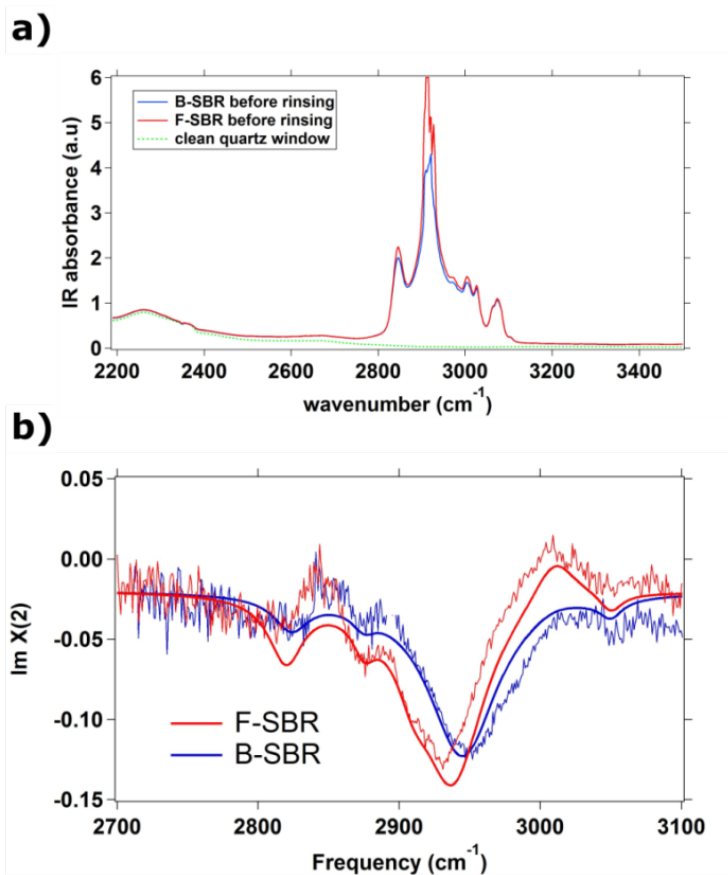
Figure 4-8. (a) FTIR spectra of clean silica window (green) and drop cast B-SBR (blue) and F-SBR (red) films on clean silica windows. Each of the presented spectra was averaged over 3 different spectra from 3 different locations on the each sample. (b) Im $\chi^{(2)}$ as a function of frequency obtained from the fitting (smooth traces) and MEM method for F-SBR and B-SBR. The fitting parameters are provided in Table 4-1.

Table 4-1. Fitting parameters for the CH stretch region and possible assignments of the bands based on other SFG work.[142,144,163,164] Phases are in radians, while frequencies and widths are in cm^{-1}.

Parameter		B_SBR	F_SBR
Nonresonant	amplitude	0.04	0.04
	phase	-0.5	-0.5
CH$_2$ symmetric stretch	amplitude	0.3	0.6
	frequency	2823	2823
	width	30	30
CH$_3$ symmetric stretch	amplitude	0.1	0.2
	frequency	2875	2875
	width	20	20
Si-CH$_3$ symmetric stretch, CH$_2$ asymmetric stretch, or CH$_2$ Fermi resonance	amplitude	0.11	0.42
	frequency	2910	2910
	width	30	30
Si-CH$_3$ asymmetric stretch, CH$_3$ asymmetric stretch, or CH$_3$ Fermi resonance	amplitude	2.7	3.2
	frequency	2945	2940
	width	55	55
CH stretch from C=C	amplitude	-0.2	-0.6
	frequency	3010	3010
	width	20	20
CH stretch from C=C	amplitude	0.11	0.12
	frequency	3050	3050
	width	20	20
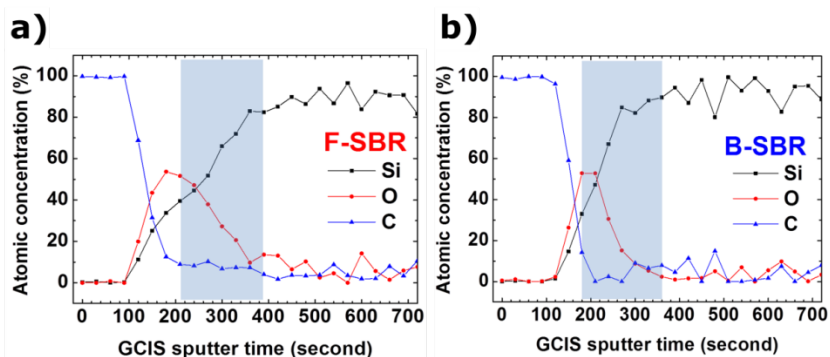
Figure 4-9. Atomic concentration (%) changes of Si, O and C at different etching time during Ar cluster sputtering of spin coated (A) F-SBR and (B) B-SBR on Si wafers. Blue highlighted regions in both graphs showing the etching period for collection of HR XPS data from the polymer film-Si wafer interfaces that are presented in Figure 4-5.
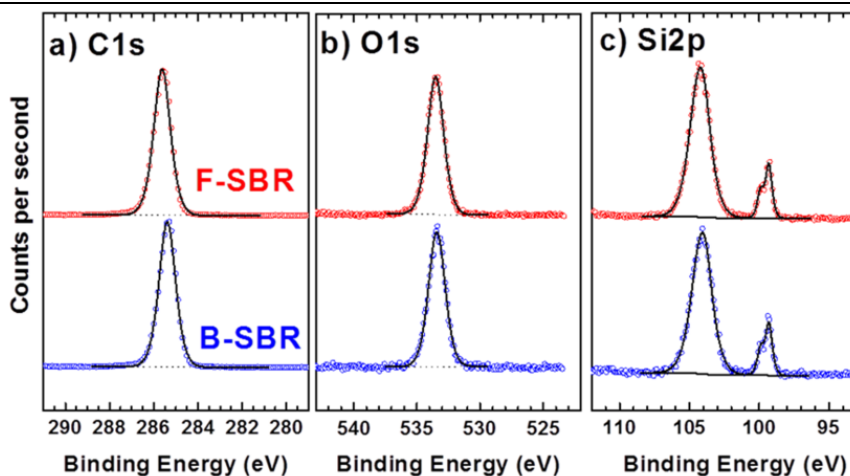
Figure 4-10. C 1s, O 1s and Si2p XPS spectra of F-SBR and B-SBR samples taken from bulk polymer films (before sputtering the films away) and presented with red and blue circles, respectively.
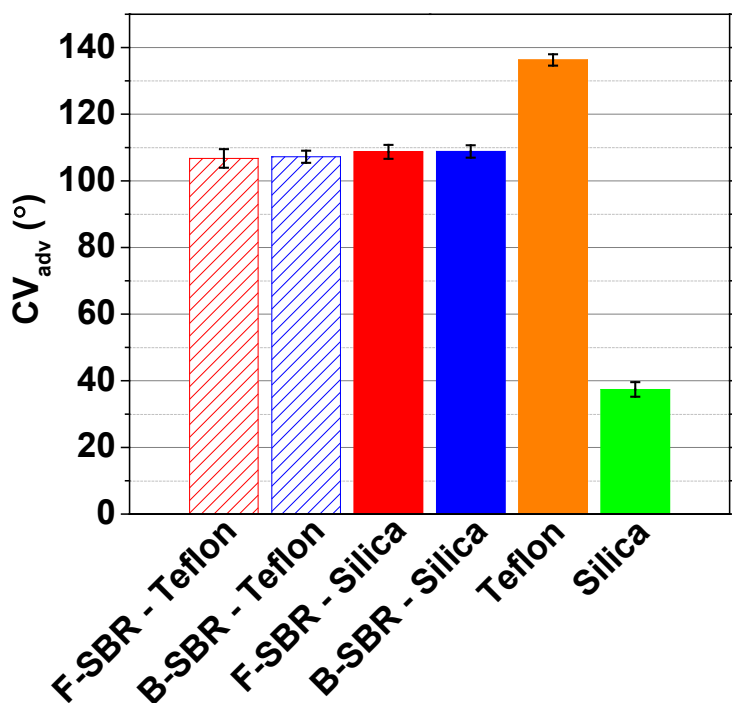
Figure 4-11. Advancing contact angle (CA) of F-SBR (red) and B-SBR (blue) on Teflon and silica window surfaces shown by patterned and solid columns, respectively. As references, CA results of clean Teflon (orange) and silica (green) windows. No significant differences ($p < 0.05$, 1-way ANOVA with Tukey's) of the CA were found between any polymer samples. Error bars indicate the standard deviation.

CHAPTER 5: RELATION BETWEEN STRAIN HARDENING AND POLYMER CHAIN ALIGNMENT

5.1   Abstract

Polymer nanocomposites – a polymer matrix blended with nanoparticles – strengthen under sufficiently large strains. Such strain hardening is critical to their function, especially for materials that bear large cyclic loads such as car tires or bearing sealants. While the reinforcement (i.e. the increase in the linear elasticity) by the addition of filler particles is phenomenologically understood, considerably less is known about strain hardening (the nonlinear elasticity). Here, we elucidate the molecular origin of strain hardening using uniaxial tensile loading, micro-spectroscopy of polymer chain alignment, and theory. The strain-hardening modulus and chain alignment are found to depend on the volume fraction, but not the size of nanofillers. This contrasts with reinforcement, which depends on both volume fraction and size of nanofillers, allowing linear and nonlinear elasticity of nanocomposites to be tuned independently.

5.2   Introduction

Many synthetic and natural materials around us increase their elastic modulus upon large deformation; a phenomenon that is known as work or *strain hardening*, which is critical to their function. In ductile polymer materials, the strain-hardening behaviour is essential for their functional lifetime, resilience, and toughness – all key parameters of their practical uses – because these materials repetitively bear large loads.[170,171] Many industrial and consumer polymeric materials are composites, in which (hard) nanoscale inorganic particles, or fillers, are blended with polymer matrices to tailor their mechanical properties. In preparing such nanocomposites, filler-filler and filler-matrix interaction, filler dispersion, and polymer properties all affect the linear (mechanical reinforcement) and nonlinear (strain softening and strain hardening) mechanical response in nontrivial ways.[10]

Chapter 5

While a massive volume of work has attempted to clarify the mechanism of reinforcement (increased linear elasticity) at low strain and of nonlinear strain softening (the Payne and Mullins effects) at medium strain, a comparatively much smaller body of work exists that focuses on the mechanism of strain hardening in polymer composite materials.

In analogy to rubber elasticity, strain hardening in polymer composites is typically attributed to the resistance to deformation of extended and oriented polymer chains. [3,5,87,172] However, it has been shown that polymer chain alignment during strain hardening is strongly affected by dispersing fillers within the host polymer matrix.[173–175] To account for these observations, one needs to establish the relation between the macroscopically observed strain hardening and the microscopic chain alignment that is affected by the presence of fillers.

The connection between chain alignment and strain hardening in glassy polymer composites is purported to occur because the fillers act as "entanglement attractors". In this picture, the segmental mobility of the polymer is disturbed (e.g. strongly constrained) by the presence of a large amount of surface area of the nanofillers, causing an increase in the number of physical entanglements. This results in greater alignment of effectively shorter segments between entanglement points in response to the applied load.[173,176] Consistent with this idea, Jancar *et al*. showed that encapsulating micron-sized fillers in poly (methyl methacrylate) (PMMA) had negligible effect on the strain-hardening properties of the PMMA matrix as opposed to the inclusion of the same volume fraction of nanofillers, which induced substantial strain hardening.[173] This suggests a clear role for both filler size and amount on strain hardening. However, because of the high glass transition temperature (T_g) for PMMA, simultaneous measurement of chain alignment was not possible in these experiments. Measuring chain alignment as a function of deformation in real-time is possible in elastomer-based nanocomposites, which have a T_g well below room temperature. This allows investigation of the effect of nanofiller size and volume fraction on strain hardening and chain alignment simultaneously; previous studies have focused on either mechanical strain hardening[177–180] or chain alignment,[70,181–183] but not both.

We investigate the strain-hardening mechanics and chain alignment in cross-linked, uniaxially loaded acrylonitrile butadiene rubber (NBR) nanocomposites (T_g ~ -30 **°C**) containing different amounts and sizes of SiO_2 nanofillers. Filler aggregate dispersion in different composites was imaged using

transmission electron microscopy (TEM). Strain hardening was quantified by the strain-hardening or neo-Hookean modulus (G_p), measured in uniaxial tensile tests.[4,184] Combined with polarized Raman micro-spectroscopy measurements of chain alignment *during* uniaxial deformation, we find that G_p is directly proportional to chain alignment and both depend on filler volume fraction, but are surprisingly independent of filler size and morphology. Using a simple scaling argument, we show that the observed chain alignment is dominated by "bridging" chains between filler aggregates. We find that chain alignment is independent of filler size because of a coupling between inter-filler spacing (related to bridging chain alignment) and volume fraction of fillers (related to total amount of bridging chains that become aligned). This demonstrates a clear distinction between the origin of nonlinear strain hardening (for which we find the nanofiller size to be irrelevant) and linear reinforcement (for which nanofiller size is important)[123] for nanocomposite-materials.

5.3   Materials & methods

Nanocomposite formulations and dipole moments of the rubbers

SiO_2 (primary particle sizes, R_p are ca. 15 nm, 20 nm and 28 nm) / Acrylonitrile Butadiene Rubber (NBR) nanocomposites were produced at SKF Elgin, USA.[1] NBR composites include 3, 8.2, 14, 22.5 vol. % fillers inside. Besides of the volume and R_p of the fillers, all the other synthetic parameters were kept the same (see Chapter 2 for details).

Electron Microscopy Imaging and Image Processing

Transmission electron microscope (TEM) imaging were done after sectioning the nanocomposites to a thickness of ca. 50 nm by ultracryotome (see Chapter 2 for details). In similar cryo condition and equipment, nanocomposites were cut to 10 μm thick sections for scanning electron microscope (SEM) imaging. All the presented electron microscope micrographs were captured at a constant magnification (5000X). TEM images were obtained with constant electron beam intensity, acceleration voltage of 120 kV and by operating a JEOL electron microscope. The magnification was set to 5000X, and images were acquired with constant electron beam intensity and an acceleration voltage of 120 kV on a LEO 1530 Gemini microscope (Leo Electron Microscopy Ltd., Zeiss, Oberkochen, Germany). Prior to the SEM imaging of the nanocomposites under stretching, 10

µm thick sections were stretched to ε_{Eng} = 1.5 and fixed on the silicon wafer with the help of a super glue (Loctite, 528).

For TEM (8-bit images), the following image processing routine was used to find the average aggregate size (R_{agg}) of nanocomposites. More than 4000 aggregates were imaged per sample from different regions of at least two sections from each composite formulation. Image analyses of electron microscope micrographs were done by using a thresholding routine in ImageJ to differentiate silica from the background polymer and obtain an area (in μm^2) for each individual aggregate. Details of the thresholding steps of TEM images are explained at length in Chapter 2. Aggregate areas for each composite are shown in Appendix III (Figure 5-6), and the cumulative distribution function of each histogram (red dashed curves in Figure 5-6) is also shown. The characteristic aggregate area was determined by discarding those aggregates in the 90th – 100th percentile of the histogram and performing a weighted average of the remaining samples. R_{agg} was then calculated assuming a circular shape.

For stretched samples measured with scanning electron microscopy (8-bit) images, ImageJ also used to process the images; however the threshold parameters were set differently than for TEM. The threshold was set to 105 and the circularity were used between 0.1 – 1.0. Starting the circularity from 0.1 helped us to avoid of counting highly charged areas around the voids in stretched samples as aggregate. For these images, all the aggregates averaged and R_{agg} was calculated assuming a circular shape.

Mechanical measurements and mechanical statistics
Uniaxial tensile measurements of nanocomposites were done by using an Instron Universal Testing Machine (Instron 6022, Darmstadt). Samples were cut into a dumbbell shape (length ≈ 1 cm, thickness ≈ 0.2 cm, width ≈ 0.18 cm) and they were clamped to the tensile testing device by applying 5 bar of clamping pressure. No pre-strain was applied and strain rate was kept 100 mm/sec for each measurement. Mechanical tests were stopped manually after the fracture of the composite. Three different stress (σ)- strain (ε) measurements were performed from each type of nanocomposite in order to have statistically consistent mechanical results. The engineering (or nominal) stress (σ_{Eng}) – engineering strain (ε_{Eng}) curves of different NBR formulations were derived after mechanical tests of the composites by following equations,

$$\sigma_{Eng} = P \ (applied \ load)/A_0(initial \ cross-sectional \ area))$$

$$\varepsilon_{Eng} = \Delta l \ (change\ in\ lenght)/l_0 (initial\ lenght)$$

To the best of our knowledge, we can assume that the volume of the composites are constant during the deformation, and thus have *Poisson's ratio* of 0.5.[5] In constant volume, true stress (σ_{True}) – true strain (ε_{True}) curves of all the nanocomposite samples were calculated using following equations,

$$\sigma_{True} = \sigma_{Eng}(\varepsilon_{Eng} + 1)$$
$$\varepsilon_{True} = \ln(\varepsilon_{Eng} + 1)$$

Anisotropy measurements by Raman Micro-spectroscopy

All the nanocomposite samples were sectioned in ca. 15 μm thicknesses by using low profile diamond blade (C.L. Sturkey Inc., Lebanon, USA) in a cryotome device (cryostat – MTC, Slee medical, Mainz, Germany) at -27 °C. These thin films were then glued on stretching brass pieces of a house –build tensile device by using super glue (Loctite 528). The gap distance between these brass blocks can be changed with in sub-micron steps by mounting a motorized actuator (THORLABS Z825B, New Jersey, USA) to the tool and this distance between gaps used for defining the strain levels (see Appendix III, Figure 5-16). Strain rate and acceleration were kept 0.025 mm/sec and 0.025 mm/sec2, respectively, for all the stretching steps between polarized Raman measurements.

At each strain level, Raman spectra of the samples were recorded with an uRaman module having a 633 nm excitation (TechnoSpex) using a (50X, 0.75 NA, Olympus). Samples at different draw ratios were placed under the constant polarized incident Raman laser with ~ 40 mW power. The angle between the drawing direction and the polarization direction was changed by rotating the sample (0° and 90°) and no analyser were placed before the detector. From each polarization angle and level of stretching, we recorded at least 6 different spectra from at least 3 different slices from each composite. Each spectrum was measured with an integration time of 24 sec.

Statistics

In order to discuss the statistical differences of the R_{agg} between different nanocomposites and G_p, we performed ANOVA package in IgorPro by using the Tukey test. Differences were considered significant when ($p<0.05$).

For S_{mol} Tukey and Student Newman-Keuls tests (SNK) were performed using IgorPro for all samples. We used ANOVA and tested the significance in S_{mol} at

each strain compared to the same sample at S_{mol} at ε=0. The value was considered statistically different when we observed a significant difference from both tests.

Significant differences between the linear slopes of S_{mol} (C≡N) data between 0 and 1.5 strain levels of different SiO_2 / NBR samples were tested by following steps. First, all measured S_{mol} data for a given sample (not only averages) was fit with a line in Igor Pro from ε = 0 until ε = 1.5 with the intercept locked to the mean S_{mol} at ε=0. In order to compare two different slopes from two different samples we assume that all the slopes follow t distribution (2-tailed).

$$t = \frac{b_1 - b_2}{\sqrt{s_{b1}^2 + s_{b2}^2}}$$

Where b_1 and b_2 refer to the slopes of the S_{mol} from sample 1 and sample 2, respectively. s_b^2 values show the standard errors of these slopes. b and s_b values were obtained as the results of the linear fitting in IgorPro. t-value then compared to the critical value of the t-distribution of cumulative distribution function in literature[97] by using $v = n_1 + n_2 - 4$ degrees of freedom. n show the total number of S_{mol} values between 0 and 1.5 strain levels. The significance between sample 1 and sample 2 is decided by finding the probability, p value in the distribution function table and statistical significance of the slopes is confirmed if $p<0.05$ according to 2-tailed t-test.[97]

5.4 Results and Discussion

5.4.1 Nanocomposite morphology

It was shown previously that the linear viscoelastic properties (reinforcement) of elastomer composite materials scaled with both the amount *and* size of dispersed nano- and microfillers for numerous elastomer polymer composites.[123] Here, we focus on elastomer nanocomposites made from acrylonitrile butadiene rubber (NBR, M_w = 250000 g/mol) loaded with various amounts (quantified as the volume fraction, Φ) and sizes (R_p) of silica (SiO_2) nanofillers. The nanocomposites are produced by melt processing and mixing (see Materials & Methods). Figure 5-1a shows the basic formulation of the nanocomposites studied here, which contain NBR (green) and one of the two different primary particle sizes (R_p) fillers (blue). All nanocomposites are vulcanized (cross-linked) (Figure 5-1a, black dotted lines). Importantly, no additional coating or coupling agents are used in these composites

to modulate filler-NBR interaction so that the composite system is as simple as possible.
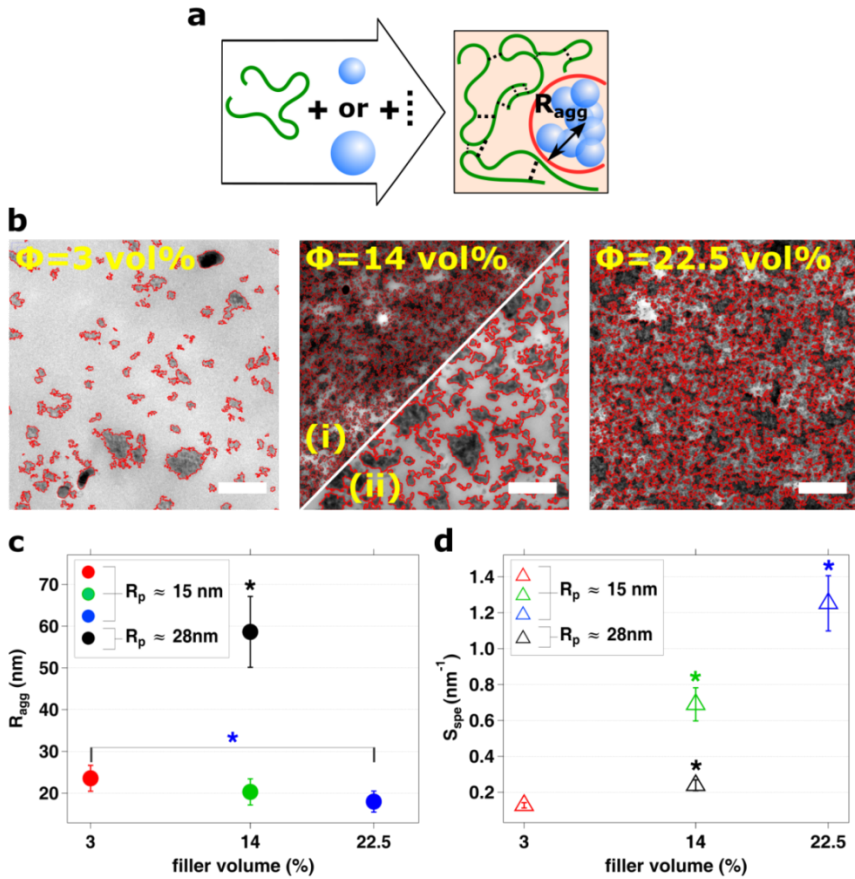
Figure 5-1. Formulation and ultrastructural characterization of nanocomposite materials. (a) Main ingredients and final microstructure of the SiO_2 / NBR nanocomposites are illustrated. Green curved line and black dashed line represents NBR molecule and sulfur cross-links, respectively. The two different sized blue balls represent the largest and smallest size nanofillers. (b) TEM images after image analysis of SiO_2 / NBR composites with different volume fraction (Φ) and primary particle size (R_p) of fillers. (i) and (ii) in the centre image both have Φ = 14%, with smallest (R_p = 15 nm) and largest (R_p = 28 nm) particles, respectively. Scale bars are 1µm. (c) Average aggregate sizes (R_{agg}) and (d) specific surface area (S_{spe}) of these samples computed by image analysis. Error bars are standard error of mean (s.e.m.) from at least 4000 aggregates from each nanocomposite. Asterisks present the significant differences ($p < 0.05$) of R_{agg} and S_{spe} (1-way ANOVA with Tukey's tests).

Chapter 5

Figure 5-1b shows transmission electron microscope (TEM) images of ultracryotomed sections of the four different nanocomposite formulations studied in this work. Light and dark contrast regions in micrographs show the elastomeric matrix and silica aggregates, respectively. Image analysis of TEM micrographs was used to quantify the filler aggregate size (R_{agg}) and dispersion[185]. Aggregate outlines are depicted by red borders in each micrograph shown in Figure 5-1b. From left to right, composites contain increasing Φ with Φ = 3%, 14%, and 22.5%, respectively. The two images with Φ = 14% contain different R_p (15 and 28 nm) whereas all other images contain R_p = 15 nm. Histograms of all detected aggregates from each nanocomposite are shown in Figure 5-6. Because a normal (Gaussian) distribution does not accurately fit these histograms, we used a weighted average over the histogram for those events that comprised 90% of the detected aggregate areas to calculate a mean aggregate size, R_{agg} (see Methods). This reduces the influence of aggregate outliers with very low abundance on R_{agg}.

Figure 5-1c show values for R_{agg} of each composite. With R_p = 15 nm, R_{agg} = 20 ± 3 nm (mean ± standard error of the mean) for Φ = 14% and 22.5% and R_{agg} increases slightly to 23.5 ± 3 nm for Φ = 3%. At Φ = 14% and R_p = 28 nm, R_{agg} = 59 ± 8.5 nm. A straightforward metric to evaluate Φ and R_{agg} simultaneously is the specific surface area ($S_{spe}=\Phi/R_{agg}$) (Figure 5-1d). Interestingly, samples with low concentrations of small particles (Φ = 3%, R_p = 15 nm) and higher concentrations of large particles (Φ = 14% R_p = 28 nm) resulted in composites with similar S_{spe}. Therefore, this sample set allows us to independently investigate the impact of filler volume fraction and filler size on the strain-hardening behavior of real industrial nanomaterials.

5.4.2   Strain hardening characteristics

We quantified the effect of filler size and Φ on strain hardening of the nanocomposites using tensile tests. True stress (σ_{True}) – true strain (ε_{True}) curves of NBR composites, are shown in Figure 5-2a. Engineering stress (σ_{eng}) and strain (ε_{eng}) curves are shown as Figure 5-7 for reference. The curves in Figure 5-2a end abruptly because of composite fracture. All composites showed strain hardening at large strains (and showed no evidence of necking). Immediately obvious from Figure 5-2a is the increased strain hardening at lower strain levels for increasing Φ. Interestingly, the curves with both sizes of fillers with Φ =14% appear

indistinguishable. Moreover, the strain hardening curves for neat NBR and for the composite with Φ = 3% also closely overlay.

In order to quantify the strain hardening for the data presented in Figure 5-2a, we calculated the strain hardening modulus, G_p. This modulus, also known as the neo-Hookean modulus derived by Mooney,[186] was used by Hawards and Thackray[187] to model cross-linked polymer composite networks as a nonlinear (rubbery) spring in parallel with a Eyring dashpot (fillers), and another Hookean spring (fillers). [177,178,188–190] In this model, randomly cross-linked (vulcanized) NBR chains create a network made up of freely joined chains, which are entropic springs that stiffen under volume conserving extension leading to[3,4]:

$$\sigma_{True} = G_p \left(\lambda^2 - \frac{1}{\lambda} \right), \text{where } \lambda$$
$$= \varepsilon_{Eng} + 1 \text{ and } G_p \text{ is the strain hardening modulus.}$$

This relation allows one to effectively quantify the linear and nonlinear behaviour simultaneously with G_p due to the scaling of $\left(\lambda^2 - \frac{1}{\lambda} \right)$ under the assumption of Gaussian chain statistics. Figure 5-2b shows Gaussian (or neo-Hookean) plots of each NBR systems until their fracture points. Since each of the composites fractured at different strain, we focus on the region from ε_{eng} = 0 - 2.9 (0 - 14.95 in the Gaussian plots) as this is the maximum strain all composites could sustain (Figure 5-2b, red box). This region is shown highlighted in Figure 5-2c. Comparing G_p from different samples for the different nanocomposites, we mark statistically significant differences ($p < 0.05$) between each pair of composites by grey boxes in the box chart (inset, Figure 5-2c). Consistent with data in Figure 5-2b, G_p is statistically identical for both samples with Φ = 14% and for neat NBR and Φ = 3%. Figure 5-2d further shows the trend that G_p increases linearly with Φ, independent of filler size, for a variety of NBR nanocomposite formulations. Statistical testing of G_p in many different NBR samples confirmed the finding that G_p varied only with Φ and was independent of filler size (Figure 5-9), which is contrary to reinforcement in the same samples.
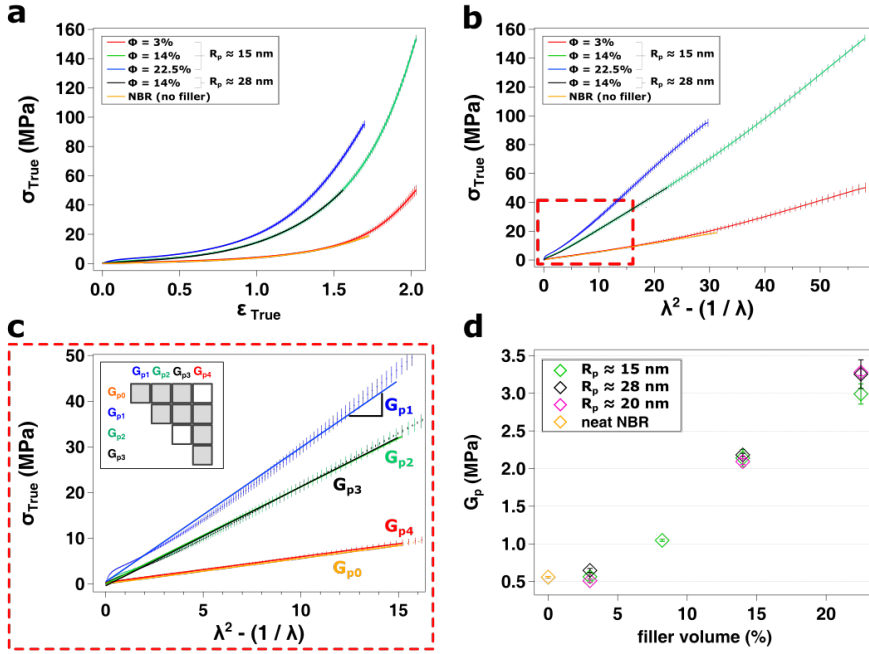
Figure 5-2. Strain-hardening characteristics of nanocomposites. (a) True stress (σ_{True}) − true strain (ε_{True}) curves of SiO$_2$ / NBR nanocomposites with different filler volume and size. σ_{True} - ε_{True} of the unfilled (vulcanized) NBR is shown by the orange curve. (b) Gaussian plots of σ_{True} as a function of (λ^2-1/ λ) of all the NBR systems. (c) Zoom into the red box shown in (b) presenting the G_p of each sample between the region where ε_{eng} is between 0 and 2.9. Inset is a box chart where statistically significant differences ($p < 0.05$) between G_p of each pair of composites is denoted by a grey box (2 tailed t-test). (d) G_p derived from Gaussian plots of many NBR nanocomposites containing different Φ and R_p of fillers. Error bars are standard deviation (s.d.) of three independent measurements of three slices from the same composite slab.

5.4.3 Chain alignment in NBR nanocomposites during uniaxial stretching

We used *in situ* vibrational spectroscopy to measure molecular chain alignment during uniaxial tension application using polarized Raman micro-spectroscopy. In our measurements, the sample was rotated such that the Raman excitation laser was polarized parallel or perpendicular to the loading direction at each strain level (ε_{eng}), and all Raman scattered light was detected; there was no polarizer in front of the detector as we were uninterested in depolarization ratios. Raman spectra at

each ε_{eng} were recorded as $A_{\parallel}$ or $A_{\perp}$, depending on whether the laser polarization was parallel or perpendicular to the stretching direction, respectively. We calculated the $\langle P_2 \rangle$ coefficient from these amplitudes and refer to this coefficient as the molecular order parameter, $S_{mol} = \frac{A_{\parallel} - A_{\perp}}{A_{\parallel} + 2 A_{\perp}}$.[181,191] S_{mol} is zero for a perfectly isotropic vibration. For a perfectly anisotropic vibrational mode of a molecular group aligned parallel or orthogonal to the loading direction S_{mol} is 1 or -0.5, respectively. In the case of stretching vibrations, such as the C≡N or C=C stretches, the polarizability changes as nuclei move along the bond axis, so S_{mol} reflects bond orientation.

An important challenge of polarized Raman measurements is spectral normalization to account for spatial heterogeneity from different positions and for inter-sample comparison. This is critical for obtaining an accurate measurement of S_{mol} and comparing measurements within and among nanocomposites. We verified that it was possible to use vibrational modes that exhibit no anisotropy as normalizing vibrations with measurements in amorphous polystyrene as a reference. Our results for anisotropy in polystyrene after normalizing background-subtracted spectra by the CH_3 rocking vibration (1033 cm^{-1}) corresponded very well with previous studies using infrared dichroism (Figure 5-11).[192–195] Therefore, we employed a similar normalization protocol for NBR samples. We observed that the CH_2 twisting (tw) vibration (1300 cm^{-1}) showed no anisotropy in strained NBR spectra, and thus the CH_2 tw peak was used as an independent peak for normalization of $A_{\parallel}$ and $A_{\perp}$ in all NBR spectra.

We focus on the C=C stretch (1666 cm^{-1}) from the *trans*-1,4-butadiene monomer (marked by letter k in Figure 5-3a)[83,196] and C≡N stretch (2235 cm^{-1}) vibrations in NBR to anisotropy and chain alignment. The C=C backbone and C≡N sidechain group will align (somewhat) parallel and perpendicular to the loading direction, respectively, as chain alignment increases (Figure 5-3 (a) and (b)). Figure 5-3b, shows S_{mol} for both vibrations. As expected, we find that S_{mol} (C=C) became more positive and S_{mol} (C≡N) became more negative with increasing ε_{eng} for all nanocomposite samples. The top and bottom orange boxes in Figure 5-3b and 3c mark the maximum standard error of the mean (s.e.m.) in S_{mol} (C=C) and S_{mol} (C≡N) from the measurements of the unfilled (but vulcanized) NBR, which never showed a statistically significant S_{mol} value at any ε_{eng} when compared to the $S_{mol} (\varepsilon_{eng} = 0\%)$.
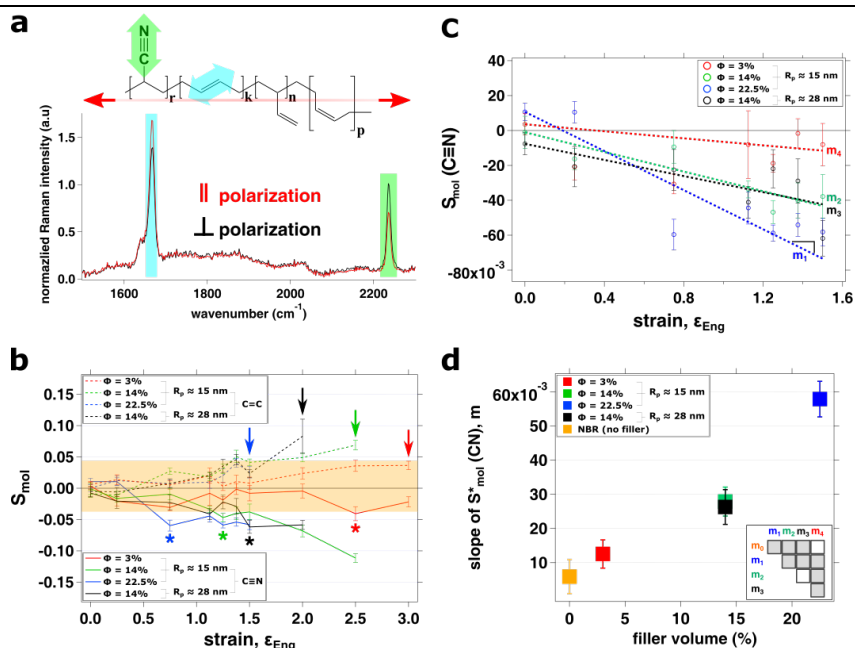
Figure 5-3. Polymer anisotropy and molecular spectroscopy of uniaxially stretched nanocomposites. (a) Molecular structure of an NBR chain aligned to the stretching direction (red line with arrows). Letters *r,k,n,* and *p* represent different monomer units in NBR (see methods). Cyan and green double-sided arrows highlight the direction of the C=C (from *trans*-1,4-butadiene) and C≡N stretching vibrations, respectively. Raman peaks corresponding to these vibrations are highlighted in the example Raman spectra of a stretched (ε_{Eng} = 2.5) nanocomposite (Φ = 14%, R_p = 15 nm). The red and black lines show spectra obtained when the Raman excitation light was parallel and perpendicular to the loading direction, respectively. (b) Vibrational anisotropy (S_{mol}) at increasing strains (ε_{eng}) in different nanocomposites with different amount and R_p fillers. S_{mol} (C=C) from *trans*-1-4 butadiene (1665 cm^{-1}) and S_{mol} (C≡N) (2235 cm^{-1}) stretching vibrations are shown with dashed and straight lines, respectively. Top and bottom orange boxes show the maximum s.e.m. of S_{mol} (C=C, top) and minimum s.e.m. of S_{mol} (C≡N, bottom), respectively, from the neat NBR data. Asterisks indicate ε_{eng} levels where the significant anisotropies ($p < 0.05$) were observed compared to unstrained samples (ε_{eng} = 0) (1-way ANOVA with Tukey's and Student Newman-Keuls tests). Colored arrows show the largest bearable ε_{eng} before fracture. (c) Linear fits to the S_{mol} (C≡N) between ε_{eng} levels of 0 and 1.5. The slope (*m*) of NBR without any filler inside (m_0) is shown in Figure 5-14. Error bars in (b) and (c) are s.e.m. from a minimum of 6 spectra (each for $A_{\parallel}$ and $A_{\perp}$ at each ε_{Eng}) from different locations from at least 3 different slices of each nanocomposite. (d) Relation between the slope values and filler amount. Inset shows, statistical differences of each pair of slopes ($p < 0.05$, t-test) in a box chart are shown by grey boxes. Error bars are s.d. from the

regression line fits presented in (c).

   In the subsequent quantification and discussion of anisotropy, we restrict our attention to the C≡N sidechain group since it is a more sensitive marker of chain alignment. This choice is substantiated by the following reasons. First, from a geometrical standpoint, a fully stretched NBR chain (Figure 5-3a) will never show purely unidirectional C=C polarizability along the bond of the *trans*-1-4 butadiene because, by definition, this bond cannot align perfectly to the loading direction. Second, the bonding geometry of C≡N is necessarily orthogonal to the (C-C bonds in the) NBR backbone due the *sp* hybridization of the carbon atom. Therefore, the alignment axes of the polymer backbone and CN stretching polarizability are nearly orthogonal, which will increase the anisotropy of this group compared to the C=C bond when a chain is aligned. Consistent with these arguments, we experimentally observed more S_{mol} (C≡N) data points appearing outside of the orange box compared to S_{mol} (C=C). We note that in addition to the C≡N sidechain, a similarly negative anisotropy was observed for CH_2 groups for the CH_2 symmetric vibration (2846 cm^{-1}), which should also lie orthogonal to the chain backbone (Figure 5-13a). Taken together, this underscores the robustness of our measurement protocol and molecular anisotropy measurements.

   In Figure 5-3b, asterisks mark the critical ε_{eng} – defined as the ε_{eng} at which we first observed a statistically significant ($p < 0.05$) increase in S_{mol} (C≡N) compared to S_{mol} (C≡N) at $\varepsilon_{eng} = 0$ for each sample. The most prominent trend observed in Figure 5-3b is that the critical ε_{eng} required to develop a statistically significant C≡N vibrational anisotropy decreased with increasing $\varPhi$. We conclude that adding more fillers (increasing $\varPhi$) causes NBR chains to align to a greater extent for a given deformation. For the two nanocomposites with $\varPhi = 14$ %, we observed a critical ε_{eng} that was slightly lower for the composite with smaller R_{agg} (Figure 5-3b, green) compared to that with increased R_{agg} (Figure 5-3b, black); otherwise, the S_{mol} (C≡N) vs. ε_{eng} traces look extremely similar.

   As a method to compare the trends in Figure 5-3b, we linearly fit the S_{mol} (C≡N) vs. ε_{eng} for each composite from $\varepsilon_{eng} = 0$ until $\varepsilon_{eng} = 1.5$ (Figure 5-3c). This range was chosen because $\varepsilon_{eng} = 1.5$ was the highest ε_{eng} from which we were able to collect Raman data from all samples. The slope of each fit, $m = (\Delta S_{mol}) / (\Delta \varepsilon_{eng})$, is a measure for how increasing ε_{eng} induces C≡N anisotropy, and therefore chain alignment, in the composites. Figure 5-3d shows that m increases with $\varPhi$, and the results from statistical comparison of m from different samples are summarized in the inset; significant differences between two slopes ($p < 0.05$) are

shown by grey boxes. All slopes were statistically independent except for those from the composites with Φ = 14%, which again confirms that volume fraction, but not filler size, affects chain alignment.
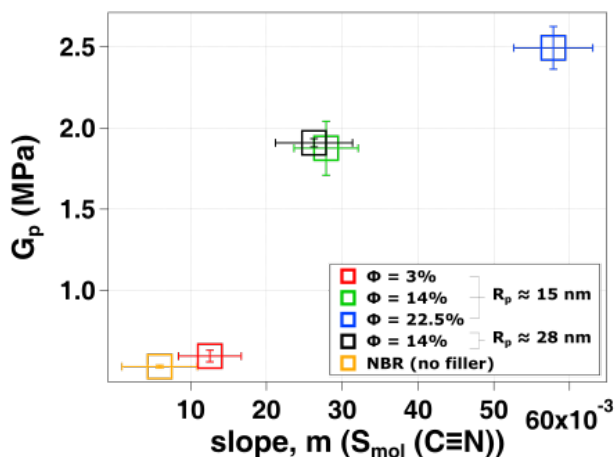
Figure 5-4. Correlation between strain hardening and chain anisotropy in nanocomposites. Graph shows relation between the $|m|$ from the chain alignment measurements (Figure 5-3d) and the strain-hardening modulus (G_p, Figure 5-2c) of all samples. Error bars of G_p are s.d (n = 3) and slopes, m are s.d. obtained from the linear regression line fits.

Since the slope in anisotropy, m, and Gp both vary with Φ, we plotted these variables against one another in Figure 5-4. This graph clearly shows that these variables are positively correlated, indicating that strain hardening can be predicted by chain alignment and vice versa in our nanocomposites. Previous work has shown that filler size strongly affects reinforcement[123] and strain hardening in semi-crystalline composites;[173] it is therefore surprising that filler size has almost no effect on chain alignment or strain hardening.

5.4.4   Modelling chain anisotropy in strained nanocomposites

To further interpret the chain alignment experiments, we developed a model for how chain alignment develops under strain and is affected by filler properties. As a starting point, we consider three types of NBR chains in a nanocomposite (Figure 5-5a): Type 1) chains that are wrapped around (bound to) the fillers, Type 2) chains that exist within the polymer bulk and not in the vicinity of fillers, and Type 3)

chains that exist within space between two fillers – referred to as "bridging" chains. Type 1 chains will necessarily have C≡N side groups that are radially symmetric and will therefore not contribute to S_{mol} (C≡N). From our measurements in unfilled, vulcanized NBR, we empirically found that Type 2 chains generate no detectable anisotropy of C≡N bonds (Figure 5-14). This leaves Type 3 bridging chains as the primary contributor to our measured C≡N anisotropy.

We assume that each Type 3 chain contributes a certain amount of Raman signal to $A_\perp$ and $A_\parallel$ – the C≡N vibration Raman intensities acquired orthogonal and parallel to the loading direction – such that $1 = A_\parallel + A_\perp$. In the simplest meaningful assumption that each chain has N monomers, each with a size a, we can write $A_\perp \sim \frac{L}{Na}$, where L parameterizes the space between fillers. This relation states that the Raman amplitude for C≡N vibrations in a Type 3 chain in the direction orthogonal to the loading direction scales proportionally with distance between fillers and inversely with chain length, which follows intuition for bridging chains. However, $A_\perp$ must be constrained because when L is greater than Na (the contour length of the chain), the anisotropy should no longer increase, and we impose this constraint by writing $A_\perp \sim \tanh\frac{2L}{Na}$. The space between fillers $L \sim L_o(1 + \varepsilon_{eng})$, where L_0 is the space between fillers in the unstrained composite, and we assume affine deformation (see Figure 5-8). We calculate L_0 using a conservation of volume argument as $L_0 \sim R_{agg}\left[\frac{1-\Phi}{\Phi}\right]^3$, where Φ is volume fraction and R_{agg} is the characteristic filler (aggregate) radius from Figure 5-1. A schematic for the model is shown in Figure 5-5a.

With this model defined, we calculated S_{mol} for a single Type 3 chain (S_{mol}^{chain}) and by multiplying this value by N_3 such Type 3 chains in the focal volume, we arrive at the total S_{mol} value, which has the form,

$$S_{mol} = N_3 \cdot S_{mol}^{chain} = N_3 \cdot \frac{1 - 2\tanh\frac{2L}{Na}}{1 + \tanh\frac{2L}{Na}}$$

From our measured aggregate size and fitted lines in Figure 5-3c, we calculated N_3 and S_{mol}^{chain} as function of ε_{eng}, assuming Na = 120 nm for an NBR chain with a molecular weight of 250000 g/mol. There are no other free parameters in this calculation. This model allows us to investigate the mechanism of increasing S_{mol} (C≡N) with ε for the different composites with respect to individual chain anisotropy and number of total contributing Type 3 chains.

Our calculations showed that N_3 and $\left|S_{mol}^{chain}\right|$ increase with ε for all systems and that N_3 was largest at largest Φ whereas $\left|S_{mol}^{chain}\right|$ was smallest at

largest Φ (Figure 5-5b). Interestingly, at Φ = 14%, we observed that N_3 was larger with smaller R_{agg} (because there are comparatively more bridging chains for greater S_{spe}), whereas $\left|S_{mol}^{chain}\right|$ was larger with larger R_{agg} (because of the larger L_0 between aggregates). Since the total signal is proportional to the product $N_3 \cdot S_{mol}^{chain}$, this model reveals that these two effects must compensate one another.

Figure 5-5c shows nanocomposite ultrastructure at ε_{eng} = 1.5 based on our model and experimental chain alignment data. Unfilled NBR (orange box, Figure 5-5c) only has Type 2 (green) chains due to the absence of fillers. Weak anisotropy could in principle originate from Type 2 chains, but this was undetectable in our spectroscopic measurements. In the presence of the lowest volume fraction fillers (Φ = 3%), Type 3 (red) chains begin to weakly contribute to the measured S_{mol}. Because Φ is relatively low, $L_o \sim Na$ (the contour length of a chain), and the anisotropy of Type 3 *bridging chains* ($\left|S_{mol}^{chain}\right|$) is quite large. However, because Φ = 3%, very few bridging chains exist, i.e. N_3 is small, and the measured S_{mol} is barely detectable.

Samples with Φ = 14% are shown in the black and green boxes in Figure 5-5c for the samples with large and small R_{agg}, respectively. Larger R_{agg} increases L_o, leading to larger $\left|S_{mol}^{chain}\right|$. However, the nanocomposite with smaller R_{agg} has smaller L_o due to larger S_{spe}, which increases the number of the bridging chains (N_3) in the same volume relative to the sample with larger R_{agg}. These two effects cancel out, resulting in the same S_{mol} for both samples. When Φ = 22.5% (blue box in Figure 5-4c), L_o and $\left|S_{mol}^{chain}\right|$ are smallest of all measured nanocomposites, but the number of bridging chains (N_3) is largest since the aggregates are most densely packed (and have the largest S_{spe}), leading to the largest measured chain alignment. These ultrastructure schematics illustrate the compensatory nature between bridging chain alignment and number that vary in opposite ways with respect to surface-to-surface distance of the filler aggregates.

Figure 5-5. Modeling chain alignment in nanocomposites. (a) Illustration showing the three different type of NBR in a typical nanocomposite structure for our scaling theory at low strain (left) and high strain (right). Type 1 (black) and Type 2 (green) chains represent filler-adsorbed and bulk rubber, respectively. Type 3 (red) chains bridge the filler aggregates to each other parallel to the stretching direction and are called "bridging" chains. Other possibilities of bridging chains which are called Type 4 (dark grey) chains, bridge the fillers orthogonally to the loading direction. The bridging region is indicated by the red box with dashed line showing. Under strain Type 1 chains delaminate from particles, enter the bridging region, and convert to Type 3 chains. (b) Graph showing calculated S_{mol}^{chain} (C≡N bonds, dashed lines) and number of Type 3 chains (N_3, solid lines) as a function of ε_{eng} based on the scaling argument presented in the text. S_{mol}^{chain} decreases (becomes more negative) and N_3 increases with ε_{eng}. (c) Schematic illustrations of the predicted ultrastructural features in nanocomposites at ε_{eng} = 1.5. Ultrastructure of neat NBR is illustrated in the orange box. Microstructures sketched in red, green and blue boxes represent the composites including small fillers ($R_p \approx$ 15 nm) at Φ = 3%, 14% and 22.5%, respectively. Microstructure in black is for Φ = 14% with the larger filler particles ($R_p \approx$ 28 nm). Color codes of different types of polymer chains (Type 1, Type 2, and Type3) are the same as those in (a). The L_o and R_{agg} represented in each illustration are scaled realistically, under the assumption that aggregates are perfectly distributed in a cubic lattice.

5.4.5 Relation between NBR anisotropy and strain-hardening modulus

Our work shows how strain hardening and strain-induced chain alignment are strongly correlated and vary with Φ alone, independent of nanofiller ultrastructure. Within the context of our model, the mechanism underlying how increasing ε increases $\left|S_{mol}^{chain}\right|$ and N_3, thereby increasing S_{mol} follows the forthcoming logic. I) L increases with strain, increasing $\left|S_{mol}^{chain}\right|$ until it reaches a maximum (-0.5), and II) conversion of Type 1 chains into Type 3 chains via shear-induced delamination of Type 1 chains from the filler surface (Figure 5-5a, red dotted boxes). Conversion of "slippery" adsorbed (Type 1) chains into Type 3 chains has been shown, specifically in samples (nearly identical to ours) where limited interaction between the polymer and fillers is present.[182,197] While it is, in principle, possible to disrupt filler aggregates with increasing tensile strain, which would have a similar effect as delamination, scanning electron micrograph images of 150% strained nanocomposite samples show no such effects (Figure 5-15).

Recalling again the results of Jancar *et al*. where PMMA microcomposites showed almost no strain hardening compared to nanocomposites at the same Φ, this raises an interesting question. Over what length scale do Type 3 chains exist, and therefore contribute tangible chain alignment, in composite systems? Looking at our data from unfilled and Φ = 3% nanocomposites, we conjecture that detectable chain alignment only occurs when $L_o \sim Na$. In microcomposites, $L_o \sim \mu m$ ($\gg Na$ of the PMMA), whereas $L_o \sim Na$ in nanocomposites. Therefore, the microcomposite case approaches that of a vanishingly low Φ in nanocomposites, where almost no Type 3 chains exist, which results in minimal chain alignment and therefore minimal strain hardening.

5.5 Conclusions

The effect of nanofiller size and amount on non-linear strain hardening of cross-linked elastomers ($T_g \sim$ -30 °C) was quantified here for various NBR nanocomposites. By measuring both their mechanical strain hardening and chain alignment with increasing tensile strain, we show that both the strain-hardening modulus and chain alignment in NBR composites only depend on filler amount and were independent of the filler size. Furthermore, these two variables were

positively correlated highlighting the relation between them. Using a simple scaling argument, we arrive at a mechanism for chain alignment that only depends on filler volume fraction via a compensatory effect between individual chain alignment and number of (bridging) chains aligning to the load. While our work highlights the importance of chains bridging filler aggregates over a length scale comparable with the contour length of a chain, Baeza *et al*. recently related the complex linear elasticity in nanocomposites to network formation among overlapping tightly bound chains in close proximity (~ nm) to filler surfaces.[198] Along with our results showing that nonlinear elasticity of nanocomposites is insensitive to filler size, this underscores the different physico-chemical origin of the linear and nonlinear elasticity in these materials. This suggests that nanocomposite design can be optimized in a two-tiered process wherein one tunes the strain hardening properties and mechanical reinforcement independently by: 1) choosing an amount of nanofillers to target a specific nonlinear strain hardening response and 2) selecting a particular size of nanofillers to obtain a desired reinforcement.

5.6   Appendix III

Thermal analysis

Differential scanning calorimetry (DSC) measurements were done by operating a DSC 822 (Mettler Toledo) under nitrogen in order to calculate glass-transition temperature (T_g) of nanocomposites and rubber samples with and without vulcanization. ~ 10 mg from each sample placed in sample pans, and DSC curves were obtained after three cycles of measurements between -100°C and +200 °C with a temperature rate of 10 K min^{-1}.

Raman micro-spectroscopy measurement of polystyrene

Polystyrene (PS) slides ((T_g ≈ 100 °C, 1 mm x 25 mm x 75 mm), Nalge Nunc™ Int., Rochester, NY, USA) were first fixed in our stretching stage using clamps. The stage was then placed on top of a heating plate, and the temperature was monitored with a thermo-couple in contact with the PS surface. When the temperature of the PS slide reached to ~ 120 °C and was stable, the PS slide was stretched to the desired strain. Immediately after stretching, the film was immersed in ice water mixture for one minute. After drying, polarized Raman spectra of stretched PS films were recorded using the same measurement parameters as used for the nanocomposites.
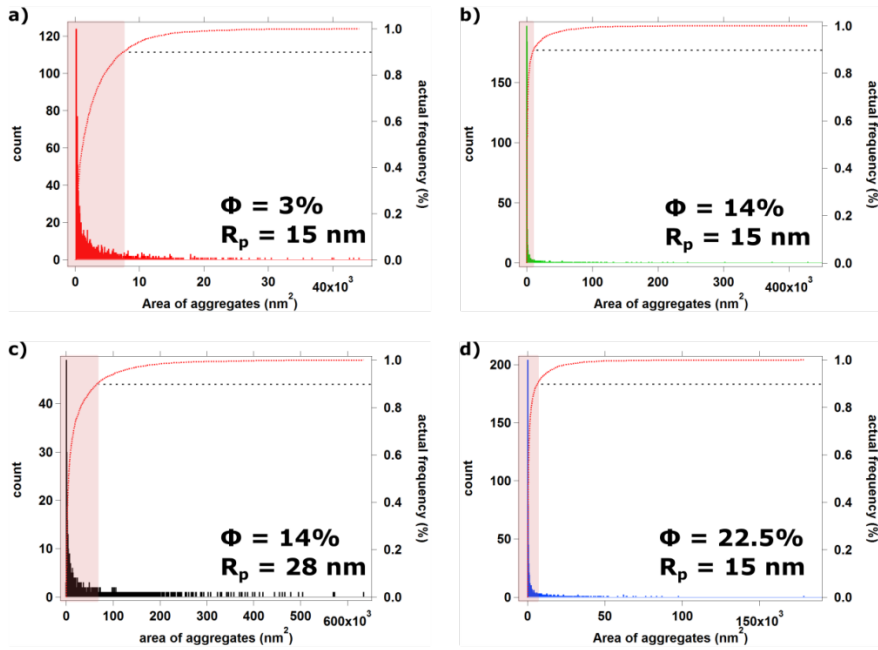
Supporting figures

Figure 5-6. Histograms showing aggregate area sizes in different NBR nanocomposites including various nanofiller particle sizes (R_p) and volume (Φ). Cumulative distribution functions derived from each of these histograms are shown from 0% frequency until 100% frequency (right y-axis) by red dashed lines. Black dashed lines mark the 90th percentile of aggregates, and all aggregates from 0-90th percentile, denoted by the bars in the shaded area (red) in each histogram, were used to calculate the average aggregate area. The 90th -100th percentile in the cumulative distribution functions were discarded.
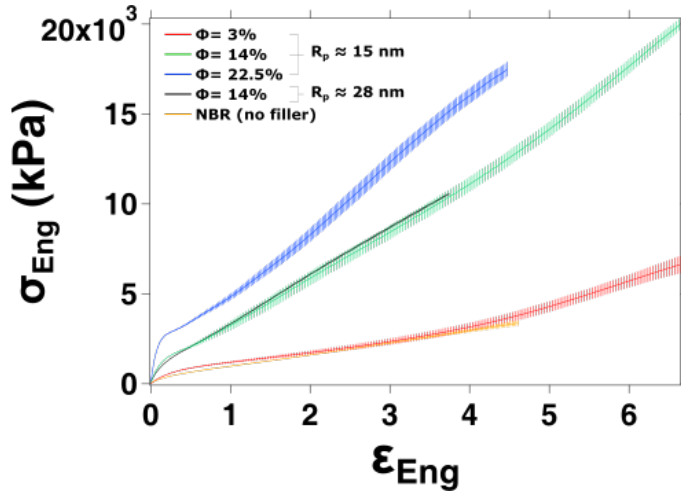
Figure 5-7. Engineering stress (σ_{Eng}) – engineering strain (ε_{Eng}) curves of neat NBR and NBR nanocomposites including different amount and size of fillers. Error bars are standard deviation (s.d.) from measurements of three slices from the same composite slab.
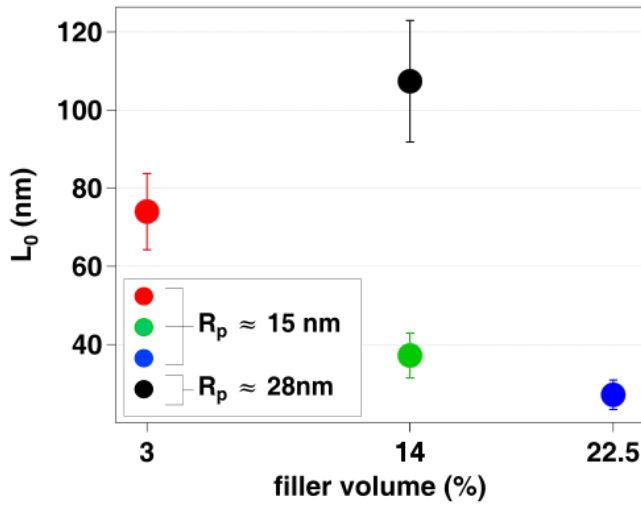

Figure 5-8. Surface-to-surface distance, $L_0 \sim R_{agg}\left[\frac{1-\Phi}{\Phi}\right]^3$ between aggregates in different NBR nanocomposites. In the formula, R_{agg} is the average aggregate size and Φ is the filler volume. Error bars are derived from standard error of the mean (s.e.m.) of the aggregate size distribution.
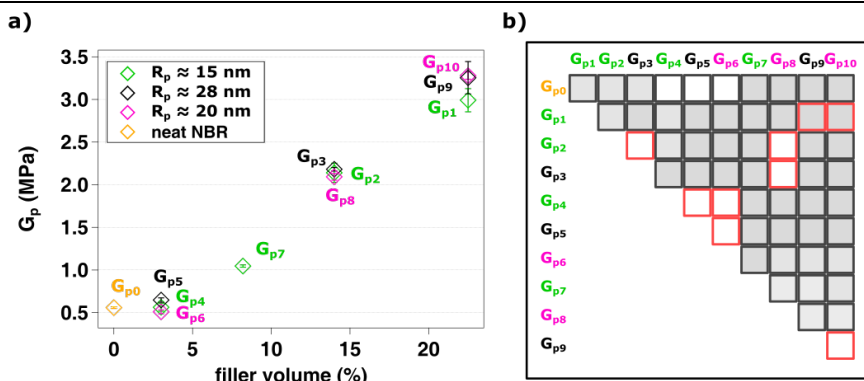
Figure 5-9. (a) Strain hardening modulus (G_p) of all the NBR nanocomposites and neat NBR derived from Gaussian plots as explained in the main text (Figure 5-2). G_p of each sample is labelled using different number and colors. (b) Box chart showing the significant differences ($p < 0.05$) between each pair of G_p by grey filled boxes (1-way ANOVA with Tukey's). Error bars in a are s.d. from measurements of three slices from the same composite slab.
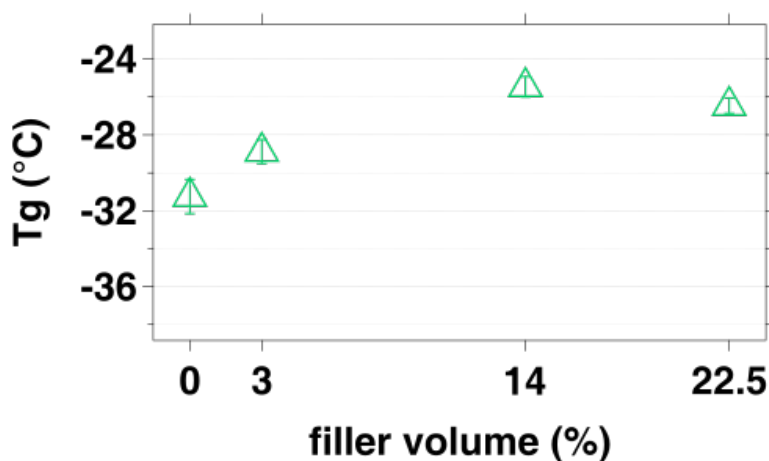

Figure 5-10. Glass transition temperature (T_g) of neat NBR and NBR nanocomposites including different amount but the same size ($R_p \approx 15$ nm) of fillers. Error bars are s.d. from 3 heating cycles on a single sample from each formulation.
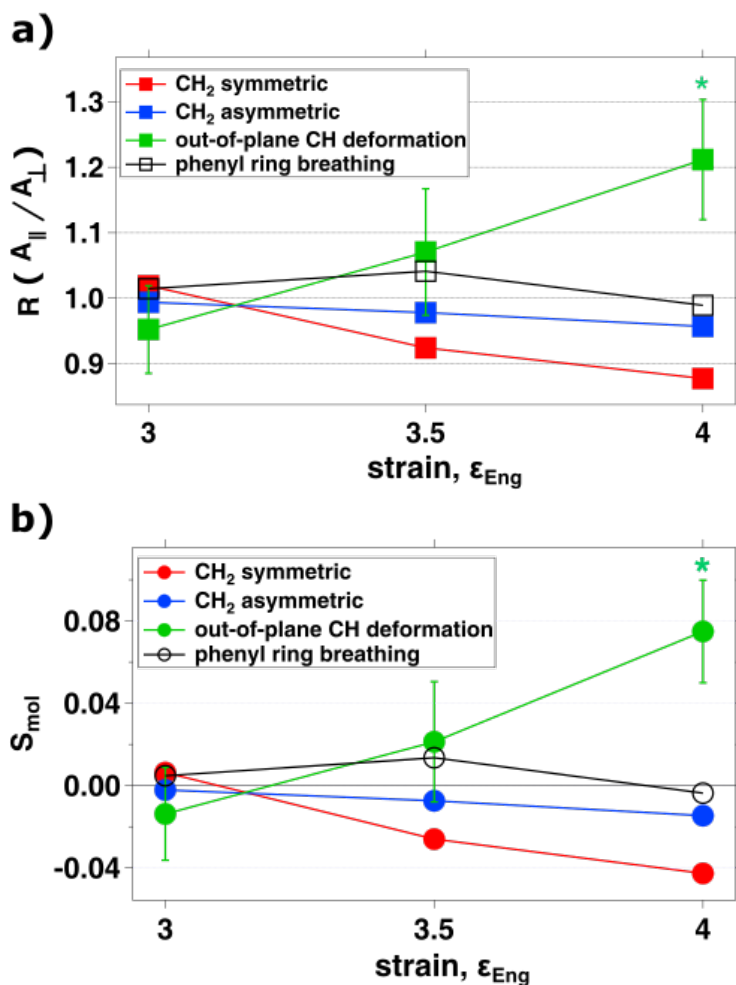
Figure 5-11. Anisotropy of polystyrene (PS) film at increasing engineering strain (ε_{Eng}) shown as (a) dichroic ratio, R, which was obtained from the ratio of the indicated Raman peak intensities in normalized Raman spectra (normalization peak is CH_3 rocking, 1033 cm^{-1}). $R = A_{||} / A_{\perp}$ where $A_{||}$ was the normalized Raman intensity when the stretching direction and excitation laser were parallel and $A_{\perp}$ was the normalized Raman intensity when the stretching direction and excitation laser were perpendicular. (b) Anisotropy of PS vibrations shown by S_{mol} (as in the main text). Significant anisotropy ($p < 0.05$) compared to the R and S_{mol} of PS film at $\varepsilon_{Eng} = 0$ is indicated by using asterisk (1-way ANOVA with Tukey's and Student Newman-Keuls tests). Error bars in both plots bars are s.e.m. from measurements three different sections from the same PS slide that were stressed to the indicated value.
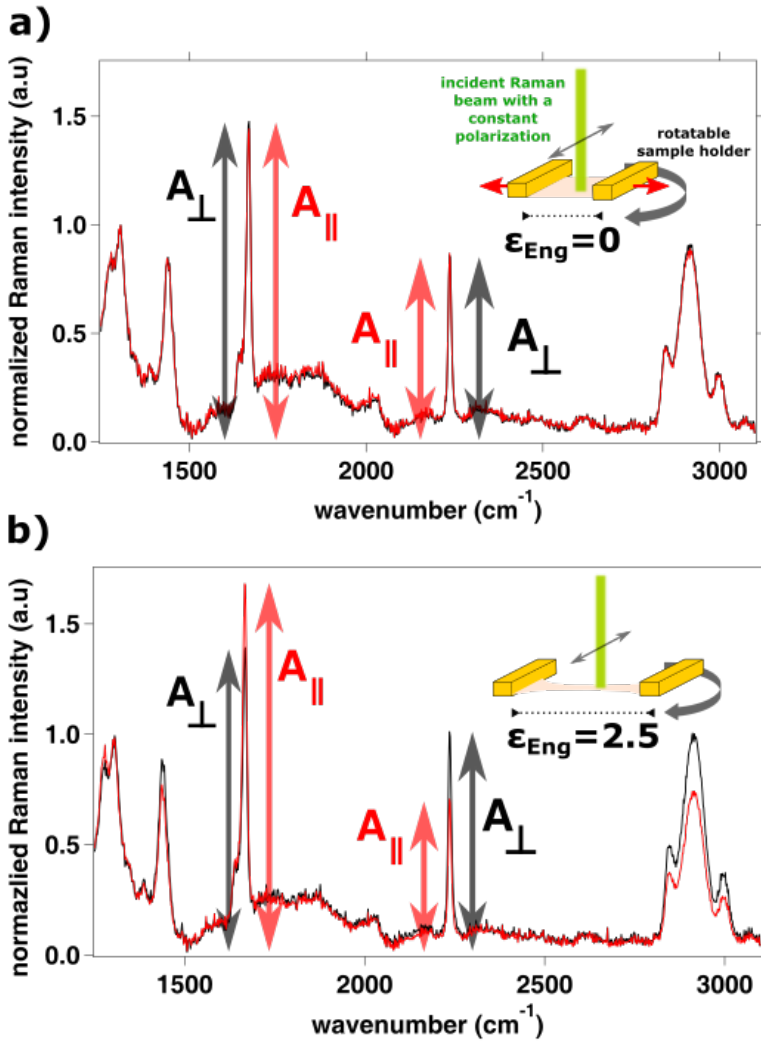
Figure 5-12. (a) Normalized Raman spectra of NBR nanocomposite (Φ = 14% and R_p = 15 nm) at (a) ε_{Eng} = 0 and (b) ε_{Eng} = 2.5 measured with the excitation laser polarization parallel (red) and perpendicular (black) to the loading direction. Insets illustrate the experimental laser polarization (double-headed arrow) and geometry of polarized Raman measurements. In (a) and (b), amplitude of characteristic Raman peaks are shown by red and black arrows next to the characteristic peaks of C=C (1666 cm^{-1}) and C≡N (2235 cm^{-1}).
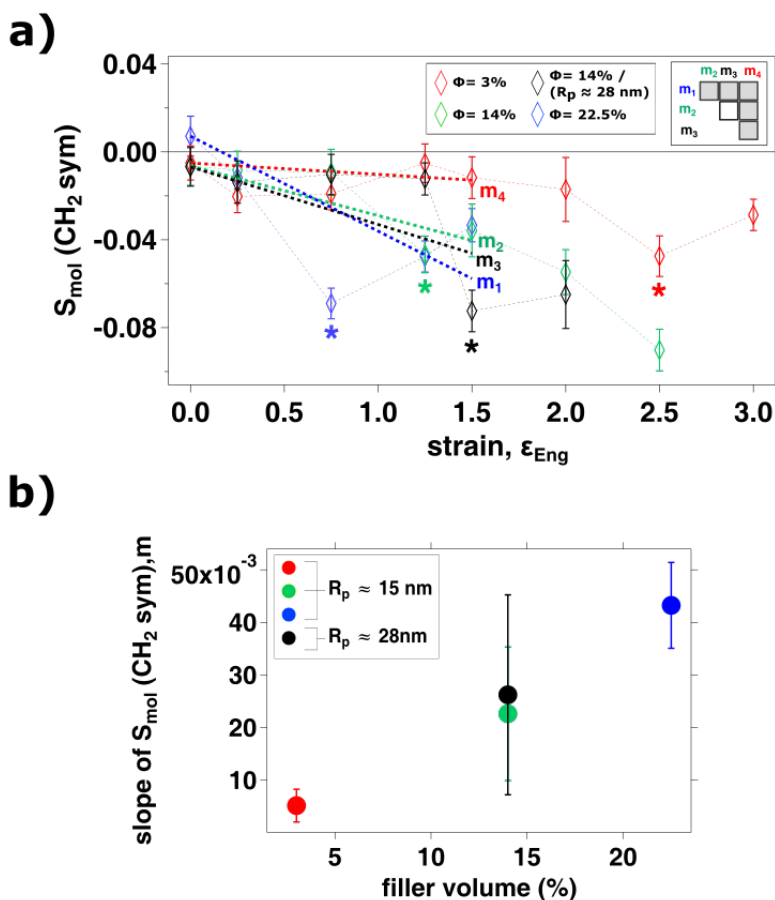
Figure 5-13. (a) S_{mol} (CH$_2$ sym, 2846 cm^{-1}, see Figure 5-12) in NBR composites with increasing strain. Asterisks shows the first significant S_{mol} change compared to the S_{mol} at relaxed state. Dashed lines represents the linear fit of S_{mol} (CH$_2$ sym) of different samples between relaxed state and ε_{Eng} = 1.5. Statistical comparison (t-test) summary of these slopes are shown in the box chart as an inset. Filled boxes represent the significant difference ($p < 0.05$) between two regression lines (slopes). (b) The slope amplitudes shown versus filler volume. Error bars in (a) are s.e.m. from a minimum of 6 spectra (each for A_∥ and A_⊥ at each ε_{Eng}) from different locations from at least 3 different slices of each nanocomposite. Error bars in (b) are s.d. from the linear fitting.
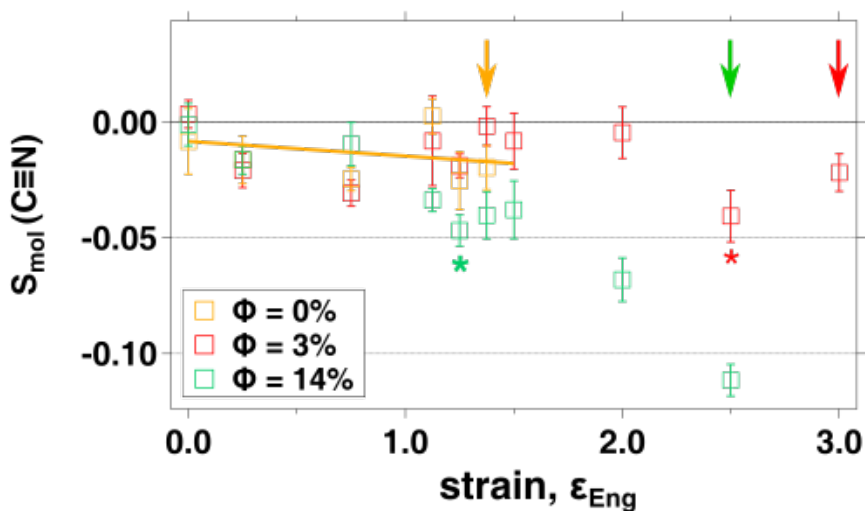
Figure 5-14. S_{mol} (C≡N) from neat NBR (Φ = 0%) and NBR nanocomposites including Φ = 3% and Φ = 14% fillers (R_p ≈ 15 nm) inside at increasing strain. The largest strain before fracture is shown by different color arrows for each sample. Error bars in (a) are s.e.m. from a minimum of 6 spectra (each for $A_\parallel$ and $A_\perp$ at each ε_{Eng}) from different locations from at least 3 different slices of each nanocomposite.

a)

b)

c)
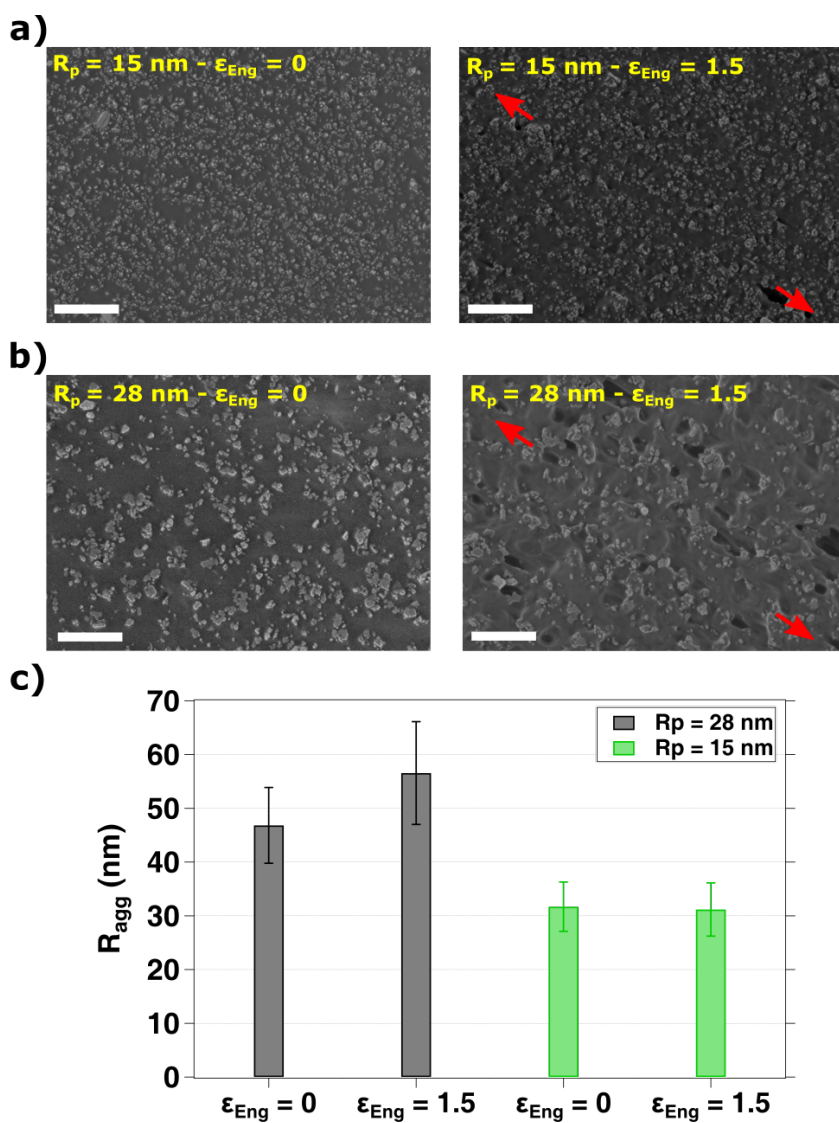
Figure 5-15. (a) Scanning electron microscope images of NBR nanocomposites (Φ = 14%) including fillers with R_p of (a) 15 nm and (b) 28 nm. In (a) and (b) images in the left and right columns were taken before (ε_{Eng} = 0) and after stretching (ε_{Eng} = 1.5), respectively. Direction of the stretching is shown by red arrows. Scale bars are 1 μm. (c) Average aggregate size (R_{agg}) of the samples shown in (a) and (b). Error bars are s.e.m. from measurements on different samples.
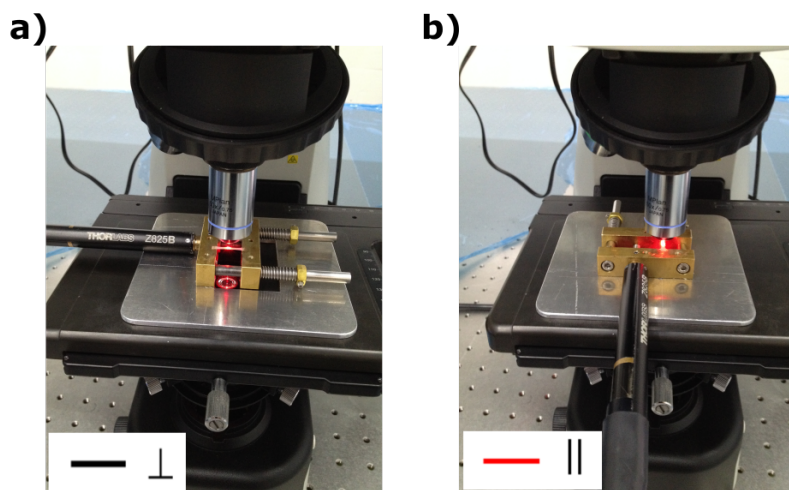
Figure 5-16. Photographic images showing our polarized Raman setup during measurement of a stretched nanocomposite sample (between the copper bars) when the angle between the incident Raman light polarization and the stretching direction is (a) perpendicular or (b) parallel.

CHAPTER 6: FUTURE DIRECTIONS

Understanding the viscoelasticity of elastomer based nanocomposites is a very challenging task. Herein, I tried to see the nanocomposites during their linear and non-linear deformations from a molecular point of view. Even though the research presented here answer some crucial questions about mechanics of nanocomposites in terms of molecular structure of elastomers network during deformation and the effect of nanofiller dispersion, still many of questions about the magic behind viscoelasticity of nanocomposites remain unanswered. Limited variability in nanocomposite chemistry is one of the drawbacks of my project preventing me to find more universal answers to important questions. Next to increasing the variety of nanocomposites, also my methods which were used for explaining the reinforcement and strain-hardening of nanocomposites, should be applied for explaining different kind of deformation stages in nanocomposites, such as Payne effect, Mullins effect etc. Particularly my findings in Chapter 5 explaining strain-hardening characteristics in nanocomposites in monotonic (not repeating) stretching conditions must be reinforced by expanding the strain-hardening behavior of these samples in more real life use conditions, for instance, under cyclic deformations. Below, I will explain preliminary results of the strain-hardening behavior of NBR nanocomposites under cyclic forces.

6.1 Strain-hardening of nanocomposites under cyclic forces

During their production and practical uses, elastomer-based nanocomposites need to fulfill some important criteria, such as optimum processability, toughness, fatigue life etc., which have not been discussed in thesis. Among these factors, cyclability directly defines the life-time of some nanocomposites in practical applications. For instance, car tires during rolling undergo cyclic loading and the life-time of the tire tread under such deformation has been related to nano- to micro- size void transitions in the rubber.[199,200] In these studies, the dispersion of carbon black or other carbon allotropies (e.g., multi-wall carbon nanotube, MWCNT) has proven to have a positive effect on the life-time of the rubber under

cyclic forces. This improvement is related to morphological changes of MWCNT fillers under cyclic deformations and the strong interaction between fillers and surrounding rubber matrix. Another recent study has elucidated the strain-hardening enhancement of material under cyclic loading due to the presence of uniformly dispersed Fe_3O_4 nanofillers having physical cross-links with elastomer.[177] In the studied system, under cyclic stretching Fe_3O_4 nanoparticles align along the direction of deformation and this alignment increases the total resistance of the composite to further deformations to the same direction. In our study, as mentioned before, there is no significant attraction between silica nano-fillers and matrix, fillers are not perfectly dispersed and the strain hardening modulus changes due to filler amount is explained in terms of "bridging rubber" alignment to the stretching direction (see Chapter 5). However, as it is shown in Figure 6-1, under uniaxial stretching of an NBR nanocomposite ($\Phi = 22.5$) sample at different cycles of stretching, we observed some interesting variations on the elasticity.
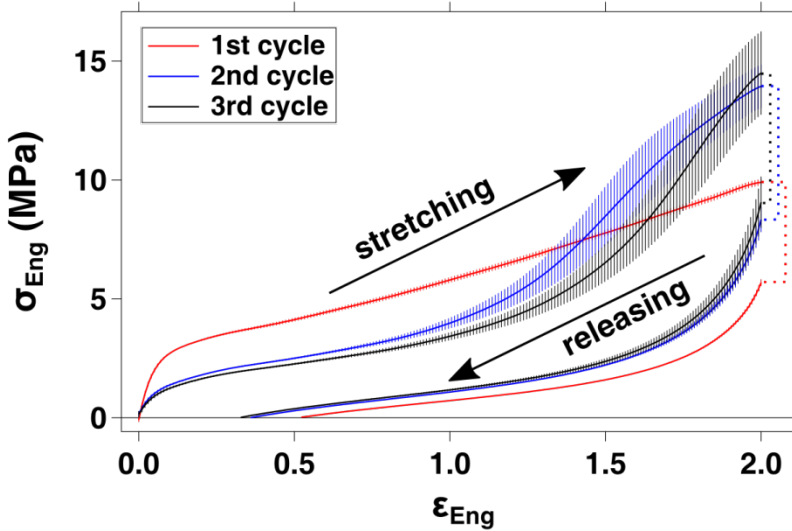
Figure 6-1. Engineering stress (σ_{Eng}) – engineering strain (ε_{Eng}) characteristics under cyclic (3 cycles) loadings of SiO_2 (Φ=22.5) / NBR nanocomposite. Curves under the arrow labelled as 'releasing' present σ_{Eng} - ε_{Eng} curves of the sample during stress release till σ_{Eng} gets zero. Three curves between the two black arrows represent the σ_{Eng} - ε_{Eng} behavior of the sample at each stretching from ε_{Eng} = 0 till ε_{Eng} = 2. Error bars are standard deviation (SD) from 3 different dog-bone shape cut samples from the same nanocomposite slab.

For this experiment, I first cut three dog bone shape (length ≈ 1 cm, thickness ≈ 0.2 cm, width ≈ 0.18 cm) tensile test specimen from the slab of the highest volume filled NBR nanocomposite (Φ = 22.5). This sample is particularly interesting among all the other NBR systems (see Methods), since it has the most prominent strain-hardening characteristics at high strain levels in monotonic tensile tests discussed in Chapter 5. Each dog-bone shape sample is clamped (5 bar pressure) and stretched from ε_{Eng} = 0 till ε_{Eng} = 2 with the strain rate of 100 mm/min. During the cyclic mechanical tests, samples were held at ε_{Eng} = 0 and ε_{Eng} = 2 constantly for 2 minutes (dashed lines in Figure 6-1), in which we could stabilize the initial stress relaxation of the samples. Releasing (unstretching) the stress is carried out till the stress on the sample returns to zero (σ_{Eng} = 0) with a constant strain rate of 50 mm/min. Before each stretching cycle, the initial stress level was tuned to zero by changing slightly the initial gap distance between clamps. First, second and third stretching cycles in the $\sigma_{Eng} - \varepsilon_{Eng}$ figure in Figure 6-1 are presented by using red, blue and black colors, respectively. In Figure 6-1, curves lies between the black arrows labelled as 'stretching' and 'releasing' present the $\sigma_{Eng} - \varepsilon_{Eng}$ curves of stretching at different cycles. The $\sigma_{Eng} - \varepsilon_{Eng}$ characteristics changing during unstretching (releasing) are shown under the black arrow labelled as 'releasing'.

In Figure 6-2a, the $\sigma_{True} - \varepsilon_{True}$ derived from $\sigma_{Eng} - \varepsilon_{Eng}$ stretching curves in Figure 6-1. Even without a quantitative analysis, it is apparent from the stretching curves from both $\sigma_{Eng} - \varepsilon_{Eng}$ and $\sigma_{True} - \varepsilon_{True}$, that there is a clear effect of different cycles of stretching on the linear (initial slope of the curves at very low strain levels) and non-linear elasticity of the nanocomposite. Similar to previous studies aimed at obtaining the strain-hardening modulus, G_p at different number of cycles,[87,177,178,188] we also quantified G_p (see Chapter 5) of our sample with the help of linear fits to Gaussian plot at very high strains where there are almost linear correlations. Therefore, we did our linear fits to each slope in Figure 6-2b and (c) between $\lambda^2 - (1/\lambda)$ values of 6 (ε_{True} = 0.93, ε_{Eng} = 2.53) and 8.66 (ε_{True} = 1.1, ε_{Eng} = 3) which is shown with a red box with dashed line in Figure 6-2b. The quantities of the slopes in each Gaussian curves (linear fits in Figure 6-2c) derived from different cyclic loadings is presented in Figure 6-2d. We have clearly observed that the strain-hardening modulus, G_p of the sample increases after each cycle of loading. On the top of this, this positive correlation between cycle of loading and G_p looks linear.
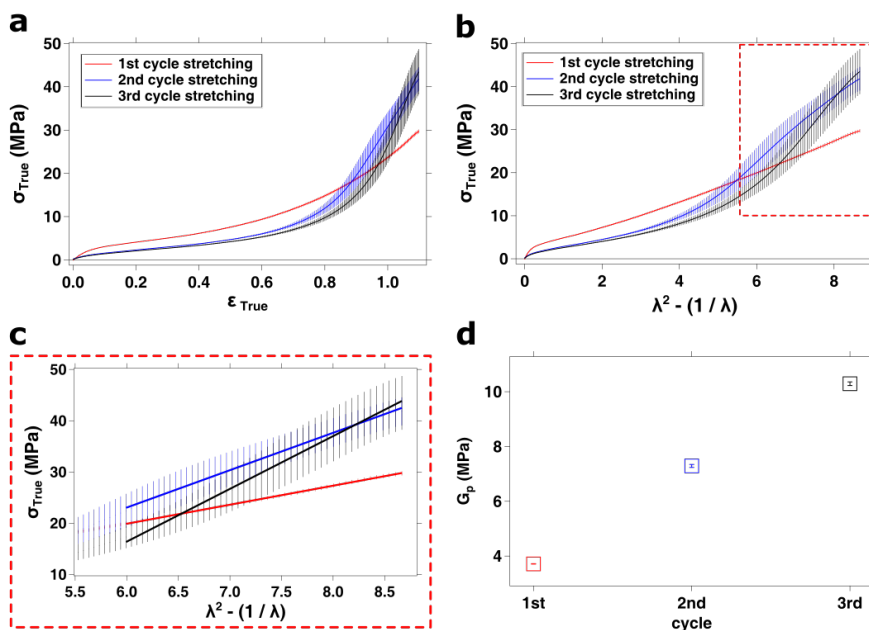
Figure 6-2. (a) True stress (σ_{True}) – true strain (ε_{True}) curves of SiO$_2$ (Φ = 22.5) / NBR nanocomposite at increasing number of stretching. (b) The Gaussian plots of the samples presented in (a). Red box sketched with dashed line represents the data range used for finding the slopes of each Gaussian curve at high strain levels. (c) Zoom in to the panel (b) is presented by showing the linear fits whose amplitude gives us the Gp presented in (d). Error bars are SD from three different dog-bone shape cut of the NBR system.

In the aforementioned literature, the "magic" behind the increase of G_p with increasing number of cycles has been explained in terms of inorganic filler alignment and enhanced interaction between fillers and surrounding rubber with each cycle.[177,178,188] In our systems, we do not have any significant chemical or physical interaction between filler and NBR and the morphology (shape) of fillers does not change with stretching (see Chapter 5). However, interestingly, in our systems we observe a clear hardening mechanism related to the number of loading cycles similar to the results on literature.

For the next steps of this preliminary work, we will repeat the cyclic mechanical tests for other NBR nanocomposites introduced in Chapter 5 and check their NBR chain anisotropy at each cycle. Performing the cyclic loading experiments of other nanocomposites will show us if this G_p and number of cycle relation is correlated also to the filler amount and/or filler size. And polarized Raman

experiments of the samples under cyclic forces might shed a light on the behavior of the "bridging chains" under cyclic deformations. One might naively guess that, previously mentioned delamination behavior of type -1 bound chains from filler surface and join to the type-3 ("bridging chains") might be the key factor of obtaining higher G_p with increasing number of loading cycle. However, such hand-waving explanations must be validated in the near future by previously mentioned experiments to achieve a better understanding of the enhanced strain-hardening of the NBR nanocomposites with increasing numbers of stretching cycles.

BIBLIOGRAPHY

[1]   J.G. de Castro, R. Zargar, M. Habibi, S.H. Varol, S.H. Parekh, B. Hosseinkhani, M. Adda-Bedia, D. Bonn, Nonmonotonic fracture behavior of polymer nanocomposites, Appl. Phys. Lett. 106 (2015) 221904. doi:10.1063/1.4922287.

[2]   S.A. Jensen, Z. Mics, I. Ivanov, H.S. Varol, D. Turchinovich, F.H.L. Koppens, M. Bonn, K.-J. Tielrooij, Competing Ultrafast Energy Relaxation Pathways in Photoexcited Graphene, Nano Lett. (2014) 1–14. doi:10.1021/nl502740g.

[3]   E. Riande, R. Diaz-Calledja, M.G. Prolongo, R.M. Masegosa, C. Salom, Polymer Viscoelasticity: Stress and Strain in Practice, Marcel Dekker AG, New York and Basel, 2000.

[4]   L.R.. Treloar, The Physics of Rubber Elasticity, Oxford University Press, Oxford, 1975.

[5]   J.R. Fried, Polymer Science and Technology, Prentice Hall, NJ, 2003.

[6]   A. Cavallo, M. Müller, J.P. Wittmer, A. Johner, K. Binder, Single chain structure in thin polymer films: corrections to Flory's and Silberberg's hypotheses, J. Phys. Condens. Matter. 17 (2005) S1697–S1709. doi:10.1088/0953-8984/17/20/004.

[7]   F.W. Starr, T.B. Schrøder, S.C. Glotzer, Molecular Dynamics Simulation of a Polymer Melt with a Nanoscopic Particle, Macromolecules. 35 (2002) 4481–4492. doi:10.1021/ma010626p.

[8]   P. Rittigstein, J.M. Torkelson, Polymer–nanoparticle interfacial interactions in polymer nanocomposites: Confinement effects on glass transition temperature and suppression of physical aging, J. Polym. Sci. Part B Polym. Phys. 44 (2006) 2935–2943. doi:10.1002/polb.20925.

[9]   C.B. Roth, J.R. Dutcher, Glass transition and chain mobility in thin polymer films, J. Electroanal. Chem. 584 (2005) 13–22. doi:10.1016/j.jelechem.2004.03.003.

[10]   J. Jancar, J. Douglas, F. Starr, Current issues in research on structure–property relationships in polymer nanocomposites, Polymer (Guildf). 51 (2010) 3321–3343. doi:10.1016/j.polymer.2010.04.074.

[11]   J. Kalfus, J. Jancar, Immobilization of polyvinylacetate macromolecules on

hydroxyapatite nanoparticles, Polymer (Guildf). 48 (2007) 3935–3937. doi:10.1016/j.polymer.2007.04.049.

[12]   S. Wolff, M.-J. Wang, E.-H. Tan, Filler-Elastomer Interactions. Part VII. Study on Bound Rubber, Rubber Chem. Technol. 66 (1993) 163–177. doi:10.5254/1.3538304.

[13]   K. Ben Azouz, E.C. Ramires, W. Van Den Fonteyne, N. El Kissi, A. Dufresne, Simple method for the melt extrusion of a cellulose nanocrystal reinforced hydrophobic polymer, ACS Macro Lett. 1 (2012) 236–240. doi:10.1021/mz2001737.

[14]   T. McNally, P. Pötschke, P. Halley, M. Murphy, D. Martin, S.E.J. Bell, G.P. Brennan, D. Bein, P. Lemoine, J.P. Quinn, Polyethylene multiwalled carbon nanotube composites, Polymer (Guildf). 46 (2005) 8222–8232. doi:10.1016/j.polymer.2005.06.094.

[15]   J. Sapkota, M. Jorfi, C. Weder, E.J. Foster, Reinforcing Poly(ethylene) with Cellulose Nanocrystals, Macromol. Rapid Commun. 35 (2014) 1747–1753.

[16]   S.S. Sternstein, A.J. Zhu, Reinforcement mechanism of nanofilled polymer melts as elucidated by nonlinear viscoelastic behavior, Macromolecules. 35 (2002) 7262–7273. doi:10.1021/ma020482u.

[17]   J. Oberdisse, Aggregation of colloidal nanoparticles in polymer matrices, Soft Matter. 2 (2006) 29. doi:10.1039/b511959f.

[18]   B.A. Jones, A. Facchetti, T.J. Marks, M.R. Wasielewski, Cyanonaphthalene Diimide Semiconductors for Air-Stable, Flexible, and Optically Transparent n-Channel Field-Effect Transistors, Chem. Mater. 19 (2007) 733–735.

[19]   K.I. Winey, R.A. Vaia, Polymer, MRS Bull. 32 (2007) 314–319.

[20]   L.S. Schadler, S.K. Kumar, B.C. Benicewicz, S.L. Lewis, S.E. Harton, D esigned Interfaces in Polymer Nanocomposites : A Fundamental Viewpoint, MRS Bull. 32 (2007) 335–340.

[21]   M. Moniruzzaman, K.I. Winey, Polymer Nanocomposites Containing Carbon Nanotubes, Macromolecules. 39 (2006) 5194–5205. doi:10.1021/ma060733p.

[22]   M.M. Rooney, D.H. Farrell, B.M. van Hemel, P.G. de Groot, S.T. Lord, The contribution of the three hypothesized integrin-binding sites in fibrinogen

to platelet-mediated clot retraction., Blood. 92 (1998) 2374–81. http://www.bloodjournal.org/content/92/7/2374.abstract.

[23]   W.A. Lam, O. Chaudhuri, A. Crow, K.D. Webster, T.-D. Li, A. Kita, J. Huang, D.A. Fletcher, Mechanics and contraction dynamics of single platelets and implications for clot stiffening., Nat. Mater. 10 (2011) 61–6. doi:10.1038/nmat2903.

[24]   M. Gerspracher, C.P. O'Farrell, Filler-filler and filler-polymer interactions as a function of in-rubber carbon black dispersion, Kautschuk Und Gummi, Kunststoffe. 51 (1998) 488–495.

[25]   R. Rauline, intentor; Michelin, assignee. Copolymer rubber composition with silica filler, tires having a base of said composition and method of preparing same. US patent 5227425. (1993, Jul 13).

[26]   W.H. Waddell, L.R. Evans, Use of Nonblack Fillers in Tire Compounds, Rubber Chem. Technol. 69 (1996) 377–423. doi:10.5254/1.3538378.

[27]   P. Akcora, S.K. Kumar, J. Moll, S. Lewis, L.S. Schadler, Y. Li, B.C. Benicewicz, A. Sandy, S. Narayanan, J. Ilavsky, P. Thiyagarajan, R.H. Colby, J.F. Douglas, "Gel-like" Mechanical Reinforcement in Polymer Nanocomposite Melts, Macromolecules. 43 (2010) 1003–1010. doi:10.1021/ma902072d.

[28]   L. Conzatti, G. Costa, M. Castellano, A. Turturro, F.M. Negroni, J.F. Gérard, Morphology and Viscoelastic Behaviour of a Silica Filled Styrene/Butadiene Random Copolymer, Macromol. Mater. Eng. 293 (2008) 178–187. doi:10.1002/mame.200700320.

[29]   C. Chevigny, F. Dalmas, E. Di Cola, D. Gigmes, D. Bertin, F. Boué, J. Jestin, Polymer-Grafted-Nanoparticles Nanocomposites: Dispersion, Grafted Chain Conformation, and Rheological Behavior, Macromolecules. 44 (2011) 122–133. doi:10.1021/ma101332s.

[30]   M. Castellano, L. Conzatti, A. Turturro, G. Costa, G. Busca, Influence of the silane modifiers on the surface thermodynamic characteristics and dispersion of the silica into elastomer compounds, J. Phys. Chem. B. 111 (2007) 4495–4502.

[31]   F. Yatsuyanagi, N. Suzuki, M. Ito, H. Kaiddu, Effects of surface chemistry of silica particles on the mechanical properties of silica filled styrene-butadiene rubber systems, J. Appl. Polym. Sci 86, 7 (2002) 1622–1629.

Bibliography

[32]   N. Jouault, F. Dalmas, F. Boué, J. Jestin, Multiscale characterization of filler
        dispersion and origins of mechanical reinforcement in model
        nanocomposites, Polymer (Guildf). 53 (2012) 761–775.
        doi:10.1016/j.polymer.2011.12.001.

[33]   J. Oberdisse, F. Boué, Rheology–structure relationship of a model
        nanocomposite material, Trends Colloid Interface Sci. XVII. (2004) 124–129.
        doi:10.1007/b94023.

[34]   G.J. Schneider, V. Vollnhals, K. Brandt, S. V Roth, D. Göritz, Correlation of
        mass fractal dimension and cluster size of silica in styrene butadiene rubber
        composites., J. Chem. Phys. 133 (2010) 94902. doi:10.1063/1.3469827.

[35]   Y. Shinohara, H. Kishimoto, N. Yagi, Y. Amemiya, Microscopic Observation
        of Aging of Silica Particles in Unvulcanized Rubber, Macromolecules. 43
        (2010) 9480–9487. doi:10.1021/ma102095b.

[36]   M. Tatou, A. Genix, A. Imaz, J. Forcada, R. Schweins, I. Grillo, J. Oberdisse,
        Reinforcement and Polymer Mobility in Silica À Latex Nanocomposites with
        Controlled Aggregation, Macromolecules. 44 (2011) 9029–9039.

[37]   A. Botti, W. Pyckhout-Hintzen, D. Richter, V. Urban, E. Straube, J.
        Kohlbrecher, Silica filled elastomers: polymer chain and filler
        characterization in the undeformed state by a SANS–SAXS approach,
        Polymer (Guildf). 44 (2003) 7505–7512.
        doi:10.1016/j.polymer.2003.09.016.

[38]   G.P. Baeza, A. Genix, C. Degrandcourt, L. Petitjean, Multiscale Filler
        Structure in Simplified Industrial Nanocomposite Silica / SBR Systems
        Studied by SAXS and TEM, Macromolecules. 46 (2013) 317–329.

[39]   G.P. Baeza, A.-C. Genix, C. Degrandcourt, J. Gummel, M. Couty, J.
        Oberdisse, Mechanism of aggregate formation in simplified industrial silica
        styrene-butadiene nanocomposites: effect of chain mass and grafting on
        rheology and structure., Soft Matter. 10 (2014) 6686–95.
        doi:10.1039/c4sm01095g.

[40]   M. Castellano, L. Conzatti, G. Costa, L. Falqui, A. Turturro, B. Valenti, F.
        Negroni, Surface modification of silica: 1. Thermodynamic aspects and
        effect on elastomer reinforcement, Polymer (Guildf). 46 (2005) 695–703.
        doi:10.1016/j.polymer.2004.11.010.

Bibliography

[41]   D. Le Strat, F. Dalmas, S. Randriamahefa, J. Jestin, V. Wintgens, Mechanical reinforcement in model elastomer nanocomposites with tuned microstructure and interactions, Polymer (Guildf). 54 (2013) 1466–1479. doi:10.1016/j.polymer.2013.01.006.

[42]   J.S. Meth, S.G. Zane, C. Chi, J.D. Londono, B.A. Wood, P. Cotts, M. Keating, W. Guise, S. Weigand, Development of Filler Structure in Colloidal Silica–Polymer Nanocomposites, Macromolecules. 44 (2011) 8301–8313. doi:10.1021/ma201714u.

[43]   S. Harms, K. Rätzke, F. Faupel, G.J. Schneider, L. Willner, D. Richter, Free Volume of Interphases in Model Nanocomposites Studied by Positron Annihilation Lifetime Spectroscopy, Macromolecules. 43 (2010) 10505–10511. doi:10.1021/ma1022692.

[44]   K. Nusser, S. Neueder, G.J. Schneider, M. Meyer, W. Pyckhout-Hintzen, L. Willner, A. Radulescu, D. Richter, Conformations of Silica–Poly(ethylene–propylene) Nanocomposites, Macromolecules. 43 (2010) 9837–9847. doi:10.1021/ma101898c.

[45]   B. Radhakrishnan, R. Ranjan, W.J. Brittain, Surface initiated polymerizations from silica nanoparticles, Soft Matter. 2 (2006) 386. doi:10.1039/b516508c.

[46]   I. In, Y. La, S. Park, P.F. Nealey, P. Gopalan, Side-Chain-Grafted Random Copolymer Brushes as Neutral Surfaces for Controlling the Orientation of Block Copolymer Microdomains in Thin Films, Langmuir. 22 (2006) 7855–7860.

[47]   G.P. Baeza, A. Genix, C. Degrandcourt, L. Petitjean, R. Schweins, M. Couty, J. Oberdisse, Effect of Grafting on Rheology and Structure of a Simpli fi ed Industrial Nanocomposite Silica/SBR, Macromolecules. 46 (2013) 6621–6633. doi:dx.doi.org/10.1021/ma401016d.

[48]   L.F. Scatena, M.G. Brown, G.L. Richmond, Water at hydrophobic surfaces: weak hydrogen bonding and strong orientation effects., Science. 292 (2001) 908–12. doi:10.1126/science.1059514.

[49]   Y.R. Shen, Surface properties probed by second-harmonic and sum-frequency generation, Nature. 337 (1989) 519–525. doi:10.1038/337519a0.

[50]   Y.R. Shen, Principles of nonlinear optics, Wiley-Interscience, NY (1984).

Bibliography

[51]   J.E. Baio, T. Weidner, J. Brison, D.J. Graham, L.J. Gamble, D.G. Castner, Amine Terminated SAMs: Investigating Why Oxygen is Present in these Films., J. Electron Spectros. Relat. Phenomena. 172 (2009) 2–8. doi:10.1016/j.elspec.2009.02.008.

[52]   J. Stöhr, NEXAFS Spectroscopy, Springer Science & Business Media, Berlin Heidelberg (1992).

[53]   A. Gulino, S. La Delfa, I. Fragalà, R.G. Egdell, Low-Temperature Stabilization of Tetragonal Zirconia by Bismuth, Chem. Mater. 8 (1996) 1287–1291. doi:10.1021/cm950558j.

[54]   G.F. Cerofolini, C. Galati, L. Renna, O. Viscuso, M. Camalleri, S. Lorenti, G.G. Condorelli, I.L. Fragalà, X-ray-photoemission-spectroscopy evidence for anomalous oxidation states of silicon after exposure of hydrogen-terminated single-crystalline (100) silicon to a diluted N2 : N2O atmosphere, J. Phys. D. Appl. Phys. 35 (2002) 1032–1038. doi:10.1088/0022-3727/35/10/311.

[55]   D. Briggs, M. Seah, H. Bubert, Practical Surface Analysis. Vol. 1: Auger and X-ray Photoelectron Spectroscopy, John Wiley & Sons, NY (1996).

[56]   H.F. Brinson, L.C. Brinson, Polymer Engineering Science and Viscoelasticity, Springer US, Boston, MA, 2015. doi:10.1007/978-1-4899-7485-3.

[57]   R. Houwink, H.K. de Decker, Elasticity, Plasticity and Structure of Matter, Cambridge University Press, Cambridge (2009).

[58]   G. Heinrich, M. Klüppel, T.A. Vilgis, Reinforcement of elastomers, Curr. Opin. Solid State Mater. Sci. 6 (2002) 195–203.

[59]   G. Heinrich, M. Kluppel, T.A. Vilgis, Reinforcement of elastomers, Curr. Opin. Solid State Mater. Sci. 6 (2002) 195–203.

[60]   E.M. Dannenberg, The Effects of Surface Chemical Interactions on the Properties of Filler-Reinforced Rubbers, Rubber Chem. Technol. 48 (1975) 410–444. doi:10.5254/1.3547460.

[61]   J.E. Mark, B. Erman, M. Roland, The science and technology of rubber, 4th ed., Academic Press, MA (2013).

[62]   C.G. Robertson, C.J. Lin, M. Rackaitis, C.M. Roland, Influence of Particle Size and Polymer–Filler Coupling on Viscoelastic Glass Transition of Particle-

Reinforced Polymers, Macromolecules. 41 (7)(2008) 2727-2731. doi: 10.1021/ma7022364.

[63] G. Huber, T.A. Vilgis, On the mechanism of hydrodynamic reinforcement in elastic composites, Macromolecules. 35 (2002) 9204–9210. doi:10.1021/ma0208887.

[64] M. Klüppel, The Role of Disorder in Filler Reinforcement of Elastomers on Various Length Scales, Springer Berlin Heidelberg (2003) 1–86. doi:10.1007/b11054.

[65] A.R. Payne, The dynamic properties of carbon black loaded natural rubber vulcanizates. Part II, J. Appl. Polym. Sci. 6 (1962) 368–372. doi:10.1002/app.1962.070062115.

[66] L. Mullins, Softening of Rubber by Deformation, Rubber Chem. Technol. 42 (1969) 339–362. doi:10.5254/1.3539210.

[67] L. Chazeau, J.D. Brown, L.C. Yanyo, S.S. Sternstein, Modulus recovery kinetics end other insights into the Payne effect for filled elastomers, Polym. Compos. 21 (2000) 202–222. doi:10.1002/pc.10178.

[68] G. Heinrich, M. Klüppel, T.A. Vilgis, Reinforcement of elastomers, Curr. Opin. Solid State Mater. Sci. 6 (2002) 195–203. doi:10.1016/S1359-0286(02)00030-X.

[69] H.W. Siesler, Rheo-optical Fourier-Transform infrared spectroscopy: Vibrational spectra and mechanical properties of polymers, Advances in Polymer Science, Springer Berlin Heidelberg (1984). 1–77. doi:10.1007/BFb0017101.

[70] L. Bokobza, Filled elastomers : a new approach based on measurements of chain orientation, Polymer (Guildf). 42 (2001) 5415–5423.

[71] C. Yuan, J. Wang, G. Chen, J. Zhang, J. Yang, Orientation studies of uniaxial drawn syndiotactic polystyrene/carbon nanotube nanocomposite films, Soft Matter. 7 (2011) 4039. doi:10.1039/c0sm01475c.

[72] C. Yuan, J. Zhang, G. Chen, J. Yang, Insight into carbon nanotube effect on polymer molecular orientation: an infrared dichroism study., Chem. Commun. (Camb). 47 (2011) 899–901. doi:10.1039/c0cc03198d.

[73] G. Chen, S. Liu, S. Zhang, Z. Qi, Self-assembly in a

polystyrene/montmorillonite nanocomposite, Macromol. Rapid Commun. 21 (2000) 746–749.

[74]   G. Chen, D. Shen, M. Feng, M. Yang, An Attenuated Total Reflection FT-IR Spectroscopic Study of Polyamide 6/Clay Nanocomposite Fibers, Macromol. Rapid Commun. 25 (2004) 1121–1124. doi:10.1002/marc.200400079.

[75]   G. Chen, Y. Ma, X. Zheng, G. Xu, J. Liu, J. Fan, D. Shen, Z. Qi, Wide angle X-ray diffraction and Fourier transform infrared dichroism studies of stretched-recovery-restretched process of polyurethane/clay nanocomposite, J. Polym. Sci. Part B Polym. Phys. 45 (2007) 654–660. doi:10.1002/polb.21075.

[76]   X. Dai, J. Xu, X. Guo, Y. Lu, D. Shen, N. Zhao, X. Luo, X. Zhang, Study on Structure and Orientation Action of Polyurethane Nanocomposites, Macromolecules. 37 (2004) 5615–5623. doi:10.1021/ma049900g.

[77]   T.A. Huy, R. Adhikari, G.H. Michler, Deformation behavior of styrene-block-butadiene-block-styrene triblock copolymers having different morphologies, Polymer (Guildf). 44 (2003) 1247–1257. doi:10.1016/S0032-3861(02)00548-7.

[78]   S. Onogi, T. Asada, A. Tanaka, Rheo-optical studies of high polymers. XIV. Study of the deformation mechanism in polymer blends of polypropylene with ethylene–propylene rubber, J. Polym. Sci. Part A-2 Polym. Phys. 7 (1969) 171–182. doi:10.1002/pol.1969.160070114.

[79]   H.W. Siesler, The characterization of polymer deformation by rheo-optical fourier-transform infrared spectroscopy, Makromol. Chemie. Macromol. Symp. 53 (1992) 89–103. doi:10.1002/masy.19920530111.

[80]   W.D. Callister, Materials Science And Engineering: An Introduction, John Wiley & Sons, DG Rethwisch (2007).

[81]   P.B. Bowden, R.J. Young, M. Science, Deformation mechanisms in crystalline polymers, J. Mater. Sci. 9 (1974) 2034–2051. doi:10.1007/BF00540553.

[82]   J.C. Halpin, J.L. Kardos, Moduli of crystalline polymers employing composite theory, J. Appl. Phys. 43 (1972) 2235–2241. doi:10.1063/1.1661482.

[83]   H.W. Siesler, K. Holland-Moritz, Infrared and Raman spectroscopy of

polymers, Marcel Dekker, NY and Basel (1980).

[84]   G. Chen, Z. Qi, D. Shen, Shear-induced ordered structure in polystyrene/clay nanocomposite, J. Mater. Res. 15 (2000) 351–356. doi:10.1557/JMR.2000.0055.

[85]   C.B. Wang, S.L. Cooper, Morphology and properties of segmented polyether polyurethaneureas, Macromolecules. 16 (1983) 775–786. doi:10.1021/ma00239a014.

[86]   R.N. Haward, G. Thackray, The Use of a Mathematical Model to Describe Isothermal Stress-Strain Curves in Glassy Thermoplastics, Proc. R. Soc. A Math. Phys. Eng. Sci. 302 (1968) 453–472. doi:10.1098/rspa.1968.0029.

[87]   R.N. Haward, Strain Hardening of Thermoplastics, Macromolecules. 26 (1993) 5860–5869. doi:10.1021/ma00074a006.

[88]   G. Michler, Electron microscopy of polymers, Springer-Verlag Berlin Heidelberg (2008).

[89]   S. Hüfner, Photoelectron spectroscopy : principles and applications, Springer-Verlag Berlin Heidelberg, NY (2003).

[90]   T. Hemraj-Benny, S. Banerjee, S. Sambasivan, M. Balasubramanian, D.A. Fischer, G. Eres, A.A. Puretzky, D.B. Geohegan, D.H. Lowndes, W. Han, J.A. Misewich, S.S. Wong, Near-edge X-ray absorption fine structure spectroscopy as a tool for investigating nanomaterials, Small. 2 (2006) 26–35. doi:10.1002/smll.200500256.

[91]   A.G. Lambert, P.B. Davies, D.J. Neivandt, Implementing the Theory of Sum Frequency Generation Vibrational Spectroscopy: A Tutorial Review, Appl. Spectrosc. Rev. 40 (2005) 103–145. doi:10.1081/ASR-200038326.

[92]   B.E.A. Saleh, M.C. Teich, Fundamentals of photonics, Wiley-Interscience, (2007).

[93]   R.D.B. Fraser, Interpretation of Infrared Dichroism in Fibrous Proteins —the 2µ Region, J. Chem. Phys. 24 (1956) 89. doi:10.1063/1.1700877.

[94]   P.H. Hermans, Contribution To The Physics Of Cellulose Fibres, Elseview Publishing Company, London (1946).

[95]   R.S. Stein, The X-ray diffraction, birefringence, and infrared dichroism of stretched polyethylene. II. Generalized uniaxial crystal orientation, J. Polym.

Sci. 31 (1958) 327–334. doi:10.1002/pol.1958.1203112309.

[96]   R.J. Samuels, Structured polymer properties: the identification, interpretation, and application of crystalline polymer structure, Wiley, NY (1974).

[97]   S. Glantz, Primer of Biostatistics, Seventh Edition, 7th ed., McGraw-Hill Education / Medical, New York, 2012.

[98]   M.L. McHugh, Multiple comparison analysis testing in ANOVA, Biochem. Medica. (2011) 203–209. doi:10.11613/BM.2011.029.

[99]   V. Bacarea, Odabrane teme iz biostatistike Lessons in biostatistics, 20 (2010) 15–32.

[100]   H. Abdi, L. Williams, Newman-Keuls test and Tukey test, Encycl. Res. Des. (2010).

[101]   J.C.H. Affdl, J.L. Kardos, The Halpin-Tsai equations: A review, Polym. Eng. Sci. 16 (1976) 344–352. doi:10.1002/pen.760160512.

[102]   Y. Benveniste, A new approach to the application of Mori-Tanaka's theory in composite materials, Mech. Mater. 6 (1987) 147–157. doi:10.1016/0167-6636(87)90005-6.

[103]   R.M. Christensen, K.H. Lo, Solutions for effective shear properties in three phase sphere and cylinder models, J. Mech. Phys. Solids. 27 (1979) 315–330. doi:10.1016/0022-5096(79)90032-2.

[104]   R.M. Christensen, A Critical Evaluation for a Class of Micro-Mechanics Models, in: Inelast. Deform. Compos. Mater., Springer New York, New York, NY, 1991: pp. 275–282. doi:10.1007/978-1-4613-9109-8_13.

[105]   S. Agnelli, G. Ramorino, S. Passera, J. Karger-Kocsis, T. Ricco, Fracture resistance of rubbers with MWCNT, organoclay, silica and carbon black fillers as assessed by the J-integral: Effects of rubber type and filler concentration, Express Polym. Lett. (2012). doi:10.3144/expresspolymlett.2012.61.

[106]   J. Jancar, L. Recman, Particle size dependence of the elastic modulus of particulate filled PMMA near its Tg, 2010. doi:10.1016/j.polymer.2010.06.041.

[107]   Z.X. Ooi, H. Ismail, A.A. Bakar, Optimisation of oil palm ash as

reinforcement in natural rubber vulcanisation: A comparison between silica and carbon black fillers, Polym. Test. 32 (2013) 625–630. doi:10.1016/j.polymertesting.2013.02.007.

[108]   R.W. Style, R. Boltyanskiy, B. Allen, K.E. Jensen, H.P. Foote, J.S. Wettlaufer, E.R. Dufresne, Stiffening solids with liquid inclusions, Nat. Phys. 11 (2014) 82–87. doi:10.1038/nphys3181.

[109]   H. Montes, and F. Lequeux, J. Berriot, Influence of the Glass Transition Temperature Gradient on the Nonlinear Viscoelastic Behavior in Reinforced Elastomers, Macromolecules, 36 (21), (2003) 8107-8118.

[110]   M.R.B. Mermet-Guyennet, J. Gianfelice de Castro, M. Habibi, N. Martzel, M.M. Denn, D. Bonn, LAOS: The strain softening/strain hardening paradox, J. Rheol. (N. Y. N. Y). 59 (2015) 21–32. doi:10.1122/1.4902000.

[111]   S.H. Bumm, J.L. White, A.I. Isayev, Breakup of silica agglomerates in corotating twin-screw extruder: Modeling and experiment, J. Elastomers Plast. 46 (2014) 527–552. doi:10.1177/0095244313476508.

[112]   T. Inoue, K. Osaki, Rheological properties of poly(vinyl alcohol)/sodium borate aqueous solutions, Rheol. Acta. 32 (1993) 550–555. doi:10.1007/BF00369071.

[113]   D. Quemada, D. Quemada, Rheological modelling of complex fluids. I. The concept of effective volume fraction revisited, Eur. Phys. J. Appl. Phys. 1 (1998) 119–127. doi:10.1051/epjap:1998125.

[114]   M. Bailly, M. Kontopoulou, K. El Mabrouk, Effect of polymer/filler interactions on the structure and rheological properties of ethylene-octene copolymer/nanosilica composites, Polymer (Guildf). 51 (2010) 5506–5515. doi:10.1016/j.polymer.2010.09.051.

[115]   J. Forsman, J.P. Harrison, A. Rutenberg, Elasticity of a percolation system: silica smoke, Canadian Journal of Physics. 65 (7), (1987) 767-771.

[116]   T.A. Witten, M. Rubinstein, R.H. Colby, Reinforcement of rubber by fractal aggregates, J. Phys. II France. 3, (1993) 367–383.

[117]   Q. Chen, S. Gong, J. Moll, D. Zhao, S.K. Kumar, R.H. Colby, Mechanical Reinforcement of Polymer Nanocomposites from Percolation of a Nanoparticle Network, ACS Macro Lett. 4(4) (2015) 398-402.

Bibliography

[118]   E. Guth, Theory of Filler Reinforcement, J. Appl. Phys. 16 (1945) 20.
        doi:10.1063/1.1707495.

[119]   J.-P. Hansen, I.R. McDonald, Theory of simple liquids, Academic Press,
        London (2006).

[120]   J.K.G. Dhont, An introduction to dynamics of colloids, Elsevier, Amsterdam
        (1996).

[121]   S. Torquato, Random Heterogeneous Materials, Springer New York, NY
        (2002). doi:10.1007/978-1-4757-6355-3.

[122]   G. Raos, Application of the Christensen-Lo Model to the Reinforcement of
        Elastomers by Fractal Fillers, Macromol. Theory Simulations. 12 (2003) 17–
        23. doi:10.1002/mats.200390002.

[123]   M.R.B. Mermet-Guyennet, J. Gianfelice de Castro, H.S. Varol, M. Habibi, B.
        Hosseinkhani, N. Martzel, R. Sprik, M.M. Denn, A. Zaccone, S.H. Parekh, D.
        Bonn, Size-dependent reinforcement of composite rubbers, Polymer
        (Guildf). 73 (2015) 170–173. doi:10.1016/j.polymer.2015.07.041.

[124]   D.W. McCarthy, J.E. Mark, S.J. Clarson, D.W. Schaefer, Synthesis, structure,
        and properties of hybrid organic-inorganic composites based on
        polysiloxanes. II. Comparisons between poly(methylphenylsiloxane) and
        poly(dimethylsiloxane), and between titania and silica, J. Polym. Sci. Part B
        Polym. Phys. 36 (1998) 1191–1200.

[125]   L. Dewimille, B. Bresson, L. Bokobza, Synthesis, structure and morphology
        of poly(dimethylsiloxane) networks filled with in situ generated silica
        particles,   Polymer   (Guildf).   46   (2005)   4135–4143.
        doi:10.1016/j.polymer.2005.02.049.

[126]   A.R. Payne, Effect of dispersion on the dynamic properties of filler-loaded
        rubbers,   J.   Appl.   Polym.   Sci.   9   (1965)   2273–2284.
        doi:10.1002/app.1965.070090619.

[127]   C. Chevigny, N. Jouault, F. Dalmas, F. Boué, J. Jestin, Tuning the mechanical
        properties in model nanocomposites: Influence of the polymer-filler
        interfacial interactions, J. Polym. Sci. Part B Polym. Phys. 49 (2011) 781–
        791. doi:10.1002/polb.22246.

[128]   P. Akcora, H. Liu, S.K. Kumar, J. Moll, Y. Li, B.C. Benicewicz, L.S. Schadler, D.

Acehan, A.Z. Panagiotopoulos, V. Pryamitsyn, V. Ganesan, J. Ilavsky, P. Thiyagarajan, R.H. Colby, J.F. Douglas, Anisotropic self-assembly of spherical polymer-grafted nanoparticles., Nat. Mater. 8 (2009) 354–9. doi:10.1038/nmat2404.

[129] S.K. Kumar, N. Jouault, B. Benicewicz, T. Neely, Nanocomposites with Polymer Grafted Nanoparticles, Macromolecules. 46 (2013) 3199–3214.

[130] R. Hasegawa, Y. Aoki, M. Doi, Optimum Graft Density for Dispersing Particles in Polymer Melts, Macromolecules. 29 (1996) 6656–6662. doi:10.1021/ma960365x.

[131] Q. Zhang, L.A. Archer, Poly(ethylene oxide)/Silica Nanocomposites: Structure and Rheology, Langmuir. 18 (2002) 10435–10442. doi:10.1021/la026338j.

[132] M.I. Aranguren, E. Mora, C.W. Macosko, Compounding Fumed Silicas into Polydimethylsiloxane: Bound Rubber and Final Aggregate Size, J. Colloid Interface Sci. 195 (1997) 329–337. doi:10.1006/jcis.1997.5143.

[133] M. Sovago, E. Vartiainen, M. Bonn, Determining Absolute Molecular Orientation at Interfaces: A Phase Retrieval Approach for Sum Frequency Generation Spectroscopy, J. Phys. Chem. C. 113 (2009) 6100–6106. doi:10.1021/jp810123g.

[134] R. Kotsilkova, D. Fragiadakis, P. Pissis, Reinforcement effect of carbon nanofillers in an epoxy resin system: Rheology, molecular dynamics, and mechanical studies, J. Polym. Sci. Part B Polym. Phys. 43 (2005) 522–533. doi:10.1002/polb.20352.

[135] G.P. Baeza, A.C. Genix, C. Degrandcourt, J. Gummel, A. Mujtaba, K. Saalwächter, T. Thurn-Albrecht, M. Couty, J. Oberdisse, Studying Twin Samples Provides Evidence for a Unique Structure- Determining Parameter in Simplifed Industrial Nanocomposites, ACS Macro Lett. 3 (2014) 448–452.

[136] C. Yam, Z. Xiao, J. Gu, S. Boutet, C. Cai, Modification of Silicon AFM Cantilever Tips with an Oligo (ethylene glycol) Derivative for Resisting Proteins and Maintaining a Small Tip Size for High-Resolution Imaging, J. Am. Chem. Soc. 125 (2003) 7498–7499.

[137] I. Leontis, A. Othonos, A.G. Nassiopoulou, Structure , morphology , and photoluminescence of porous Si nanowires : effect of different chemical

treatments, Nanoscale Res. Lett. 8 (2013) 1–7.

[138]   Y. Nagata, S. Mukamel, Vibrational sum-frequency generation spectroscopy at the water/lipid interface: Molecular dynamics simulation study, J. Am. Chem. Soc. 132 (2010) 6434–6442. doi:10.1021/ja100508n.

[139]   J. Wang, M.A. Even, Z. Chen, Sum Frequency Generation Vibrational Spectroscopy Studies on "Buried" Polymer/Polymer Interfaces, Macromolecules. 35 (2002) 8093–8097. doi:10.1021/ma0205717.

[140]   C.L. Loch, J. Wang, Z. Chen, Different Molecular Structures at Polymer/Silane Interfaces Detected by SFG, J. Phys. Chem. B. 107 (2003) 10440–10445. doi:10.1021/jp035211f.

[141]   C.L. Loch, D. Ahn, C. Chen, J. Wang, Z. Chen, Sum Frequency Generation Studies at Poly (ethylene terephthalate)/ Silane Interfaces : Hydrogen Bond Formation and Molecular Conformation Determination, Langmuir. (2004) 5467–5473.

[142]   J. Wang, C. Chen, S.M. Buck, Z. Chen, Sum Frequency Generation (SFG) Vibrational Spectroscopy, J. Phys. Chem. B. 105 (2001) 12118–12125.

[143]   J. Wang, Z. Paszti, M.A. Even, Z. Chen, Measuring Polymer Surface Ordering Differences in Air and Water by Sum Frequency Generation Vibrational Spectroscopy, J. Am. Chem. Soc. 124 (2002) 7016–7023.

[144]   Z. Chen, Y.R. Shen, G. a Somorjai, Studies of polymer surfaces by sum frequency generation vibrational spectroscopy., Annu. Rev. Phys. Chem. 53 (2002) 437–65. doi:10.1146/annurev.physchem.53.091801.115126.

[145]   C. Zhang, Z. Chen, Probing Molecular Structures of Poly (dimethylsiloxane) at Buried Interfaces in Situ, J. Phys. Chem. C. 117 (2013) 3903–3914.

[146]   J.E. Baio, C. Jaye, D.A. Fischer, T. Weidner, Multiplexed orientation and structure analysis by imaging near-edge X-ray absorption fine structure (MOSAIX) for combinatorial surface science., Anal. Chem. 85 (2013) 4307–10. doi:10.1021/ac4003479.

[147]   H.-J. Himmel, A. Terfort, C. Wöll, Fabrication of a Carboxyl-Terminated Organic Surface with Self-Assembly of Functionalized Terphenylthiols: The Importance of Hydrogen Bond Formation, J. Am. Chem. Soc. 120 (1998) 12069–12074. doi:10.1021/ja981872s.

Bibliography

[148]   D.A. Outka, J. Stöhr, J.P. Rabe, J.D. Swalen, The orientation of Langmuir–Blodgett monolayers using NEXAFS, J. Chem. Phys. 88 (1988) 4076. doi:10.1063/1.453862.

[149]   P. Väterlein, R. Fink, E. Umbach, W. Wurth, Analysis of the x-ray absorption spectra of linear saturated hydrocarbons using the Xα scattered-wave method, J. Chem. Phys. 108 (1998) 3313. doi:10.1063/1.475729.

[150]   K. Weiss, P.S. Bagus, C. Wöll, Rydberg transitions in X-ray absorption spectroscopy of alkanes: The importance of matrix effects, J. Chem. Phys. 111 (1999) 6834. doi:10.1063/1.479976.

[151]   A. Afzal, H.M. Siddiqi, S. Saeed, Z. Ahmad, Exploring resin viscosity effects in solventless processing of nano-SiO_2/epoxy polymer hybrids, RSC Adv. 3 (2013) 3885. doi:10.1039/c3ra21150a.

[152]   A. Gulino, F. Lupo, M.E. Fragalà, S.L. Schiavo, X-ray photoelectron spectroscopy: A powerful tool for electronic and structural investigations of covalently assembled monolayers. a representative case study, J. Phys. Chem. C. 113 (2009) 13558–13564. doi:10.1021/jp9027436.

[153]   S.R. Puniredd, O. Assad, H. Haick, Highly Stable Organic Monolayers for Reacting Silicon with Further Functionalities : The Effect of the C # C Bond nearest the Silicon Surface Highly Stable Organic Monolayers for Reacting Silicon with Further Functionalities : The Effect of the C-C Bond n, (2008) 13727–13734. doi:10.1021/ja804674z.

[154]   Z.C. Liu, Q.G. He, P.F. Xiao, B. Liang, J.X. Tan, N.Y. He, Z.H. Lu, Self-assembly monolayer of mercaptopropyltrimethoxysilane for electroless deposition of Ag, Mater. Chem. Phys. 82 (2003) 301–305. doi:10.1016/S0254-0584(03)00135-4.

[155]   Y.X. Shao, D. Dong, Y.H. Cai, S. Wang, S.G. Ang, G.Q. Xu, Thermal and Photoinduced Covalent Attachment of 3-Chloro-1-propanol on Si (100)-2x1, J. Phys. Chem. C. 114 (2010) 17159–17165.

[156]   H. Roghani-Mamaqani, V. Haddadi-Asl, Edge-functionalized graphene nanoplatelets with polystyrene by atom transfer radical polymerization : grafting through carboxyl, Polym. Int. 63 (2014) 1912–1923. doi:10.1002/pi.4730.

[157]   R. Sengupta, S. Chakraborty, S. Bandyopadhyay, S. Dasgupta, R.

Mukhopadhyay, K. Auddy, a S. Deuri, A Short Review on Rubber / Clay Nanocomposites With Emphasis on Mechanical Properties, Polym. Eng. Sci. 47 (2007) 21–25. doi:10.1002/pen.

[158] G. Mani, D.M. Johnson, D. Marton, V.L. Dougherty, M.D. Feldman, D. Patel, A. a. Ayon, C. Mauli Agrawal, Stability of self-assembled monolayers on titanium and gold, Langmuir. 24 (2008) 6774–6784. doi:10.1021/la8003646.

[159] J.L. Armstrong, Thermal chemistry of biacetyl on Si(100), J. Vac. Sci. Technol. A Vacuum, Surfaces, Film. 16 (1998) 123. doi:10.1116/1.580958.

[160] S.H. Li, X.F. Zhu, Y.P. Zhao, Carbon-assisted growth of SiO x nanowires, J. Phys. Chem. B. 108 (2004) 17032–17041. doi:10.1021/jp048418x.

[161] M. Schildenberger, R. Prins, Y.C. Bonetti, Foils, Films, and Nanostructured Surfaces: A Comparative XPS and AFM Study of Model Catalyst Surfaces, J. Phys. Chem. B. 104 (2000) 3250–3260. doi:10.1021/jp9932970.

[162] A. Azioune, N. Carpi, J. Fink, M.M. Chehimi, D. Cuvelier, M. Piel, Robust method for high-throughput surface patterning of deformable substrates, Langmuir. 27 (2011) 7349–7352. doi:10.1021/la200970t.

[163] X. Vanden Eynde, J.P. Servais, M. Lamberigts, Investigation into the surface selective oxidation of dual-phase steels by XPS, SAM and SIMS, Surf. Interface Anal. 35 (2003) 1004–1014. doi:10.1002/sia.1639.

[164] A.G. Kannan, N.R. Choudhury, N.K. Dutta, Synthesis and characterization of methacrylate phospho-silicate hybrid for thin film applications, Polymer (Guildf). 48 (2007) 7078–7086. doi:10.1016/j.polymer.2007.09.050.

[165] T. Glomann, G.J. Schneider, J. Allgaier, a. Radulescu, W. Lohstroh, B. Farago, D. Richter, Microscopic dynamics of polyethylene glycol chains interacting with silica nanoparticles, Phys. Rev. Lett. 110 (2013) 1–5. doi:10.1103/PhysRevLett.110.178001.

[166] T. Glomann, A. Hamm, J. Allgaier, E.G. Hübner, A. Radulescu, B. Farago, G.J. Schneider, A microscopic view on the large scale chain dynamics in nanocomposites with attractive interactions, Soft Matter. 9 (2013) 10559. doi:10.1039/c3sm51194d.

[167] S.Y. Kim, H.W. Meyer, K. Saalwa, C.F. Zukoski, Polymer Dynamics in PEG-Silica Nanocomposites : E ff ects of Polymer Molecular Weight ,

Temperature and Solvent Dilution, Macromolecules. 45 (2012) 4225–4237.

[168]   T. Weidner, A. Krämer, C. Bruhn, M. Zharnikov, A. Shaporenko, U. Siemeling, F. Träger, Novel tripod ligands for prickly self-assembled monolayers., Dalton Trans. (2006) 2767–77. doi:10.1039/b515727g.

[169]   U. Glebe, T. Weidner, J.E. Baio, D. Schach, C. Bruhn, A. Buchholz, W. Plass, S. Walleck, T. Glaser, U. Siemeling, Self-Assembled Monolayers of Single-Molecule Magnets [Tb{Pc'(SR) 8 } 2] on Gold, Chempluschem. 77 (2012) 889–897. doi:10.1002/cplu.201200043.

[170]   B.J. Carey, P.K. Patra, L. Ci, G.G. Silva, P.M. Ajayan, Observation of dynamic strain hardening in polymer nanocomposites, ACS Nano. 5 (2011) 2715–2722. doi:10.1021/nn103104g.

[171]   Y. Huang, D.R. Paul, Effect of MolecularWeight and Temperature on Physical Aging of ThinGlassy Poly(2,6-dimethyl-1,4-phenylene oxide) Films, J. Polym. Sci. Part B Polym. Phys. 45 (2007) 1390–1398. doi:10.1002/polb.

[172]   B. Na, R. Lv, W. Xu, P. Yu, K. Wang, Q. Fu, Inverse temperature dependence of strain hardening in ultrahigh molecular weight polyethylene: Role of lamellar coupling and entanglement density, J. Phys. Chem. B. 111 (2007) 13206–13210. doi:10.1021/jp075990q.

[173]   J. Jancar, R.S. Hoy, A.J. Lesser, E. Jancarova, J. Zidek, Effect of Particle Size, Temperature, and DeformationRate on the Plastic Flow and Strain Hardening Response of PMMA Composites., Macromolecules. 46 (2013) 9409–9426. doi:10.1021/ma400965c.

[174]   B. PUKANSZKY, Influence of interface interaction on the ultimate tensile properties of polymer composites, Composites. 21 (1990) 255–262. doi:10.1016/0010-4361(90)90240-W.

[175]   P. Costa, J. Silva, V. Sencadas, R. Simoes, J.C. Viana, S. Lanceros-Méndez, Mechanical, electrical and electro-mechanical properties of thermoplastic elastomer styrene–butadiene–styrene/multiwall carbon nanotubes composites, J. Mater. Sci. (2012) 1172–1179. doi:10.1007/s10853-012-6855-7.

[176]   R.A. Riggleman, G. Toepperwein, G.J. Papakonstantopoulos, J.-L. Barrat, J.J. de Pablo, Entanglement network in nanoparticle reinforced polymers., J. Chem. Phys. 130 (2009) 244903. doi:10.1063/1.3148026.

Bibliography

[177] F. Jiang, Y. Zhang, Z. Wang, W. Wang, Z. Xu, Z. Wang, Combination of magnetic and enhanced mechanical properties for copolymer-grafted magnetite composite thermoplastic elastomers, ACS Appl. Mater. Interfaces. 7 (2015) 10563–10575. doi:10.1021/acsami.5b02208.

[178] F. Jiang, Y. Zhang, C. Fang, Z. Wang, Z. Wang, From soft to strong elastomers: the role of additional crosslinkings in copolymer-grafted multiwalled carbon nanotube composite thermoplastic elastomers, RSC Adv. 4 (2014) 60079–60085. doi:10.1039/C4RA11626G.

[179] A. Pei, J.M. Malho, J. Ruokolainen, Q. Zhou, L.A. Berglund, Strong nanocomposite reinforcement effects in polyurethane elastomer with low volume fraction of cellulose nanocrystals, Macromolecules. 44 (2011) 4422–4427. doi:10.1021/ma200318k.

[180] Y.H. Ha, E.L. Thomas, Deformation behavior of a roll-cast layered-silicate/lamellar triblock copolymer nanocomposite, Macromolecules. 35 (2002) 4419–4428. doi:10.1021/ma012210h.

[181] L. Bokobza, G. Garnaud, J.E. Mark, J.M. Jethmalani, E.E. Seabolt, W.T. Ford, Effects of Filler Particle/Elastomer Distribution and Interaction on Composite Mechanical Properties, Chem. Mater. 14 (2002) 162–167. doi:10.1021/cm010462r.

[182] Z. Wang, J. Liu, S. Wu, W. Wang, L. Zhang, Novel percolation phenomena and mechanism of strengthening elastomers by nanofillers., Phys. Chem. Chem. Phys. 12 (2010) 3014–3030. doi:10.1039/b919789c.

[183] L. Bistričić, M. Leskovac, G. Baranović, S.L. Blagojević, Mechanical properties and linear infrared dichroism of thin films of polyurethane nanocomposites, J. Appl. Polym. Sci. 108 (2008) 791–803. doi:10.1002/app.27754.

[184] M. Rubinstein, R.H. Colby, Polymer physics (Chemistry), Oxford University Press, Oxford (2003).

[185] H.S. Varol, M.A. Sánchez, H. Lu, J.E. Baio, C. Malm, N. Encinas, M.R.B. Mermet-Guyennet, N. Martzel, D. Bonn, M. Bonn, T. Weidner, E.H.G. Backus, S.H. Parekh, Multiscale Effects of Interfacial Polymer Confinement in Silica Nanocomposites, Macromolecules. 48 (2015) 7929–7937. doi:10.1021/acs.macromol.5b01111.

Bibliography

[186] M. Mooney, A theory of large elastic deformation, J. Appl. Phys. 11 (1940) 582–592. doi:10.1063/1.1712836.

[187] R.N. Haward, The physics of glassy polymers, 2nd ed., Springer Netherlands, Dordrecht (1997).

[188] C. Fang, Y. Zhang, W. Wang, Z. Wang, F. Jiang, Z. Wang, Fabrication of Copolymer-Grafted Multiwalled Carbon Nanotube Composite Thermoplastic Elastomers Filled with Unmodified MWCNTs as Additional Nanofillers to Significantly Improve Both Electrical Conductivity and Mechanical Properties, Ind. Eng. Chem. Res. 54 (2015) 12597–12606. doi:10.1021/acs.iecr.5b03599.

[189] I.M. Ward, J. Sweeney, Mechanical properties of solid polymers, 3rd ed., John Wiley & Sons, Chichester (2012).

[190] Y.-H. Lin, Polymer viscoelasticity : basics, molecular theories, experiments and simulations, 2nd ed., World Scientific, Singapore (2011).

[191] M. Richard-Lacroix, C. Pellerin, Accurate new method for molecular orientation quantification using polarized raman spectroscopy, Macromolecules. 46 (2013) 5561–5569. doi:10.1021/ma400955u.

[192] T. Keplinger, E. Cabane, M. Chanana, P. Hass, V. Merk, N. Gierlinger, I. Burgert, A versatile strategy for grafting polymers to wood cell walls., Acta Biomater. 11 (2015) 256–63. doi:10.1016/j.actbio.2014.09.016.

[193] S. Prasertsri, F. Lagarde, N. Rattanasom, C. Sirisinha, P. Daniel, Raman spectroscopy and thermal analysis of gum and silica-filled NR/SBR blends prepared from latex system, Polym. Test. 32 (2013) 852–861. doi:10.1016/j.polymertesting.2013.04.007.

[194] S. Prakanrat, P. Phinyocheep, P. Daniel, Spectroscopic Investigation of Polystyrene Surface Grafting on Natural Rubber, Appl. Spectrosc. 63 (2009) 233–238. doi:10.1366/000370209787391978.

[195] K. Bruckmoser, K. Resch, T. Kisslinger, T. Lucyshyn, Measurement of interdiffusion in polymeric materials by applying Raman spectroscopy, Polym. Test. 46 (2015) 122–133. doi:10.1016/j.polymertesting.2015.07.004.

[196] D.I. Bower, M.F. Maddams, The Vibrational Spectroscopy of Polymers, Cambridge University Press, Cambridge (1992).

Bibliography

[197] H.G. Kilian, M. Strauss, W. Hamm, Universal Properties in Filler-Loaded Rubbers, Rubber Chem. Technol. 67 (1994) 1–16. doi:10.5254/1.3538664.

[198] G.P. Baeza, C. Dessi, S. Costanzo, D. Zhao, S. Gong, A. Alegria, R.H. Colby, M. Rubinstein, D. Vlassopoulos, S.K. Kumar, Network dynamics in nanofilled polymers., Nat. Commun. 7 (2016) 11368. doi:10.1038/ncomms11368.

[199] H. Zhang, A.K. Scholz, F. Vion-Loisel, Y. Merckel, M. Brieu, H. Brown, S. Roux, E.J. Kramer, C. Creton, Opening and closing of nanocavities under cyclic loading in a soft nanocomposite probed by real-time small-angle X-ray scattering, Macromolecules. 46 (2013) 900–913. doi:10.1021/ma302325w.

[200] S.K. Peddini, C.P. Bosnyak, N.M. Henderson, C.J. Ellison, D.R. Paul, Nanocomposites from styrene-butadiene rubber (SBR) and multiwall carbon nanotubes (MWCNT) part 2: Mechanical properties, Polym. (United Kingdom). 56 (2015) 443–451. doi:10.1016/j.polymer.2014.11.006.

SUMMARY

Materials including hard nano fillers inside of a soft polymeric matrix are called polymer nanocomposites. Nanocomposites are all around us; we sometimes find them at the sea side in a shape of nacre, in our daily life routine as the basic material of tires of our car, and even in our body as teeth in our mouth or as blood clots in response to cuts on our skin. Thanks to the large surface-to-volume ratio of nanofillers, even very small amounts of fillers offer substantial improvements to the host polymer properties – of which toughness, optical properties, yield strength, stiffening, and electrical conductivity may be counted among. However, the physico-chemical origin of this wide range of characteristic changes due to filler dispersion is still not fully understood.

Since almost a century, the addition of nanofillers, which are mainly carbon black or silica particles, to rubbery polymers (elastomers) has been used primarily for improving the mechanics of commercial elastomers in the market and for research. These formulations normally introduce many other ingredients such as cross-linkers, catalyzers and so on, for improving filler dispersion and altering certain characteristics of the final materials, particularly their mechanical characteristics. Such complex chemical formulations and lack of knowledge about spectroscopic and microscopic properties of nanocomposites are two fundamental challenges for explaining the effect of nanofiller chemistry and morphology on the nanocomposite macroscale viscoelasticity.

The central idea of this thesis can be expressed as 'molecular scale explanation of the linear and non-linear elastic properties of industrial nanocomposites by inclusion of nano-size silica fillers'. In each Chapter of this thesis where I included my data, I tried to answer some sub-questions stemming from this main question. In order to address the sub-questions, I always tried to find the answer in a 'triangle of data' consisting of molecular spectroscopy (physical chemistry), electron microscopy (structure) and mechanical characterization (mechanics) of silica filled rubber systems.

In Chapter 3, I examined the linear elasticity – reinforcement – of filled elastomer systems. The positive effect of using nano-size fillers on the reinforcement of the elastomer based nanocomposites is already known. However, classical micromechanical models (e.g., the Einstein – Smallwood or Guth – Einstein models) cannot explain the scale-dependent reinforcement in such nanocomposites, particularly at high volume fraction filler loading. In the course of my work, for various chemistries and micro- and nanocomposite systems, we found

that the reinforcement increases with decreasing filler size. The master scaling proposed in this chapter relates the reinforcement of the composites to their particle size, volume fraction, and relative moduli of host polymer and hard filler. The experimental reinforcement values of various microcomposite model systems and industrial nanocomposites were successfully described by our scaling model.

In Chapter 4, we investigate the fundamental reason behind the phenomenon of simple functional (Si-OH) groups at the end of each rubber molecule modifying the dispersion of silica nano fillers. The ability to control the dispersion of fillers is one of the key factors for tuning their linear and nonlinear elastic properties. Among different synthetic strategies, recently, silica filler dispersion was improved in SiO_2 / styrene-butadiene rubber (SBR) systems by simply having Si-OH groups at the end of each SBR chain. Parallel to such recent studies, in this chapter, I focused on finding the main reason for the filler dispersion improvement in similar SiO_2 / SBR systems with functional groups compared to those without functionalized rubber. Therefore, the interaction of the functional groups on the filler surface with the polymer host was investigated with various surface-sensitive spectroscopies. The constrained polymer molecular orientation at the nano-filler surface was detected, which was mediated by covalent bonding between Si-OH groups from the silica surface and the functional end groups. As a consequence of this ordering, in our simplified composite formulations which consist of only rubber and fillers, we observed smaller aggregates in the composites with functional groups compared to those without functional SBR.

In Chapter 5 we discussed the relations between filler size, filler amount, and strain-hardening using a combination of uniaxial tensile loading and micro-spectroscopic measurements of chain alignment. Strain hardening is very important non-linear elastic behavior for industrial composite materials that bear large cyclic loads, such as those used for car tires or bearing sealants. While a clear connection exists between filler size and amount for reinforcement as also discussed in Chapter 3, substantially less is known about the nonlinear regime at high strain, where strain-hardening begins to dominate the elastic response of the material. In this chapter, our results show that the strain-hardening modulus and chain alignment depend only on the amount, and not the size, of nanofillers. With the help of a theoretical scaling argument, we find that strain hardening is controlled by a product of the number of "bridging" chains that bear load between different filler aggregates and bridging chain alignment, which also depends only on the volume fraction of fillers. This is in contrast to the plateau or linear modulus

Summary

(reinforcement), which depends on both amount and size of nanofillers. These results highlight a critical difference between the origin of linear and nonlinear elasticity, respectively, in composite materials.

As a final part of the thesis, in Chapter 6, I indicated my preliminary results showing the effect of cyclic loading on the strain-hardening behavior of an NBR nanocomposite. In practical uses of rubber-based nanocomposite materials, they are subject to mechanical loads in cycles, and their behavior under cyclic load is very crucial for their life-time. Hardening of the nanocomposites under different cycle of loadings is not a new observation, and it has been discussed previously in terms of void size changes, filler-matrix interaction and alignment of inorganic fillers to the direction of loading. In our systems, even with the absence of many of already proposed reasons (no significant alignment of fillers, no filler-matrix interaction), we still observed a clear strain-hardening modulus increase under increasing cycles of loadings. In the near future, this work will be completed by investigating the filler volume and size effect on their cyclic strain-hardening behavior and also measuring NBR chain alignment by using polarized Raman spectroscopy, similar to what we did in Chapter 5.

SAMENVATTING

Polymeer-nanocomposieten zijn materialen waarbij harde nanovulstoffen zich in een zachte polymeermatrix bevinden. Polymeer-nanocomposieten zijn overal om ons heen; we vinden ze aan de kust in de vorm van parelmoer, in ons dagelijks leven als het basismateriaal van onze autobanden en zelfs in of op ons lichaam als de tanden in onze mond of als een wondkorstje op onze huid. Dankzij de grote oppervlakte-volumeverhouding van de nanovulstoffen kunnen zeer kleine hoeveelheden al substantiële verbeteringen in de eigenschappen van het originele polymeer bewerkstelligen, waaronder o.a. taaiheid, rekgrens, verstijving, optische eigenschappen en elektrische geleidbaarheid. De fysisch-chemische achtergrond van dit grote aantal veranderingen in eigenschappen, veroorzaakt door de dispersie van nanovulstoffen, is tot op heden nog niet volledig verklaard.

Al ongeveer een eeuw worden nanovulstoffen zoals carbon black en silica deeltjes toegevoegd aan rubberpolymeren (elastomeren) om de mechanische eigenschappen van commerciële elastomeren te verbeteren en voor onderzoek. In deze samenstellingen worden ook veel andere componenten toegevoegd zoals crosslinkers, katalysatoren, etc. om de dispersie van de nanovulstoffen te verbeteren en om bepaalde eigenschappen van het eindmateriaal te veranderen, in het bijzonder de mechanische eigenschappen. Zulke complexe chemische samenstellingen en het gebrek aan kennis over spectroscopische en microscopische eigenschappen van nanocomposieten zijn twee fundamentele uitdagingen bij het verklaren van het effect van de chemie en morfologie van de nanovulstoffen op viscoelasticiteit.

De hoofdgedachte van dit proefschrift kan uitgedrukt worden als 'verklaring op moleculaire schaal van de lineaire en niet-lineaire elastische eigenschappen van industriële nanocomposieten door insluiting van silica nanovulstoffen'. In elk hoofdstuk van dit proefschrift waarin ik mijn resultaten presenteer probeer ik een antwoord te geven op afgeleide vragen die voortvloeien uit die hoofdgedachte. Om de afgeleide vragen te beantwoorden heb ik steeds geprobeerd om een "driehoek van data" te creëren gebaseerd op moleculaire spectroscopie (fysische chemie), elektronenmicroscopie (structuur) en mechanische kenschetsing (mechanica) van met silica gevulde rubbers.

In hoofdstuk 3 heb ik de lineaire elasticiteit (versterking) van gevulde elastomeersystemen onderzocht. Het positieve effect dat nanovulstoffen hebben op de versterking van elastomeer nanocomposieten is al langer bekend. De

klassieke micromechanische modellen (bijv. de Einstein-Smallwood of Guth-Einstein modellen) kunnen de schaal-afhankelijke versterking in zulke nanocomposieten echter niet verklaren, in het bijzonder bij een hoge volumefractie aan vulstof. We hebben voor diverse formuleringen en diverse micro- en nanocomposietsystemen gevonden dat de versterking toenam bij afnemende vulstofafmetingen. De in dit hoofdstuk voorgestelde master scaling relateert de versterking van de composieten aan hun deeltjesgrootte, volumefractie en relatieve moduli van gastheerpolymeer en harde vulstof. De proefondervindelijke waarden van de versterking van verschillende microcomposietmodelsystemen en industriële nanocomposieten werden met succes beschreven door ons schaalmodel.

In hoofdstuk 4 wordt de fundamentele oorzaak onderzocht achter hoe een simpele functionele Si-OH groep aan het eind van elk rubbermolecuul de dispersie van silica nanovulstoffen kan wijzigen. Het vermogen om de dispersie van vulstoffen te controleren is een van de sleutelfactoren om de lineaire en non-lineaire elasticiteit aan te passen. Eén van de recente synthetische strategieën om de dispersie van silica vulstoffen in SiO2 / styreen-butadieen rubber (SBR) systemen te verbeteren is het aanbrengen van Si-OH groepen aan het einde van elke SBR keten. Parallel aan dergelijke recente studies focus ik in dit hoofdstuk op het vinden van de voornaamste reden voor verbeteringen van de vulstofdispersie in vergelijkbare SiO2 /SBR systemen met functionele groepen in vergelijking met systemen zonder functionele groepen. Dit werd gedaan door de interactie tussen de functionele groepen en het oppervlak van de vulstof te onderzoeken met oppervlaktegevoelige spectroscopie. De moleculaire oriëntatie van het gedwongen polymeer op het oppervlak van de nanovulstof werd gedetecteerd, gemedieerd door de covalente binding tussen de Si-OH groepen van silica en de functionele eindgroepen. Aan de hand van deze ordening konden we in onze vereenvoudigde composietsamenstellingen, die bestaan uit enkel rubber en vulstoffen, kleinere aggregaten in de composieten met functionele groepen detecteren in vergelijking met composieten zonder functionele SBR.

In hoofdstuk 5 bespreken we de relatie tussen de afmetingen van de vulstof, de hoeveelheid vulstof en deformatieharding door gebruik te maken van een eenassige trekbelasting en micro-spectroscopische metingen van de oriëntatie van de polymeerketens. Deformatieharding is een zeer belangrijk, niet-lineair gedrag van industriële composietmaterialen die onder hoge wisselbelastingen staan in bijvoorbeeld autobanden en lager-afdichtingen. Hoewel er een duidelijke

relatie bestaat tussen de afmetingen van de vulstof en versterking, zoals besproken in hoofdstuk 3, is er nog weinig bekend over het non-lineaire gedrag onder hoge trekbelasting waar de deformatieharding het elastische gedrag begint te beïnvloeden. In dit hoofdstuk laten onze resultaten zien dat de deformatieharding modulus en keten oriëntatie alleen afhangen van de hoeveelheid nanovulstoffen en niet van de afmetingen ervan. Met behulp van een theoretisch schaalmodel hebben we aangetoond dat de deformatieharding afhangt van het product van het aantal "verbindende" ketens dat belast wordt tussen verschillende vulstofaggregaten en de oriëntatie van verbindende ketens, welke ook alleen afhangt van de volumefractie van de vulstoffen. Dit in tegenstelling tot het plateau of de lineaire modulus (versterking) die afhangt van het aantal én de afmetingen van de nanovulstoffen. Deze resultaten benadrukken een cruciaal verschil tussen de oorsprong van lineaire en niet-lineaire elasticiteit in composieten.

In hoofstuk 6, als laatste deel van dit proefschrift, bespreek ik mijn voorlopige resultaten die het effect laten zien van cyclische belastingen op de deformatieharding van een NBR nanocomposiet. In de praktijk worden rubber nanocomposieten veel blootgesteld aan cyclische belastingen die een grote invloed hebben op de levensduur. Het deformatieharden van nanocomposieten tijdens cyclische belastingen is geen onbekend fenomeen en werd tot nu toe verklaard door veranderingen in de grootte van poriën, interactie tussen de vulstof en de polymeermatrix en de oriëntatie van anorganische vulstoffen in relatie tot de belasting. In onze systemen hebben we zonder de voorgenoemde verklaringen voor de veranderingen (geen significante oriëntatie van de vulstoffen in relatie tot de belasting, geen interactie tussen vulstof en polymeermatrix) toch een duidelijke toename in deformatiehardingmodulus waargenomen tijdens cyclische belastingen. In de nabije toekomst wordt dit werk voltooid door onderzoek te doen naar het effect van het volume en de afmetingen van de vulstof op de cyclische deformatieharding en door onderzoek te doen naar de oriëntatie van de NBR ketens door middel van gepolariseerde Raman spectroscopie, zoals beschreven in hoofdstuk 5.

ACKNOWLEDGEMENTS

First of all, it would not have been possible to write this thesis without the help of many people – secret heroes – around me, to only some of whom it is possible to express my gratitude here. Thus, as the opening words of my acknowledgement, I would sincerely like to apologize to those who I cannot write my gratefulness here.

Above all, I would like to thank Mischa for giving me the opportunity to be a part of his lovely department and for always being supportive and patient with me. Honestly, I will always admire you and try to understand how you can manage to provide us such a nice working environment. After Mischa, I owe very special thanks to my project leader Sapun. I want to thank him for teaching me how to be a stronger man and a good scientist. I am very happy and proud of being your *first* PhD student. While working together, I believe we learned a lot from each other. Herein, I need to address my appreciations to the entire AK-Bonn group particularly to Ellen Backus, Alejandra Sánchez, Tobias Weidner, Hao Lu, Johannes Hunger, Marc-Jan Van Zadel, Florian Gericke, Walter Scholdei and of course the lovely Laurie Gangloff. Along with these names, I want to mention also the *non-AK-Bonn people*, Ingo Lieberwirth, Gunnar Glasser, Andreas Hanewald, Katrin Kirchhoff and Uwe Rietzler, who never refused to provide me friendly and extremely helpful technical and scientific support when needed. Without the help of above sorted names, no scientific achievements in this thesis would be possible.

I want to send my special appreciation to the members of the "rubber project" specifically to Marius, Janaina, Babak, Fanlong, Alessio and of course Daniel Bonn as the founder/leader of the project. Dear Daniel, "*Stop, stop! We're all confused now*" sentence of you which I heard almost in every talk of mine given in front of you, taught me how to stand strong under the rain of challenging critics about my scientific findings. Thanks for being honest!

By remembering all the members in its history, I must say: "CARS ROCKS!" As a member of CARS, I learned a lot while working in this group, for instance, merciless critiques from Frederik taught me how to better defend my ideas. Xiao Ling´s excellent imitation of mine truly helped me to reflect better upon myself. Great

efforts by Mischa Schwendy to explain the basics of biology along with "dance" lessons for Lucia and I, will always inspire me in the future. To my dear super thiol-tolerant friend Sabine: it was nice to work, collaborate and in particular, sing with you. Last but certainly not least, Will and his endless effort for teaching me Igor coding, Nils and our pleasurable unplugged heavy metal sessions with *Fistook*, Christian Malm and his fantastic contribution to my thesis, Miriam, Yujen, Gustav, Schrudi and others. I will seriously miss 'CARS the Great'.

A very special thanks must be addressed to my lovely '*Mediterranean-Indian flavored lunch, party, coffee, Saturday market, talking – BS – group*'. First of all, Vasilis and Natalia, holding and supporting each other in sad days, happy days, party days, Funzelfahrt days will always be remembered with a smile. Extra line for Vasilis, your picture while holding a rabbit and dealing with *Greek* bureaucracy will be the cover of my next book, I promise. Noemí, you will always be in my PhD memories as the walking *post-doc-carrot* spreading love and peace around. Amala, I believe the decibel level of our laughter after each of our BS talks/imitations cannot be beaten by anyone else. For instance 'Salt Bae' must stay here as one of remembrance. Mike, the glorious and fearless lord of the cakes and a great friend – your smartly designed '*X bring cake polls*' will guide me a lot in my professional career! Melike, she is probably one of the best listeners in the world and of course 'the other Turk' in the group. By a few words, I have no idea how to describe your giant heart, Catarina Nardi Tironi. Of course, this list can go further with the names of many lovely people around me during my PhD years like, David and Elena, Andrea (greatest double bass player, half of *Fistook*), Cesare ("*como se diceee Cesarin Urbinooo*"), Alice, Hassan, Grazia Gonella, Uliana, Philipp, Selen, Filiz, Maria Kokkinopoulou, Francesco, Erika, Matthias, Johannes Franz, Prerna, Dimitra, Simon A. Bretschneider, Malte, Peng, Ilias, Claudia, Leonie Driessen and all the players (fighters) of the best football team ever "*golden girls / 2016*".

Very special thank must go to Sergio Mauri. Uncle Gigino, are you aware what have you done to me? You have introduced me to the most important person in my life and then you married us! You 'patiently' educated me how to drink wine and

eat good food (sometimes a bit too much) and so on. Thanks! Another special gratitude must be addressed to the lovely Giacomo and Valeria. I feel very lucky for knowing you guys. Every glass of wine, cold beer in Istanbul afternoon and many more will be lifelong remembered by Lucia and I. We truly believe this friendship will last forever.

To my beautiful aunt, Armağan and my uncle-in-law Emin: I am still trying to understand how you can be so generous!? Both of you particularly helped me a lot in making this country my home. For every success and happiness that I have in my life, I cannot forget your big role.

To my lovely sister, Bilge who has a beautiful and a pure lovely heart! My father, Fikret, the man always standing strong and stiff like a mountain and for me he is the definition of "*Dad*". My mom, Sema, a huge piece of love combined with a strong patience and who is the backbone of my family. I want to send my deepest gratitude to three of you by the words of *Nazım Hikmet* who is probably a beautiful common thing between the four of us,

"yok öyle umutları yitirip karanlıkta savrulmak.

unutma; aynı gökyüzü altında, bir direniştir yaşamak."

Lucia! It is so hard to play with the words and letters to describe how I feel now. How can I frighten the characters and punish the words by trying to risk them to describe my love for you? They are not enough to portray my excitement and happiness about living a life beside you and "the beautiful new member of our life" in our warm *casettina* as a family. But, again my best friend, *Nazım* is next to me and helping me with his words for describing my love to you,

"Hoş geldin kadınım benim hoş geldin

ayağını basdın odama kırk yıllık beton, çayır çimen şimdi

güldün, güller açıldı penceremin demirlerinde

ağladın, avuçlarıma döküldü inciler

gönlüm gibi zengin hürriyet gibi aydınlık oldu odam…"